Combinatorial Thin Film Sputtering for Rapid Materials Discovery of Next Generation Alloys

A Dissertation Presented for the
Doctor of Philosophy
Degree
The University of Tennessee, Knoxville

Reece Chastain Emery
May 2024

DEDICATION

This work is dedicated to:

Elizabth Chastain Emery

J. Wayne and Linda Salyer

ACKNOWLEDGEMENTS

First of all, I would like to acknowledge my family and friends. To my parents (John and Alisa) and my sister (Hannah): thank you. I would not be where I am without you. I would also like to thank my graduate advisor Philip Rack for his invaluable guidance and support. I would also thank my committee members: Eric Lass, Steven Randolph, and Zac Sims. A special thank you is also needed for Michael Koehler without whom this work would not have been possible. Thank you for dealing with all of the difficult/weird samples I would bring through the XRD lab. Finally, thank you to all of my lab mates. Grad school would not have been the same without you all.

ABSTRACT

Current methodologies for the development of new alloy systems and exploration of their properties are the rate-limiting step to meet application requirements for new end-use cases such as the replacement of Al-Si alloys or materials for extreme environments. A methodology for the rapid design of next generation alloy systems is also not well established. Thus, this work utilizes a gated down selection approach to develop and implement an accelerated material discovery process to address new and critical needs. Here, combinatorial sputtering is leveraged as the initial gate for down selection. Co-sputtering has been shown to be an effective rapid materials discovery process as it achieves thin film compositions that cover a large composition range while allowing for the realization of metastable and equilibrium material configurations. Thus, it may be leveraged to rapidly survey a wide composition space to identify suitable candidates that meet programmatic requirements relating to properties such as coefficient of thermal expansion and mechanical properties. Experimental techniques such as scanning electron microscopy (SEM), energy dispersive x-ray spectroscopy (EDXS), x-ray diffraction (XRD), temperature dependent XRD (TDXRD), and nanoindentation will be leveraged to fully characterize the combinatorial libraries and identify compositions that demonstrate unique or interesting properties. Upscaling into traditional metallurgy can then be utilized to confirm and further characterize these compositions of interest.

TABLE OF CONTENTS

LIST OF FIGURES

INTRODUCTION

Motivation

The primary motivations for this research are: (1) demonstrate the efficacy of the combinatorial thin film approach for mechanical alloy design, (2) identify methods that can characterize properties of interest to mechanical alloy design that are accessible from thin film materials, (3) rapidly explore new phase spaces for alloys of interest, which collectively (4) advance the Critical Materials Institute's mission to accelerate innovative scientific and technological solutions to develop resilient and secure supply chains for rare-earth metals and other materials critical to the success of clean energy technologies [1] and advance the UT-MRSEC Center for Advanced Materials and Manufacturing mission.

Thin Films

A thin film is a geometric configuration of a material in which one dimension, the thickness, is significantly reduced, typically on the nanometer scale up to a few microns. The thickness component is defined as the dimension normal to the supporting substrate. There are a myriad of experimental techniques that can be used to generate thin films. Techniques for generating films are typically subdivided into two categories: chemical and physical. The main chemical techniques include chemical vapor deposition, plasma enhanced chemical vapor deposition, laser assisted chemical vapor deposition, sol-gel, spray pyrolysis, and spin coating. Physical techniques are typically sputtering via direct current, radio frequency, magnetron, or ion beam, and evaporation through thermal, laser,

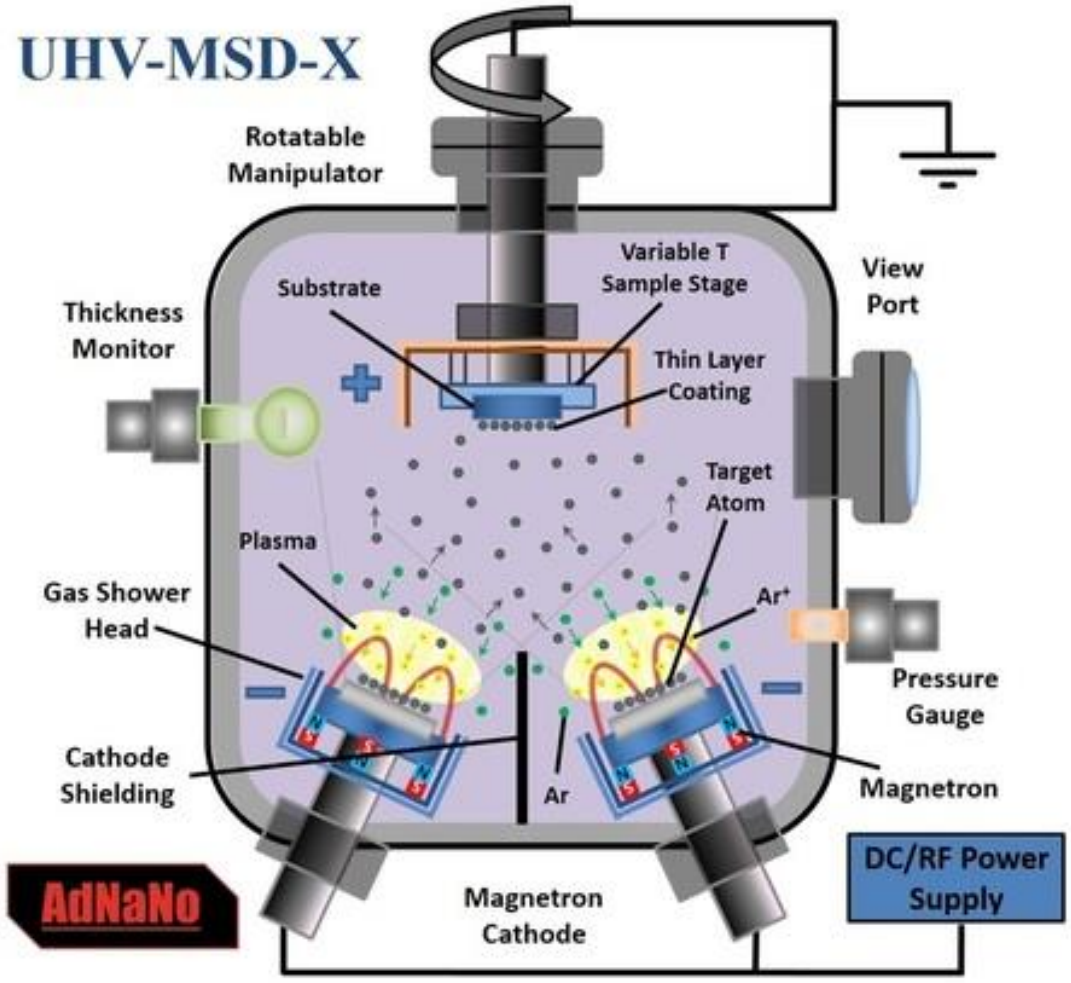

Figure 1. Schematic of a DC/RF magnetron combinatorial sputtering system in operation [2]

or electron beam. Physical deposition techniques, namely sputtering, will be leveraged for thin film growth in this dissertation.

Sputtering

The general concept of sputtering is the physical ejection of particles from a solid surface of a material, known as a "target." The particles are then condensed onto a substrate to create a film. The process begins via the evacuation of a chamber to high vacuum (~$3x10^{-7}$ Torr for our system) to reduce the number of unwanted collisions and impurities during the sputtering process. An inert gas, such as Argon, is then flowed into the chamber near the target and a bias is applied to generate a plasma. The bias can be applied via direct current or alternating current depending on the conductive nature of the target species. The ionized Ar atoms from the plasma are attracted to the negatively biased target, which results in a collision and ejection of target species atoms which forms a physical vapor of the desired element. The atoms are ejected in all directions (with a typical cosine distribution), and thus some are directed toward a substrate in close proximity. The vapor subsequently condenses onto the substrate, thus generating a film [3].

Combinatorial Approach

Combinatorial sputtering can be leveraged as a convenient tool for rapid material discovery as it can achieve thin film compositions that cover a large and tuned composition range. Higher complexity, combinatorial films can be attained through additional sputtering targets and power supplies. Appropriate configuration of the additional sputtering targets can create a wide compositional gradient across a single wafer. Alternatively, the substrate

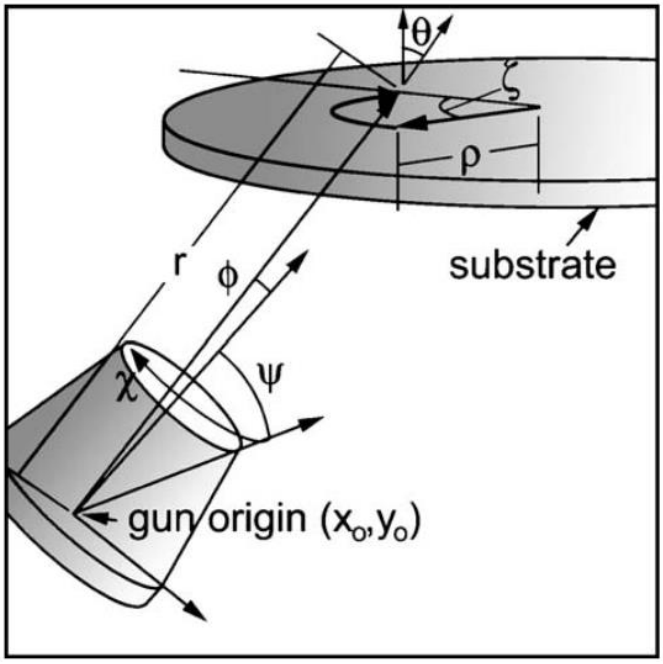

Figure 2. Schematic of the important system parameters taken into account in the sputtering simulation [4]

can be rotated to generate a film of uniform composition and thickness. A schematic of a combinatorial system in operation can be seen in Figure 1. Further, the high energy deposition process and fast cooling rates of the energetic sputtered species allows for the realization of metastable material configurations, for example supersaturated solid solution found in various as-deposited sputtered alloys [5,6]. Subsequent annealing can be utilized to achieve the equilibrium state of the system through recrystallization, grain growth, and phase separation [7,8].

Sputtering Simulation

The high throughput, combinatorial approach to binary and higher order alloy systems will be aided by a computer simulation, which can predict the composition and thickness profiles across a 100 mm wafer. The geometry of the sputtering chamber, the relevant distances, and angles to the substrate holder in our specific chamber are the important variables in the construction of the model. A schematic of the sputtering geometry along with the important chamber geometries is shown in Figure 2 though it should be noted this schematic is not to scale [4].

For this model, the four sputtering guns were modeled as an individual Knudson surface source, where the sputtering flux per unit area is given by the equation [9]:

$$\frac{d\overline{M_S}}{dA_S} = \frac{\overline{M_T}(n+1)cos^n\phi cos\theta}{2\pi r^2} \quad (1)$$

where dM_s/dA_s is the mass deposited per unit area, M_T is the total sputtered mass from the target, ϕ is the angle between the target surface normal and a line extending from the center

of the target to a fixed point on the substrate surface, and n is the degree of flux forward peaking. Due to the targets being placed inside 50 mm tall stainless steel chimneys to avoid cross-contamination, the value of n has been determined experimentally to be ~12 [4]. In our system, the sputtering guns are not perpendicular to the substrate; therefore, θ is introduced as the angle between the substrate surface normal and a line extending from the center of the target surface to a set point on the substrate surface. Finally, r is the distance from the center of the target to a fixed point on the substrate surface. Good agreement has been shown previously between the simulated and experimental composition and thickness profiles [5,6,10]. To account for the multi-element targets to be utilized in this investigation, the duplicate Knudson surface sources were overlapped so that there were two (or more) sources at each gun location to account for multiple species being sputtered. The flux from these targets were then split between the two sources according to the atomic ratios within the alloy target. More complex alloy targets can be estimated similarly.

Bulk Synthesis

Once compositions of interest are identified through the combinatorial approach, bulk samples will be generated through arc casting with an Arcast Arc 200 Cold Crucible Arc Melting Furnace. Compositions will be weighed out from pure element constituents and Al-based master alloys. 60 g to 100 g charges will be used based on the target composition (alloy versus pure intermetallic, respectively) and mold geometry. Once the charge is loaded, the chamber will be evacuated and backfilled with Argon. This evacuation/backfill procedure is repeated three times to reduce the partial pressure of atmospheric gases that can contaminate the alloy. The charge is then melted, mixed, and flipped until the materials

are fully integrated. At this point, the molten material is tilt poured into a predetermined mold geometry and allowed to cool. Subsequently, the sample will be prepared for a variety of tests including SEM, XRD, EDS, indentation, and scratch testing.

Coefficient of Thermal Expansion

The coefficient of thermal expansion (CTE) is a material phenomenon that is defined by a material's dimensional response to an exterior, applied heating or cooling source. This phenomenon is critical to processes at elevated temperatures as the change in dimension with temperature affects operational tolerances and if excessive, can lead to failure [11,12]. Additionally, for parts that have cyclic temperatures, the induced thermal stresses can cause thermal fatigue, which can lead to the formation of defects and ultimately failure [13]. The linear coefficient of thermal expansion, α, is defined as:

$$\alpha = \frac{(L-L_0)/L_0}{(T-T_0)} \tag{2}$$

where L_0 is the original dimensional length at the nominal temperature T_0, and L is the dimensional length after expansion by changing the temperature of the system to temperature T. Similarly, the volumetric coefficient of thermal expansion, β, is defined as:

$$\beta = \frac{(V-V_0)/V_0}{(T-T_0)} \tag{3}$$

where the change in volume is measured rather than a singular dimension, L. For isotropic materials:

$$\beta = 3\alpha \tag{4}$$

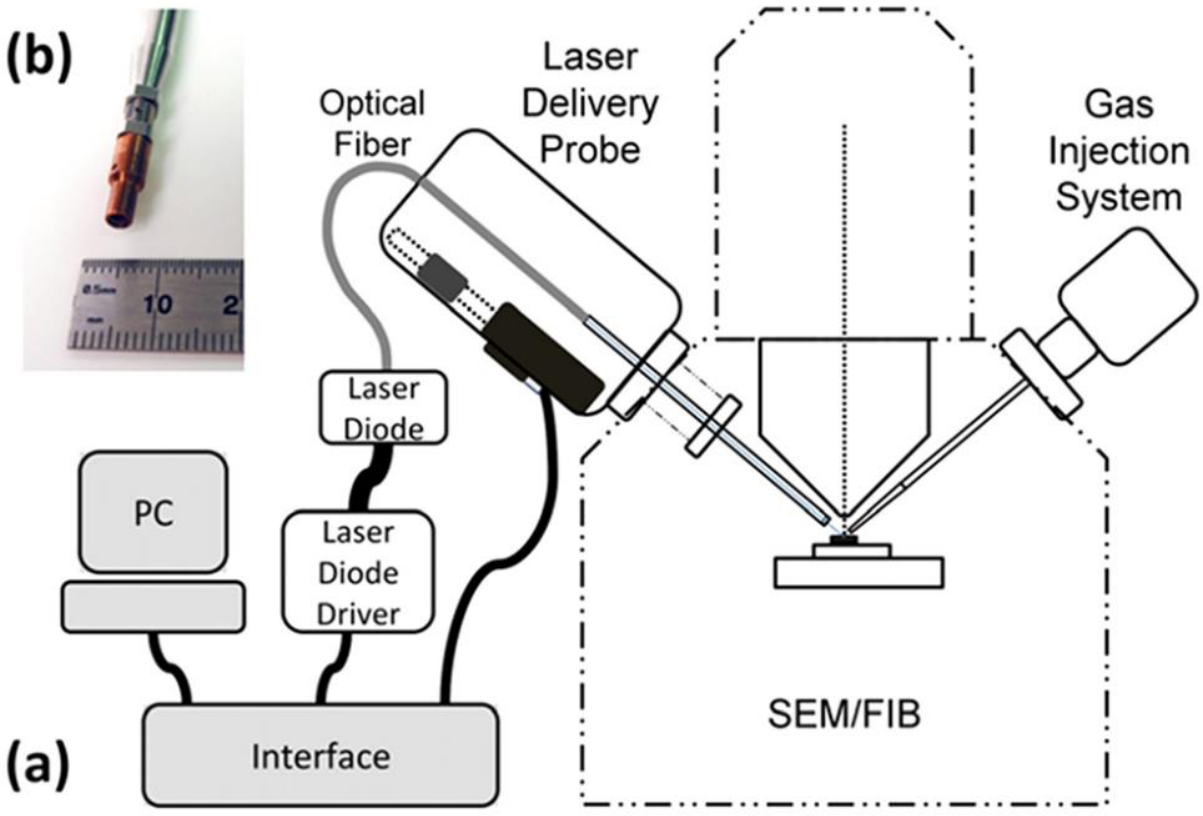

Figure 3. Schematic of the optical delivery system to be utilized in this project [14]

which holds true at singular temperature instances but is more complex over a temperature range.

Laser Annealing

Material processing utilizing high power laser diodes have been routinely performed for several decades now with the first report coming in 1991 for soldering [15]. Since then, the use of laser systems for processing has expanded to include transformation hardening, welding, surface melting, engraving, machining, sintering, and thermal annealing among others [16,17]. Combining *in situ* laser processing with a scanning electron microscope and/or a focused ion beam allows for sample heating and enhanced ion beam induced deposition or laser assisted chemical vapor deposition which has been demonstrated previously [18,19]. Further, this combination allows for real time monitoring of microstructural development or film dewetting as well as characterization of the chemical (EDS) and structural (BSD) makeup of the film. A schematic of the optical laser system that will be leveraged in this study can be seen in Figure 3. The spot size of this laser is approximately 100 microns which allows for localized annealing of the film and temperature gradient effects to be investigated.

Literature Review

Thin films for rapid material discovery

Combinatorial physical vapor deposited films can be leveraged as a rapid materials discovery and optimization process in mechanical alloy design. This is done through the synthesis of a wide targeted composition range in combination with high throughput

screening methods to enhance understanding of composition-structure-property relationships to identify compositions with desired properties [20,21]. This approach was first developed in the 1960's as a way to explore isothermal ternary phase diagram spaces [22] and was further realized to search for new superconducting materials [23]. Since then, this technique has been employed for a variety of material discovery processes. One of the primary use cases for the combinatorial approach is in the development of functional materials such as the superconducting materials previously mentioned. Other work in this area includes transducer materials [24], hydrogen storage [25], fuel cell electrodes [26,27], and lithium-ion battery electrodes [28]. Another interesting use case of thin films for rapid alloy assessment is for optical data storage utilizing phase change materials [29,30]. In the post-Covid onset world, anti-microbial material properties have also been of interest. The rapid solidification into metastable materials and the discovery process utilizing thin films can be used to investigate these properties [31] to limit transmission of pathogens in high traffic touch surfaces such as doorknobs, countertops, and handrails among others. The combinatorial thin film approach also allows for sustainable development of new alloys. Traditional bulk metallurgy techniques have high time, energy, and material demands. However, the combinatorial approach reduces all three of these demands allowing for a faster, more sustainable methodology [32]. Once composition ranges of interest have been identified more conventional methodologies can be leveraged to establish the structure-processing-properties relationship.

Combinatorially synthesized films have also been utilized in mechanical alloy design for mechanical, thermal, and corrosion property as well as microstructure determination. It has

been proven to be a powerful tool in understanding the composition-structure-property relationship and identify composition ranges of interest for enhanced or unique material properties [33]. Previously, Al-Si alloys have been investigated using the combinatorial thin film technique. Al-Si alloys are of interest especially in the automotive industry due to their high strength-to-weight ratio, thermal conductivity, and thermal expansion [34]. This system has thus been further investigated to understand the role of Si content on the mechanical properties as well as influence on microstructure. Olk *et. al.* investigated Si contents from approximately 15 to 85 at.% Si combinatorially and showed a strong dependence of phase formation and hardness on the Si content [35]. Further work by this group investigated the microstructure and the ability to tune it in the Al-Si system. Here they showed that an amorphous phase a-(Al–Si) and a mixed phase a-Si + c-Al containing a tunable Al grain structure and systematically engineer the sample surface can be produced [36]. This work was done in parallel with nanoindentation to aid in identifying new compositions regions of interest. Combinatorial, nanoindentation work has also been performed in the Ti-Al system. One study explores this system from ~0 to 35 at.% Al with near uniform thickness of around 900 nm and demonstrates that thin films can be leveraged to track mechanical property changes over a composition gradient using nanoindentation [37]. Further studies have been performed to understand the interaction effects between the film and substrate on mechanical property determination. As expected, the interaction is dominated by the thickness of the deposited film. However, parameters can be adjusted and thickness-corrections applied to accommodate the substrate interaction zone [38,39]. Additionally, corrosion behavior can be effectively investigated utilizing the combinatorial

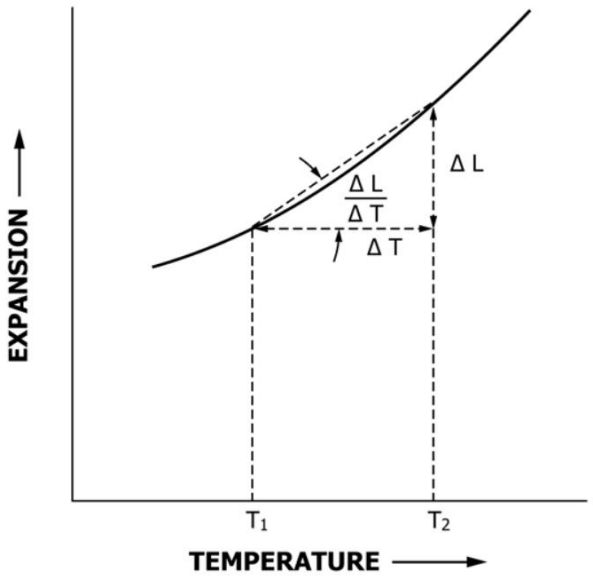

Figure 4. Sample graph of expansion versus temperature from thermomechanical CTE measurements [40]

thin films rapid material discovery technique [41]. This approach has been applied to a variety of alloy classes. High Entropy Alloys (HEAs) have been investigated using this technique as the optimization and development of these alloys can prove difficult and time consuming using conventional metallurgical techniques [42].

Coefficient of thermal expansion determination

A variety of techniques have been utilized to investigate the coefficient of thermal expansion of a given bulk material [43]. ASTM standard E831 covers thermomechanical analysis techniques for CTE determination of bulk materials [40]. This methodology can be used in a temperature range from -120^{o}C to 900^{o}C for ~10 mm test specimens with CTEs higher than 5x10^{-6} /K when subjected to a constant heating rate of 5^{o}C/min over a desired temperature range. The apparatus consists of a rigid specimen holder – with a low, known CTE, rigid expansion plate, sensing element, wight or force transducer, furnace, temperature controller, temperature sensor, means of sustaining an inert atmosphere, a data collection device, and a micrometer. The data is collected electronically, and a plot as shown in Figure 4. Sample graph of expansion versus temperature from thermomechanical CTE measurements [40] is generated. The mean CTE is then extracted using equation 2 after which a correction can be performed to remove the substrate interaction. For greater accuracy, a more detailed method utilizing push rods is established in ASTM standard E228 [44].

For thin films, a different strategy needs to be employed. Due to the dimensional limitations of a thin film, conventional dilatometry and optical techniques cannot be applied to films.

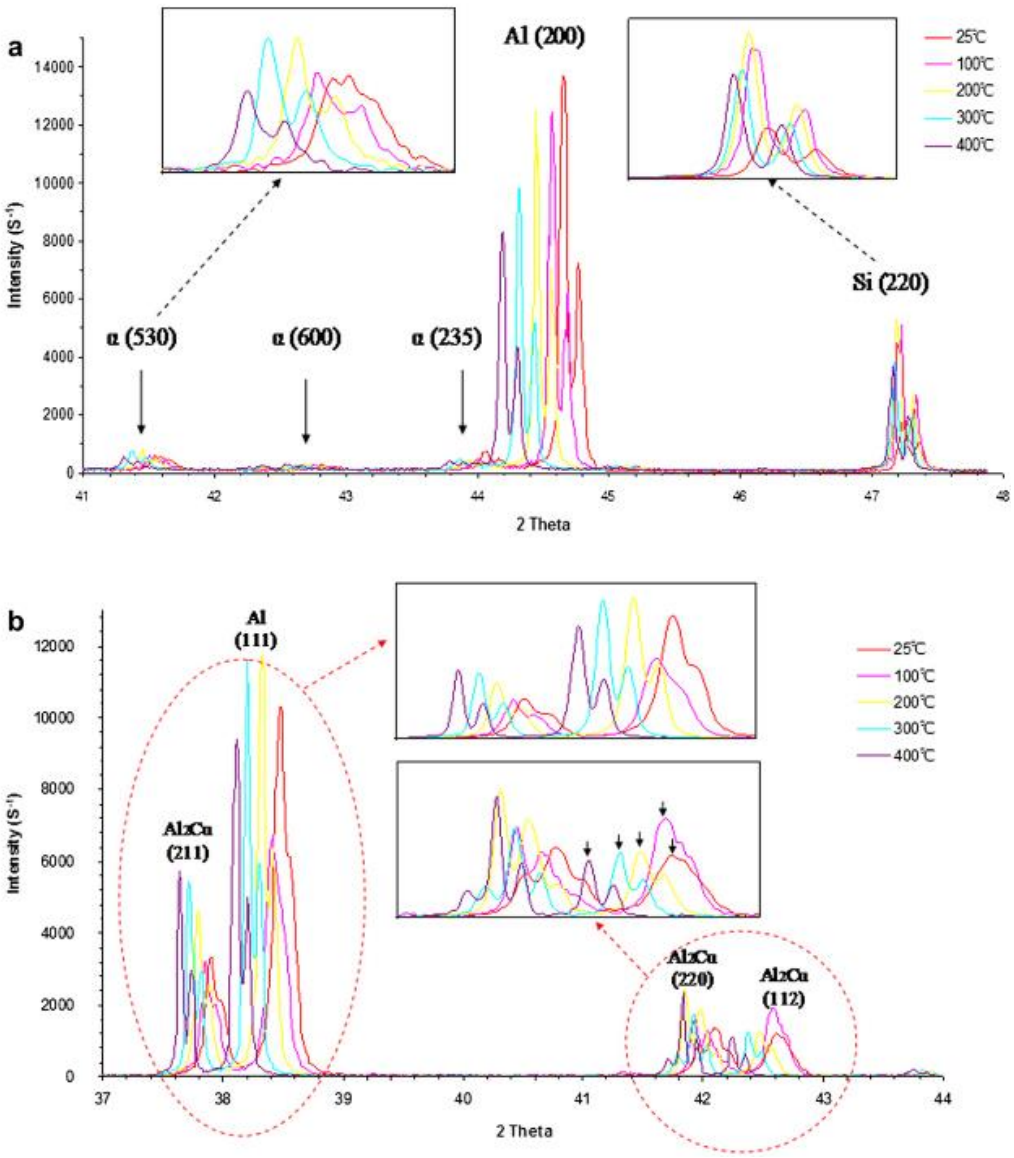

Figure 5. Sample TDXRD pattern that identifies several phases from [45]

One common technique is non- ambient or temperature-dependent x-ray diffraction (TDXRD). In this approach, x-ray diffraction is used to determine the lattice parameters of the phases present and the changes to those lattice parameters over a given temperature range. A variation of equation 2, replacing length with d-spacing, is used to calculate CTE from TDXRD data. These parameters can be extracted from peak positions based on Bragg's law or through a Rietveld refinement program. This approach also allows for the investigation of anisotropy in the coefficient of thermal expansion. Previous work with pure Cu, Ni, and Pd deposited on Si substrates shows that the thin film CTE values are consistent with bulk values once annealed to allow for the relief of stress in the film generated during deposition [46]. However, there are concerns about substrate interaction effects on the CTE of the film. Another previous work investigating Ag films on two different substrates (SiO_2 and PEN), studied thickness dependency of CTE value. It was determined that a Poisson correction can be applied to CTE values for films thinner than ~300-350 nm which accounts for the CTE mismatch between the film and substrate making it consistent with bulk values [47]. The more standard dilatometry techniques will be utilized for bulk alloys generated based on the films to determine the composite CTE value.

The temperature-dependent x-ray diffraction approach has also been utilized for bulk materials in studying thermal expansion of alloy systems with intermetallics. A novel characteristic of this technique is that the thermal expansion of individual phases can be determined rather than only the bulk composite CTE value [48]. It should also be noted that the phases are shown to expand independently. This technique has already been leveraged in investigating Al-based alloy systems [45]. In this investigation, several

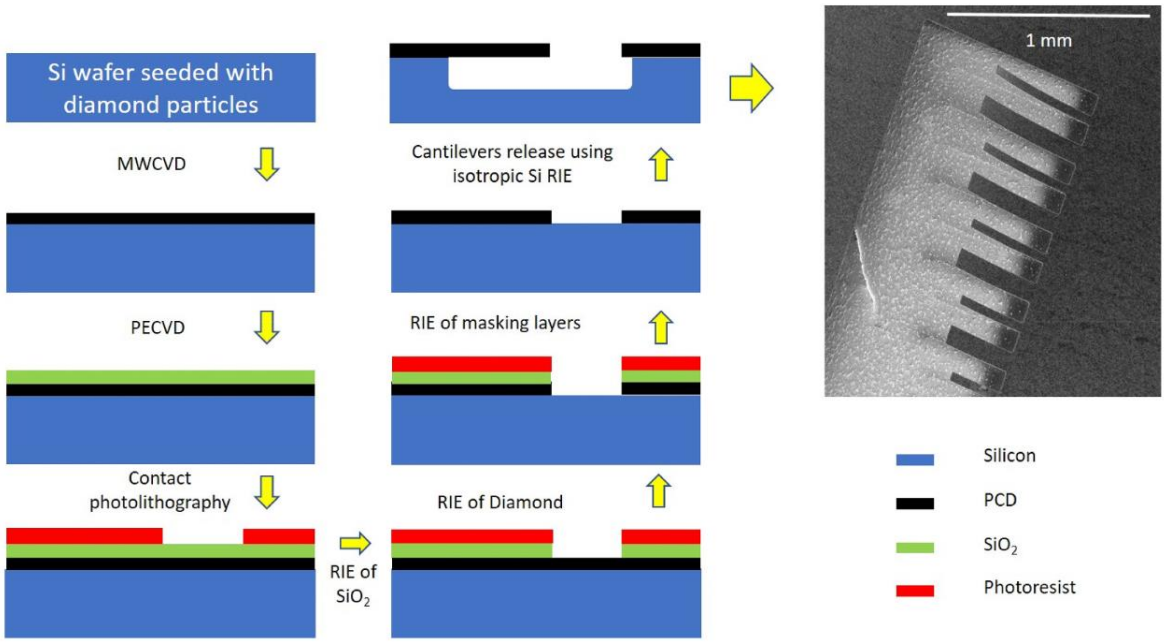

Figure 6. Cantilever preparation process and resulting structure from diamond films for thermal property determination [49]

intermetallics were formed including: Al_2Cu, Al_3Ni, $Al3Ni_2$, Al_7Cu_4Ni, Al_9FeNi and α-AlFeMnSi. Peak shifts in the combined TDXRD pattern allow for the determination of the CTE of each individual phase. Through Rietveld refinement, the average across all peaks for a given phase can be determined as well of the phase fraction to estimate the bulk CTE value. An example TDXRD pattern is shown in Figure 5. Sample TDXRD pattern that identifies several phases from [45]. Post-thermal cycling SEM imaging can reveal deformation due to phase CTE mismatch.

Another technique to be considered for CTE determination of thin films employs micromachined cantilever structures [50]. One benefit of this approach is that it can be applied more broadly to non-crystalline materials. The microcantilevers are generated using a process similar to the one shown in Figure 6. Cantilever preparation process and resulting structure from diamond films for thermal property determination [49]. For a cantilever structure, when the temperature is raised by some ΔT, the length of the cantilever changes on the free end by some corresponding ΔL. Thus, the coefficient of thermal expansion, α, can be calculated using:

$$\Delta L = \alpha L_0 \Delta T \tag{5}$$

where L_0 is the initial length of the structure. However, the change in length corresponding to a 100°C change in temperature for a 200 micron long SiO_2 cantilever is approximately 0.01 microns [50] which cannot be measured accurately by optical methods. The beam out-of-plane deflection alternatively can be measured directly by optical means and related to the CTE value. Further the microcantilever approach can be leveraged to measure thermal conductivity [49,51]. Factors such as film thickness and deposition parameters have also

been shown to influence the experienced CTE value in films [52]. As such, these variables should be taken into account when growing the film.

CHAPTER I

THIN FILM COMBINATORIAL SPUTTERING OF AL-CE ALLOYS: INVESTIGATING THE PHASE SEPARATION OF AS-DEPOSITED SOLID SOLUTIONS AND DETERMINING THE COEFFICIENT OF THERMAL EXPANSION

Thin film combinatorial sputtering of Al-Ce alloys: Investigating the phase separation of as-deposited solid solutions and determining the coefficient of thermal expansion

Reece Emery[1], Orlando R. Rios[1], Michael J. Thompson[1], David Weiss[2], Philip D. Rack[1,3,*]

1. Department of Materials Science and Engineering, University of Tennessee, Knoxville, Tennessee 37996, USA
2. Eck Industries, Manitowoc, Wisconsin 54220, USA
3. University of Tennessee – Oak Ridge Innovation Institute, Knoxville, Tennessee 37996, USA

*corresponding author: prack@utk.edu

Keywords: combinatorial sputtering, thin films, rare earth alloys and compounds, thermal expansion, x-ray diffraction

Author Contributions

This work was originally published in the Journal of Alloys and Compounds. The author of this dissertation was the lead writer and experimentalist for this paper. Synthesis of the film as well as all characterization of the samples including scanning electron microscopy (SEM), x-ray diffraction (XRD), and 4-point probe resistivity measurements were performed by him. Collaborator Michael Thompson fabricated the bulk samples used in this study using feedstock material generated by collaborator David Weiss. The author performed all data analysis, interpretation, writing, and figure generation for the results included in this paper.

Abstract

Al_xCe_{100-x} thin films with a composition range of ~75.0<x<99.5 at. % (36.5<x<97.5 wt. %) were synthesized via combinatorial co-sputtering from an Al and an $Al_{50}Ce_{50}$ target. The crystal structure, phase fraction, film morphology, electrical resistivity, and temperature-dependent coefficients of thermal expansion (CTE) are all correlated to the Al_xCe_{100-x} composition. The as-deposited films form a metastable solid-solution, and annealing leads to the formation of the thermodynamically stable two-phase system of Al and the α-$Al_{11}Ce_3$ intermetallic. Temperature dependent x-ray diffraction (XRD) reveals that the two phases expand independently of one another, and the thin film Al temperature-dependent CTE is similar to bulk Al. The thin film $Al_{11}Ce_3$ intermetallic phase has a nearly constant CTE of ~$1.5x10^{-5}$/°C within the temperature range studied (25-550ºC). To confirm the thin film $Al_{11}Ce_3$ results, bulk stoichiometric $Al_{11}Ce_3$ and +/- 1 wt.% Ce samples were prepared and the CTE of each was measured with the same conditions. A Rietveld analysis of the bulk data enabled an estimation of the CTE in each of the 3 orthorhombic lattice parameters, which displayed anisotropic behavior. The thin film and bulk CTE measurements were in very good agreement. Estimations of the temperature dependent CTE of the two-phase alloys are made via the Reuss and Voigt models. By demonstrating the efficacy of the approach, more complex multi-component rapid materials discovery of low CTE Al-alloys can be pursued via the combinatorial thin film synthesis and XRD measurement.

Introduction

Alloying aluminum with cerium in the range of 6-16 wt. % (1.2-3.5 at. %) has recently been shown to significantly improve the high temperature mechanical properties,

castability, and thermal stability relative to existing aluminum alloys [53,54]. Traditional aluminum alloys have been of interest in the automotive industry where factors such as weight, high-temperature performance, and cost play an important role in determining attainable fuel efficiency. Existing aluminum alloys meet the weight and cost requirements; however, they lack the necessary high-temperature performance required as the demand for higher power throughput and fuel efficiency continues to increase. Cerium-based aluminum alloys have been shown to maintain the weight and cost-savings of traditional aluminum alloys while providing high-temperature stability due to the formation of intermetallic phases [55–57]. Recently, the Al-Ce alloy system has also been of interest as a surface coating for corrosion resistance [58,59] where it has been shown that the Al-Ce alloy system creates a Ce-rich outer passivation layer, which limits the reduction of the Al matrix [60].

Al has a face-centered cubic (FCC) structure with a lattice parameter of 4.04 Å [61]. Cerium has been shown to crystallize in two forms at ambient temperatures and pressure. One is an FCC structure with a lattice parameter of 5.14 Å while the other is a hexagonal close-packed (HCP) structure with a=3.65 Å, and c= 5.91 Å [62]. This leads to limited solubility in the alloy system. However, the system readily forms several intermetallics. In the composition region of interest, (<21.5 at.% Ce), the Al-Ce alloy system forms a two phase region with a pure Al matrix and the $\alpha Al_{11}Ce_3$ intermetallic. $\alpha Al_{11}Ce_3$ forms an orthorhombic structure with a=4.39 Å, b=10.08 Å, and c=13.02 Å [63].

The coefficient of thermal expansion (CTE) is an important parameter in high temperature applications as the change in dimension with temperature affects operational tolerances

and if excessive, can lead to failure. Additionally, for parts that have cyclic temperatures, the induced thermal stresses can cause thermal fatigue. Temperature-dependent x-ray diffraction (XRD) is one technique that can be used to quantify the CTE of a material. In this technique, the CTE is determined through changes in the interplanar spacing with changes in temperature [64]. Using this technique, it has been shown that the CTE decreases with increasing grainsize [46], and that various phases can be measured simultaneously [45]. Furthermore, CTE anisotropy has been explored by comparing various reflections in non-cubic systems [48,65].

Combinatorial sputtering can be leveraged as a convenient tool for rapid material discovery as it can achieve thin film compositions that cover a large and targeted composition range. Further, the high energy deposition process and fast cooling rates allows for the realization of metastable material configurations, for example supersaturated solid solution found in various as-deposited sputtered alloys [5,6]. Subsequent annealing can be utilized to achieve the equilibrium state of the system through recrystallization, grain growth, and phase separation [8,66]. The motivation of the study is to demonstrate that thin film combinatorial synthesis can be used for alloy development. In particular, we apply the thin film rapid materials discovery approach to a new alloy system ($Al_xCe_{100-x)}$ that is being explored for various lightweight alloy applications. The coefficient of thermal expansion (CTE) is a critical property to various high-temperature applications and thus we use the thin film approach to extract the CTE of the $Al_{11}Ce_3$ intermetallic to determine its suitability. Thus, a combinatorial library of Al_xCe_{100-x} ($\sim 75.0 < x < 99.5$ at. %) alloys is co-sputter deposited and the crystal structure and phase fraction, film morphology, effective electrical

resistivity, and temperature-dependent coefficients of thermal expansion are all correlated to the Al_xCe_{100-x} composition.

Material and methods

Sputtering Conditions

Al_xCe_{100-x} alloys were co-sputtered from a pure Al and a $Al_{50}Ce_{50}$ (50-50 at.%) target to form a combinatorial library across a SiO_2-coated (500 nm) Si substrate (500 μm). The substrate was fixed and not rotated to generate the composition gradient. The Al target was powered with a 200 W DC source while the $Al_{50}Ce_{50}$ target was powered with a 100 W RF source in a 5 mTorr Ar ambient atmosphere for 2 hours.

X-Ray Conditions

Room temperature x-ray diffraction (XRD) patterns were measured using a Malvern Panalytical X'Pert3 MRD diffractometer while temperature-dependent XRD experiments were performed using a Malvern Panalytical Empyrean diffractometer. A 2θ-ω scan with an ω offset of 3° with a Cu tube (λ=0.154 nm) was used for all experiments. Room temperature XRD experiments on an as-deposited and an annealed sample were run with an angle sweep from 25° to 85° with a step size of 0.52° (total time of each scan 30 min). To estimate the coefficient of thermal expansion, we performed temperature-dependent x-ray diffraction experiments with an angle sweep from 20° to 110° with a 0.26° step size (total time of each scan 23 min). The sample was heated *in situ* from room temperature (~25°C) to 550°C in a nitrogen atmosphere with a heating rate of 5°C/min. The sample was held for 5 minutes at 100, 200, 300, 400, 500, and 550°C after which each XRD

measurement was taken. The same conditions were used during the cooling cycle. In total, thirteen measurements were taken for each temperature cycle.

Annealing Conditions

Annealing was conducted in vacuum with a base pressure of ~$3x10^{-7}$ Torr. The sample was ramped from room temperature (~15°C) to 500°C over a period of 1 hour. It was held at 500°C for 10 minutes and then reduced to 475°C and 450°C and held for 5 and 15 minutes, respectively. The sample was cooled at a rate of 10°C/min from 450°C to 200°C at which point the heater was turned off and the sample was left to cool to room temperature overnight.

Scanning Electron Microscopy and Energy dispersive X-ray spectroscopy

Energy dispersive x-ray spectroscopy (EDXS) and scanning electron microscopy (SEM) were conducted on a Carl Zeiss MERLIN SEM. The combinatorially sputtered Al_xCe_{100-x} thin film (as-deposited and annealed) was measured at 9 points at equally spaced increments of 10 mm along the composition gradient. An accelerating voltage of 10 keV was used for EDXS.

4-Point Probe Measurements

Resistivity measurements were performed using a Lucas Labs Pro4-440N QuadPro Resistivity System with a Keithley 2400 Source Measurement Unit. Resistivity was calculated by multiplying the experimental resistance measurement by the film thickness. Film thickness values were taken from the simulated thickness profile in figure 1d.

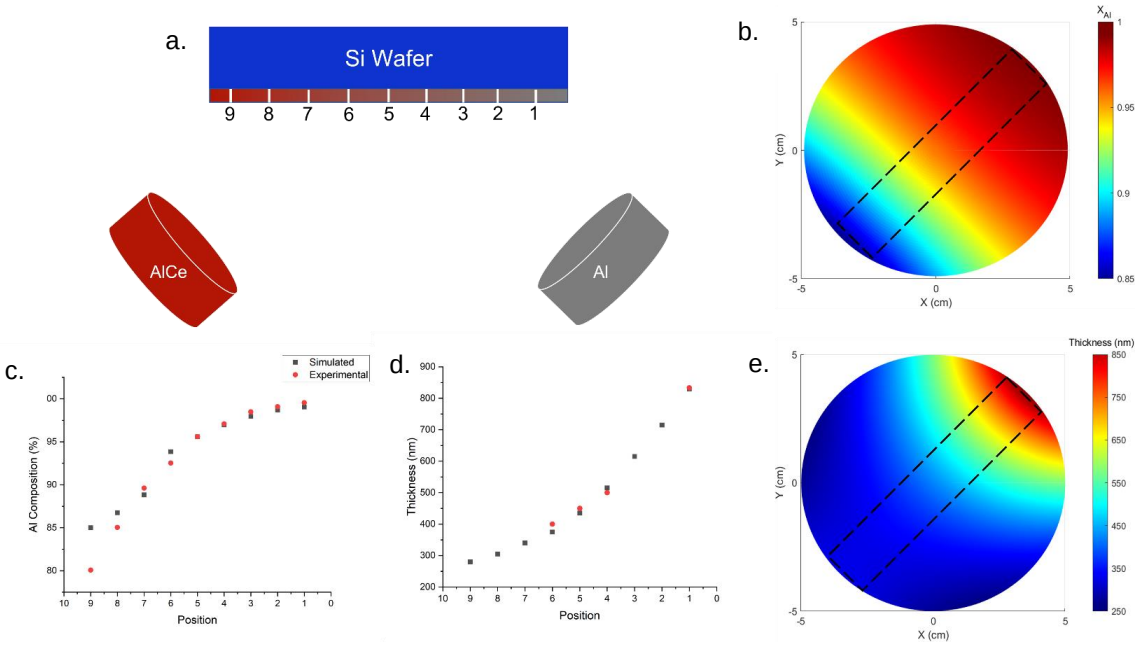

Figure 7. (a) Schematic of sputtering configuration. (b) Simulated Al composition of the Al-Ce combinatorially sputtered 100 mm diameter film. Comparison of simulated versus experimental (c) composition and (d) thickness. (e) Simulated film thickness of the Al-Ce combinatorially sputtered 100 mm diameter film. Dashed black box denotes area of study.

Results and Discussion

Full Wafer Characterization

Figure 7a is a schematic of the sputtering configuration used to synthesize the Al_xCe_{100-x} thin films. Since the substrate is not rotated and the flux from the targets are different, both a composition and thickness gradient are generated, respectively. For reference, position 0 is at the aluminum rich wafer edge and positions 1-10 proceed in 10 mm increments across the wafer diameter along the gradient to the Ce-rich wafer edge. Figure 7b also illustrates the simulated [4] Al composition across the entire substrate and 7c) the simulated versus experimental EDXS measured film composition and the 7d) simulated and SEM measured thickness along the gradient diameter centerline. The simulations assumed a substrate center (position 5) Al and $Al_{50}Ce_{50}$ deposition rate of 3 and 0.75 nm/min, respectively. Figure 7c and 7d show good agreement between the experimental and simulated composition and thickness, respectively. Figure 7e shows the complementary thickness as a function of the substrate position for the entire substrate.

To confirm the crystal structure of the as-deposited and annealed combinatorially sputtered Al_xCe_{100-x} thin films, x-ray diffraction (XRD) was conducted at positions 1-6 (starting at 10 mm from the Al-rich edge and measuring every 10 mm) and position 8 as shown in Figure 8. For x>97.0, the Al (111) reflection dominates with trace reflections of the (222) plane. A shift in 2θ and broadening in the Al (111) peak suggests the formation of a metastable solid solution for the as-deposited sample, which appears evident up to position 5 (x=95.5). For x<=97 (or approximately the hypereutectic region) the x-ray intensity

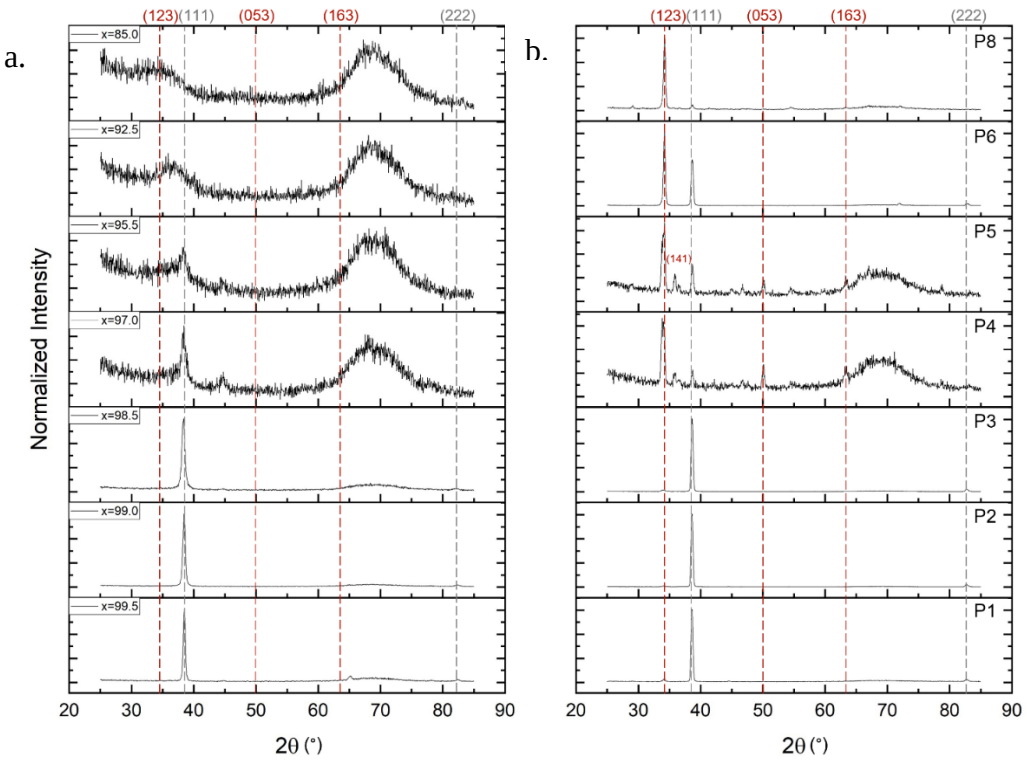

Figure 8. XRD results for Al_xCe_{100-x} films for (a) as-deposited and (b) annealed samples. Grey lines denote Al peaks. Red lines denote $Al_{11}Ce_3$ peaks [67]

drops as evidenced by the low signal to noise. A broad amorphous hump emerges at ~ 70° an(a. :tributed to the amorphous $Al_{11}Ce_3$ phase, which has reasonable phase fraction in this region. The $Al_{11}Ce_3$ is fairly refractory as it has an incongruent phase transformation to Al_4Ce and Al_3Ce at ~1000°C [68], thus the rapid solidification that occurs during the sputtering process inhibits crystallization of this phase at room temperature. The Al (111) peak is very broad and shifted to lower 2θ up to x=95.5 consistent with the solid solution formation; at x> 92.5 it is unclear if there is any long range order in the material as the phase fraction is dominated by the $Al_{11}Ce_3$ which appears to be amorphous. To confirm the observed results as-deposited results are consistent with no phase separation EDS maps of various compositions were measured which confirmed the homogeneous distribution of the Al and Ce (see supplemental information 1). After annealing, the $Al_{11}Ce_3$ intermetallic phase emerges and the peak ratio of the Al (111)/$Al_{11}Ce_3$ (123) decreases consistent with the expected increase in the $Al_{11}Ce_3$ phase fraction with increasing Ce content. Note that the (111) orientation in FCC crystals have a preferred orientation due to the low surface energy [69]. As expected, the aluminum peak intensity increases, narrows, and shifts back to its expected position (higher 2θ) consistent with rejection of the Ce in Al phase (note confirmation of this in temperature dependent x-ray diffraction below). The recrystallization for 97.0<x<95.5 seems to be robust as the x-ray diffraction intensity for the Al (111) (for x>97) and $Al_{11}Ce_3$ (123) (for x<95.5) peaks are high. Interestingly, the recrystallization for the x=97 and 95.5 compositions seem sluggish as the signal to noise in the diffraction data is low and the amorphous peak at ~ 70° is relatively high.

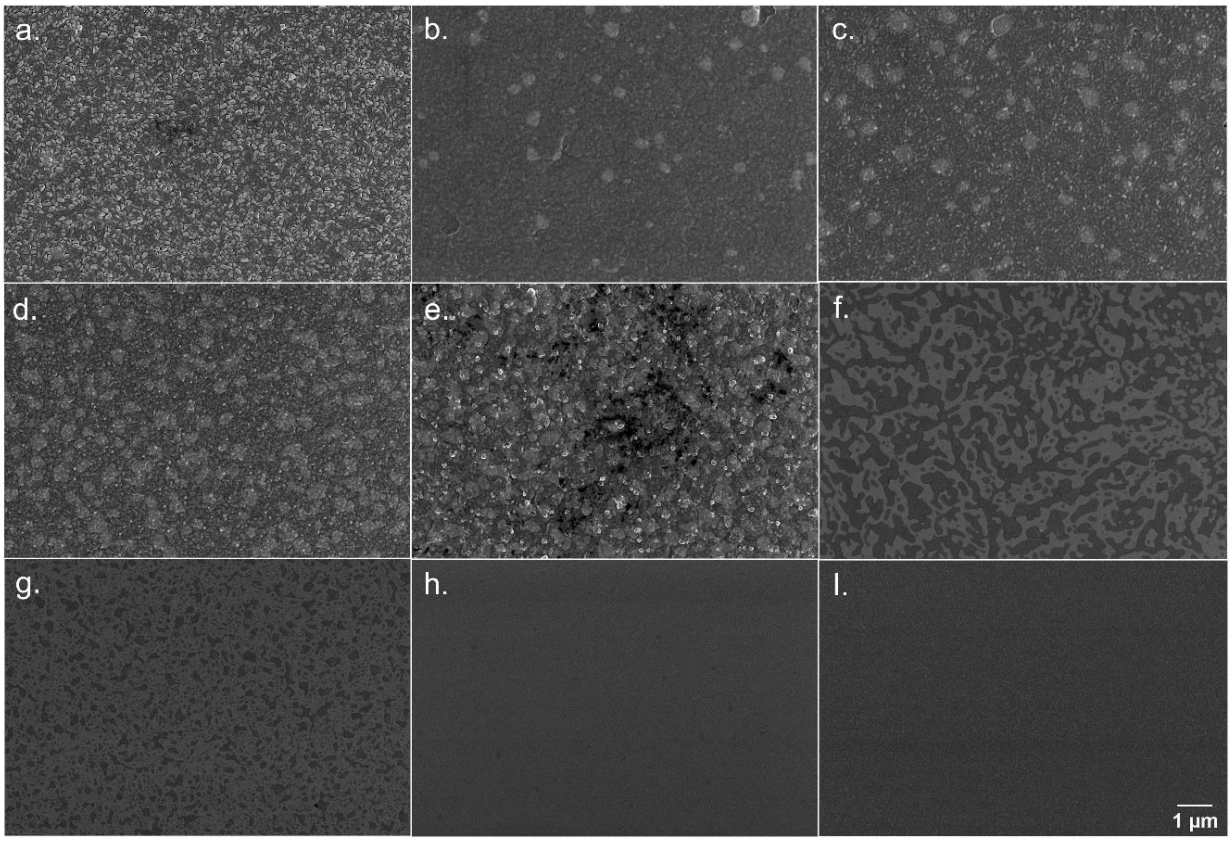

Figure 9. Plane view SEM images of the annealed films where (a) $Al_{99.5}Ce_{0.5}$, (b) $Al_{99.0}Ce_{1.0}$, (c) $Al_{98.5}Ce_{1.5}$, (d) $Al_{97.0}Ce_{3.0}$, (e) $Al_{95.5}Ce_{4.5}$, (f) $Al_{92.5}Ce_{7.5}$, (g) $Al_{89.5}Ce_{10.5}$, (h) $Al_{85.0}Ce_{15.0}$, and (i) $Al_{80.0}Ce_{20.0}$.

Figure 9 show the SEM images of annealed Al_xCe_{100-x} films (see supplemental information for as-deposited films). As noted in the progression to higher Ce concentration, the emergence of a second phase with higher secondary electron yield emerges. EDS maps confirmed that the brighter second phase contains cerium and thus assigned to the equilibrium $Al_{11}Ce_3$ phase. Clearly the phase fraction of the $Al_{11}Ce_3$ phase fraction increases with increasing Ce content as expected and as observed in the XRD. An estimation of the phase fraction was determined via image processing and good agreement between the estimated $Al_{11}Ce_3$ and Al phase fraction versus the phase fraction calculated from the phase diagram was obtained (see supplemental information for a plot of the estimated versus calculated phase fraction). In Figure 9a the $Al_{11}Ce_3$ is not evident in the SEM image, but small precipitates on the order of a 50-200 nm emerge in 9b and the size and number grow from 9c and 9d, respectively. The contrast in 9e shows clear precipitation, but the intergranular Al region is not as dark in the image. Note there is a significant transition in the microstructure in figure 9e to 9f where the $Al_{11}Ce_3$ grain size increases and is interconnected. Interestingly this is consistent with the enhanced crystallization observed at higher Ce content in position 6 observed in the x-ray diffraction. This enhanced transformation at this composition will be studied in the future.

Resistivity Measurements

The composition and microstructure were also correlated to the resistivity as shown in Figure 10. The resistivity of the as-deposited sample increases with increasing Ce content. As described above, the Al_xCe_{100-x} alloy forms a solid solution up to ~x=95.5 and at higher Ce content appears to be in an amorphous phase. Thus, increase in resistivity in the as-

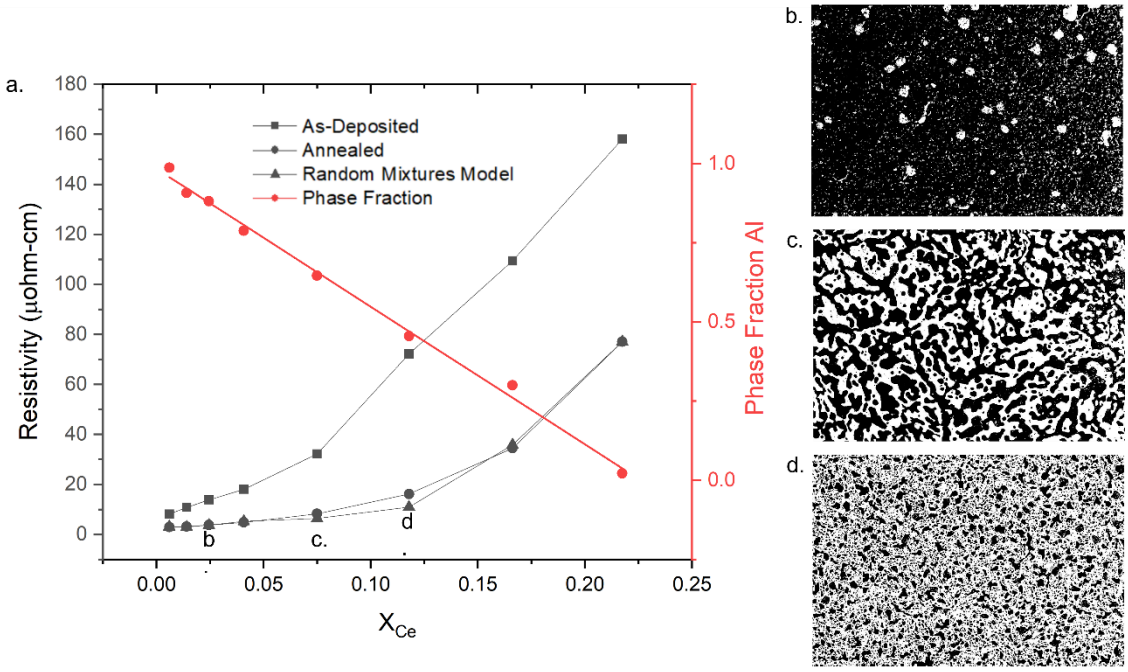

Figure 10. (a) Resistivity (left axis) and phase fraction (right axis) as a function of Cerium content for the as-deposited and annealed sample as well as the resistivity calculated via a random mixture model. Micrographs after thresholding for (b) $Al_{98.5}Ce_{1.5}$*, (c)* $Al_{92.5}Ce_{7.5}$*, and (d)* $Al_{87.5}Ce_{12.5}$*. White regions are the* $Al_{11}Ce_3$ *phase while the black regions are the Al phase*

deposited phase up to $X_{Ce} = 4.5$ is due to solid solution effects; cerium has lower resistivity than aluminum and the size mismatch strains the lattice which decreases the resistivity. Beyond that composition, the slope changes slightly and the as –deposited resistivity is that of the amorphous Al_xCe_{100-x} phase which could be an amorphous form of sub-stoichiometric $Al_{11}Ce_3$ (cerium deficient for $4.5<X_{Ce}<21$). For the annealed sample, the resistivity increases slowly until 7.5 at. % Ce after which there is a sharp increase in the resistivity. As shown in Figure 9, upon annealing, the system phase separates into a low resistivity Al phase and higher resistivity intermetallic phase. Note that because we are in a two-phase system in the annealed film, the resistivity is an effective medium approximation of the two constituent phases. In this equilibrium state, for Ce content less than 10.5 at. %, the current is carried by the percolating Al network. Image analysis revealed that at the $Al_{92.5}Ce_{7.5}$ composition, the Al phase fraction is ~55%, which supports the percolating Al network. The image analysis suggests the Al phase fraction is only 38% at $Al_{89.5}Ce_{10.5}$ and 5% at $Al_{85.0}Ce_{15.0}$. Thus, at aluminum concentrations higher than $Al_{92.5}Ce_{7.5}$, the current has a percolating path to travel through the aluminum phase, however as the intermetallic phase fraction increases above this concentration, the percolating network closes off thereby increasing the resistivity. A random mixtures model [70] was applied using the phase fractions estimated via the image analysis. The constituent resistivities were taken to be 2.65 μohm-cm for Al [71] and was determined experimentally to be ~77 μohm-cm for the $Al_{11}Ce_3$ intermetallic which is consistent with literature values [72]. Very good agreement between the model and experimental phase separated resistivity values. This suggests that a random combination of series and parallel connections exist

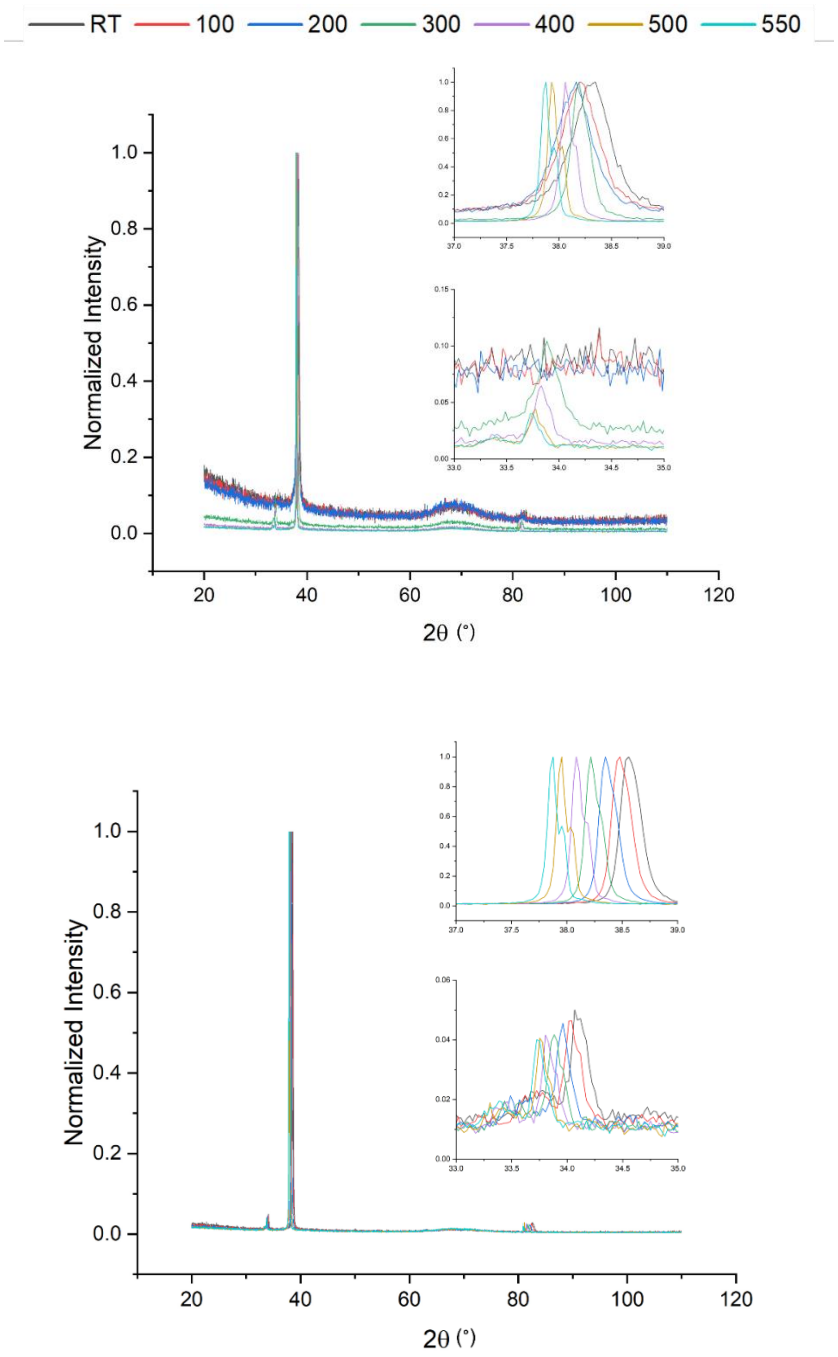

Figure 11. XRD results of the $Al_{97}Ce_3$ composition for (a) the heating cycle from room temperature to 550°C, and (b) the cooling cycle from 550°C back to room temperature. Inset are the normalized Al (111) peaks, and the $Al_{11}Ce_3$ intermetallic peaks.

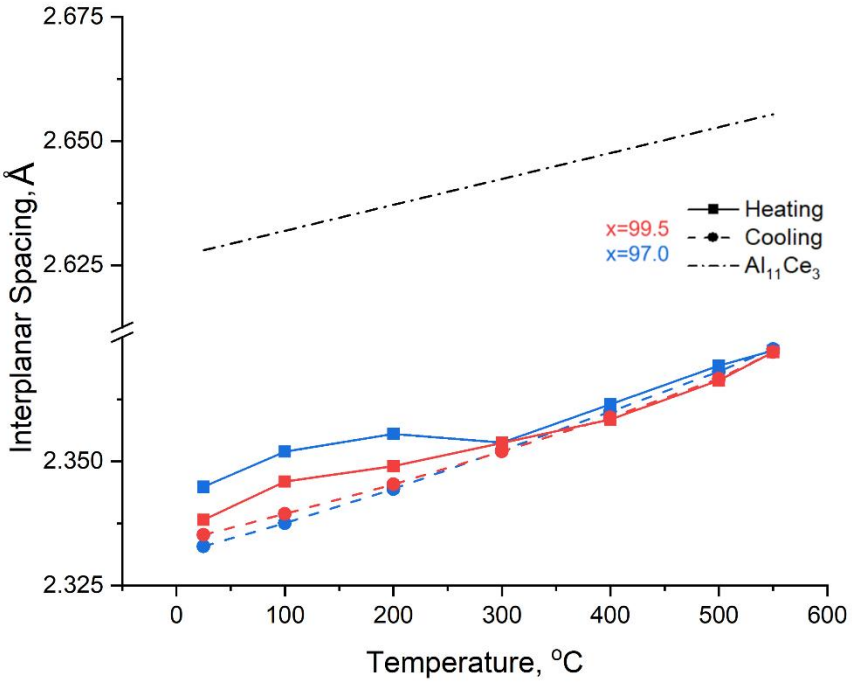

Figure 12. Measured interplanar spacing for the Al (111) peak measured during heating and cooling, and $Al_{11}Ce_3$ (123) peak upon cooling for $Al_{99.5}Ce_{0.5}$ and $Al_{97}Ce_3$.

within the system and that neither phase dominates the composite resistivity value. Comparing the as-deposited versus the annealed film, it is clear that the solid solution effects increase the resistivity more than the second phase intermetallic.

Temperature Dependent X-ray Diffraction Measurements

Figure 11 shows the overlay of the x-ray diffraction results for the $Al_{97}Ce_3$ composition (position 4) during a 11a temperature ramp and 11b cool down. Consistent with Figure 8, there are three predominant peaks. Around 34° is a low angle peak associated with the (123) $Al_{11}Ce_3$ phase. The Al (111) peak is present at ~38° as well as the Al (222) peak at ~82°. In the as-deposited state, up to 200°C, the material is in the metastable solid solution.

At the 300°C anneal step, the $Al_{11}Ce_3$ (123) starts to precipitate from the solid solution and the Al (111) and (222) reflection intensities increase. Throughout the annealing process, the peaks shift and sharpen. Inset in Figure 11a and 11b are magnified views of the Al (111) and the $Al_{11}Ce_3$ (123) normalized peaks for the heating cycle and cooling cycle, respectively. Figure 12 illustrates the resultant Al (111) interplanar spacing during the heating and cooling cycle. As is shown, during the heating cycle, the Al (111) interplanar spacing increases from room temperature to 100°C consistent with thermal expansion and from 100 to 300°C it saturates and decreases, suggesting intrinsic stress relief in the film. As noted above, at 300°C, the $Al_{11}Ce_3$ phase emerges consistent with Figure 8. From 300°C to 550°C the peaks shift consistent with thermal expansion and as shown in Figure 12 during the cooling cycle the $Al_{11}Ce_3$ (123) interplanar spacing contracts linearly with decreasing temperature. The open hysteresis observed in the heating/cooling cycle for the Al (111) is a measure of the stress relief and rejection of the Ce in the solution, which also leads to a

lattice contraction as shown in Figure 12. The total contributions can be estimated by comparing the interplanar spacing of the as-deposited film to the room temperature value after the temperature cycle. A simple calculation of the lattice expansion from a Vegard's law approximation suggests that substitutional Ce induces ~564 MPa of tensile stress to the Al lattice at this concentration. Thus, the difference in the room temperature interplanar spacing before and after the annealing cycle is due to the $Al_{11}Ce_3$ precipitation and ~ -109 MPa (compressive) stress is due to stress relief. Similarly, a Vegard's law approximation of the $Al_{99.5}Ce_{0.5}$ composition was calculated suggesting that (94 MPa) of the difference in room temperature interplanar spacing is due to the $Al_{11}Ce_3$ precipitation and ~ 76 MPa (tensile) is due to stress relief. A Vegard's law approximation could not be performed on the $Al_{92.5}Ce_{7.5}$ composition as the TDXRD experiment was run on a pre-annealed sample. The interplanar spacing values of the $Al_{11}Ce_3$ precipitation phase is also shown on Figure 12. Because all the data was consistent, only a single dashed line representing the linear regression is shown. As discussed below, we use the cooling cycle data to extract the coefficient of thermal expansion of the Al and $Al_{11}Ce_3$ phases in the thin films.

Coefficient of Thermal Expansion Determination

The coefficient of thermal expansion (CTE) can be calculated through the shifts in the XRD peaks as a function of temperature. The linear coefficient of thermal expansion can be calculated using:

$$\frac{\Delta d}{d} = \alpha \Delta T \tag{6}$$

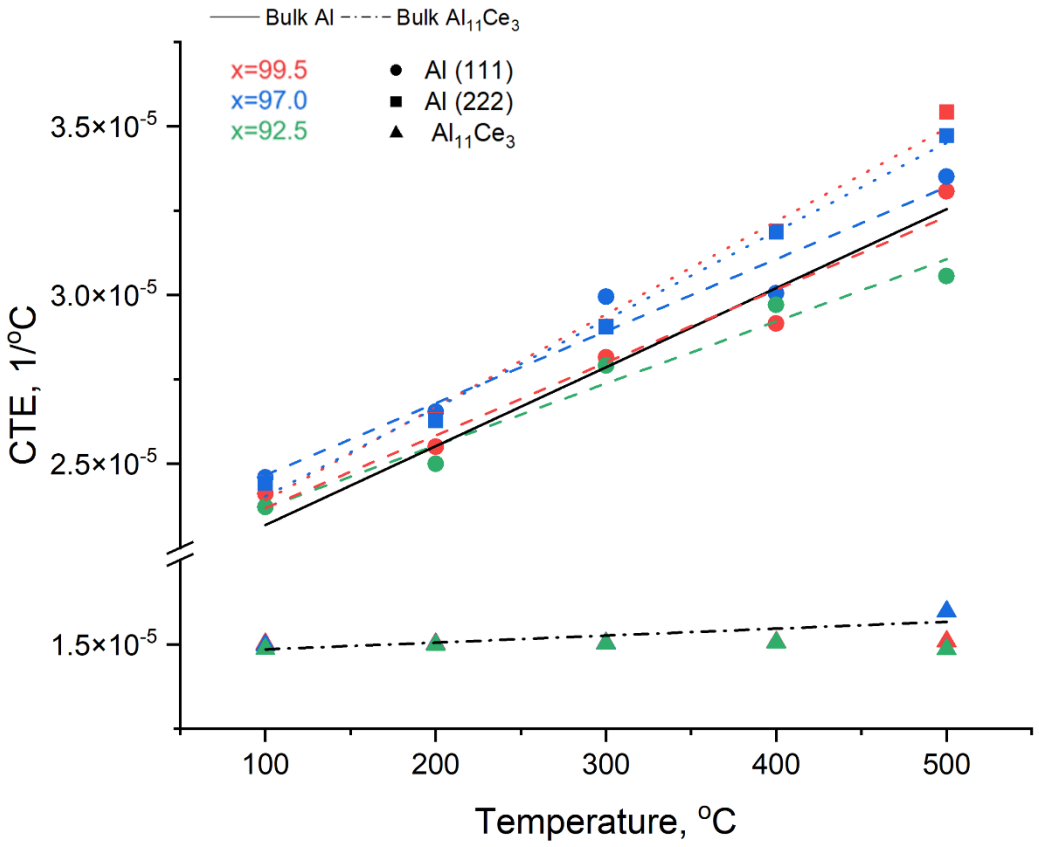

Figure 13. CTE calculated (with correction for x=92.5) from HTXRD experiments for the Al (111), Al (222), and $Al_{11}Ce_3$ (123) showing the temperature dependent CTE compared to bulk Al and $Al_{11}Ce_3$ for each composition measured

where d is the interplanar spacing determined via Braggs law, α is the CTE, and ΔT is the change in temperature. Using this equation and estimating Δd/d for each temperature increment, the temperature dependent CTE for aluminum and $Al_{11}Ce_3$ can be estimated. Because of the rigid underlying SiO_2 on Si substrate, below a critical thickness a correction can be performed to account for the in-plane biaxial compressive stress that develops due to the difference in the SiO_2 and Al CTE [61]. The correction term is given by:

$$\alpha' = \frac{\alpha_f - \alpha_{sub}}{1-\nu} \tag{7}$$

where α' is the uncorrected CTE, α_f is the CTE of the film (Al), α_{sub} is the CTE of the substrate (SiO_2), and ν is Poisson's ratio. α_{sub} (SiO_2) is taken to be $0.25*10^{-6}$/°C [47], and ν is taken to be 0.33 for Al. The cooling cycle data was used to determine the CTE values as the intrinsic stress is relieved and the equilibrium phases have formed.

Note that for the high Ce content sample (x=92.5) the measured CTE values were adjusted using equation 2. The thickness value at this point is ~375 nm as shown in figure 1d. In this thickness regime, the CTE value shows a dependence due to the rigid nature of the substrate [73]. Both the Al and $Al_{11}Ce_3$ phase exhibit this thickness dependent behavior. As shown in Figure 13, the two phases expand independently of one another at each composition. The temperature dependent CTE of the Al matrix within the thin films increases similarly to bulk Al and the values for Al found in literature [74]. However, the $Al_{11}Ce_3$ intermetallic phase has a nearly constant CTE of ~$1.5x10^{-5}$/°C within the temperature range on this study (25-550°C).

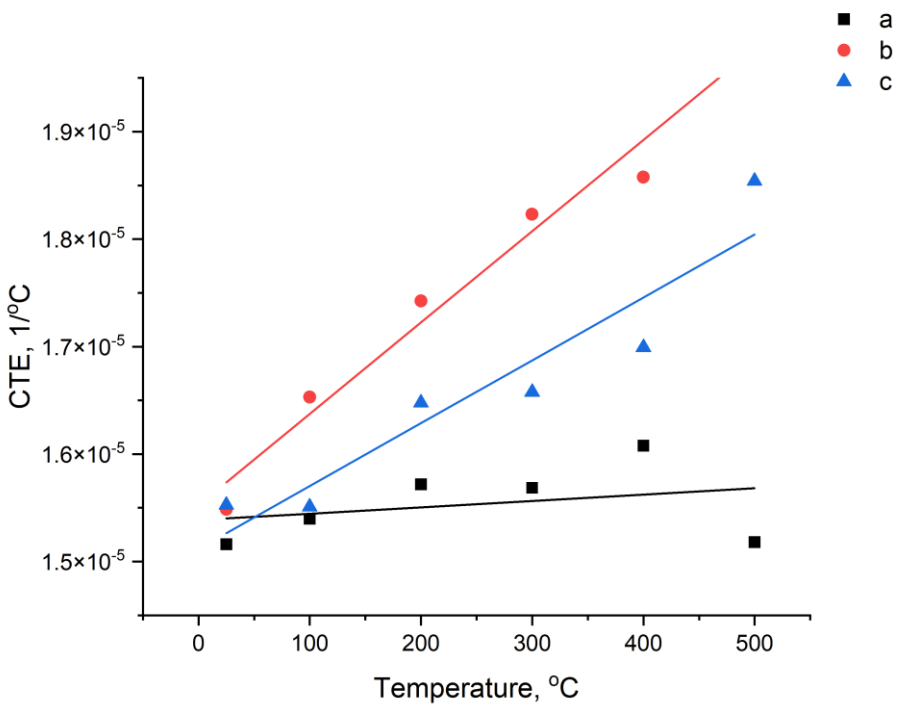

Figure 14. Directional dependent CTE from the bulk $Al_{11}Ce_3$ showing anisotropic behavior

A pure, bulk $Al_{11}Ce_3$ sample was arc melted from a mixture of stoichiometric Al ad Ce powders and the CTE measured with the same conditions as the thin films. The bulk $Al_{11}Ce_3$ (123) results are included in Figure 13 and shows a slight CTE temperature dependence in the temperature range of study varying roughly linearly from ~$1.5x10^{-5}$/°C to $1.72x10^{-5}$/°C, from room temperature to 550°C. A Rietveld analysis of the entire XRD pattern (shown in supplemental information) demonstrated a slight anisotropic behavior as shown in Figure 14. The expansion of the a lattice parameter remains roughly stable at ~$1.54x10^{-5}$/°C while the b lattice parameter expands with a slightly higher slope, and the c lattice parameter expansion shows an even higher change from ~$1.5x10^{-5}$/°C to $2.0x10^{-5}$/°C, from room temperature to 550°C. The refined lattice parameter values with respect to temperature is shown in supplement. Since the thin film sample demonstrates preferred orientation along the (123) plane, the expansion of the film is dominated by the a lattice parameter which is consistent with the nearly constant CTE in (123) reflection of the thin film. Similarly, analysis of the expansion of the bulk sample along the (040) and (006) planes are consistent with the b and c lattice parameter expansion, respectively. In addition, bulk samples with nominally 1 wt.% plus or minus the $Al_{11}Ce_3$ composition were also generated. The measured CTE values of these samples were also consistent with both the Al and $Al_{11}Ce_3$ phase in the thin films and this HTXRD data given in the supplement information.

The two phase alloy CTE was estimated using two rule of mixture models assuming uniform stress or strain. The Reuss [75] model for the effective coefficient of thermal expansion, α^*, is given by

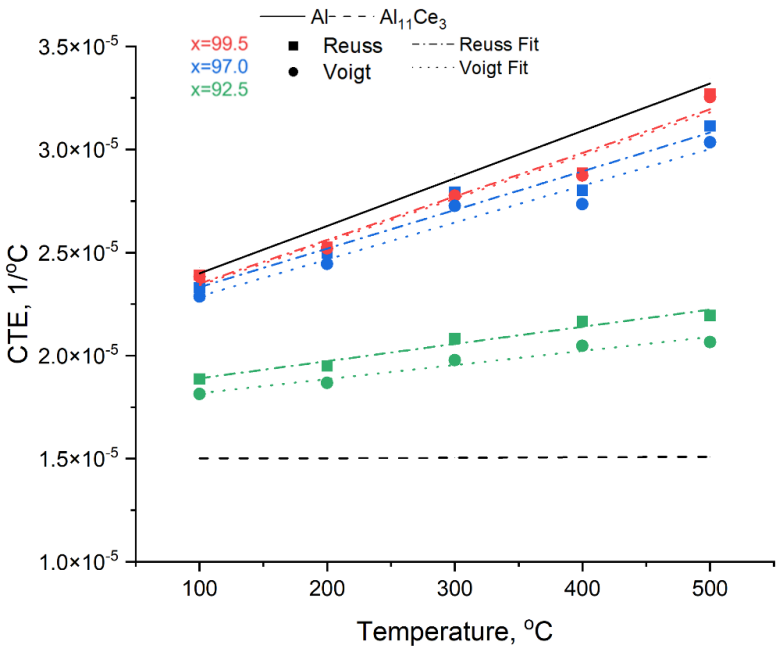

Figure 15. Two phase alloy composite CTE calculated from Voigt and Reuss approximations using average of our Al and $Al_{11}Ce_3$ data as reference

$$\alpha^* = \xi_1\alpha_1 + \xi_2\alpha_2 \quad (8)$$

where ξ_i and α_i are the phase fractions and single phase coefficient of thermal expansions, respectively. The Voigt [76] upper bound model is given by

$$\alpha^* = \frac{\xi_1 E_1 \alpha_1 + \xi_2 E_2 \alpha_2}{\xi_1 E_1 + \xi_2 E_2} \quad (9)$$

where E is the Young's Modulus for the respective phase taken to be 69 GPa for Al and a value of 97 GPa for $Al_{11}Ce_3$ was extracted from figure 4 of Sims *et. al*. Figure 15 shows the two-phase alloy CTE as a function of temperature for various Al_xCe_{100-x} compositions. The $Al_{11}Ce_3$ intermetallic CTE lowers the Al CTE and is suitable for some piston applications. Future work will be done to examine the two-phase system CTE via microfabricated cantilevers [49,77] structures and dilatometry for the thin film and bulk alloys, respectively.

Conclusion

The crystal structure and phase fraction, film morphology, electrical resistivity, and temperature-dependent coefficients of thermal expansion are all correlated to the Al_xCe_{100-x} composition. In the as-deposited state, the Al (111) peak is present. Peak broadening and shifting indicate the formation of a metastable solid solution. Upon annealing, the α-$Al_{11}Ce_3$ intermetallic phase forms and the Al (111) to α-$Al_{11}Ce_3$ (123) peak ratio decreases as expected with increasing Ce content. The film transitions from an almost pure Al matrix to pure α-$Al_{11}Ce_3$ intermetallic across the material library sputter deposited on the SiO_2-coated Si wafer. The as-deposited resistivity increases with increasing Ce content, consistent with solid solution alloying. In the annealed sample, the resistivity is lower, however the two-phase system resistivity increases with increasing Ce content due to the

reduction in the percolating network with the precipitation and increasing phase fraction of the intermetallic phase. Additionally, we investigated the temperature dependent CTE at a series of fixed alloy compositions. The two phases expanded independently of one another with the Al matrix having a temperature-dependent CTE similar to bulk Al, and the $Al_{11}Ce_3$ intermetallic phase showing a constant CTE of ~$1.5x10^{-5}$/°C in the range of study. The two-phase alloy CTE was estimated via the Reuss and Voigt models and with the $Al_{11}Ce_3$ CTE being lower than Al, it suppresses the composite CTE value bring it in line with the current premium piston alloys that are commercially available. Importantly, we have demonstrated the efficacy of the thin film technique, which is consistent with the bulk alloy, thus we can explore more complex multi-component alloys via the thin film combinatorial synthesis and XRD analysis technique for rapid discovery of new lower CTE materials.

Acknowledgements

This research was sponsored by the Critical Materials Institute, an Energy Innovation Hub funded by the U.S. Department of Energy (DOE), Office of Energy Efficiency and Renewable Energy, Advanced Manufacturing Office, and Eck Industries. This work was performed under the auspices of the U.S. DOE.

CHAPTER II

IDENTIFICATION OF LOW THERMAL OF EXPANSION IN $AL_{23}CE_4NI_6$ VIA COMBINATORIAL SPUTTERING OF AL-CE-NI-MN THIN FILMS AND UPSCALING TO BULK MATERIALS

Identification of low coefficient of thermal expansion in $Al_{23}Ce_4Ni_6$ via combinatorial sputtering of Al-Ce-Ni-Mn thin films and upscaling to bulk materials

Reece Emery[1], Orlando R. Rios[1], Eric A. Lass[1], Cameron S. Jorgensen[1], Dustin A. Gilbert[1], William R. Meier[1], Michael R. Koehler[2], Philip D. Rack[1,3,*]

1. Department of Materials Science and Engineering, University of Tennessee, Knoxville, Tennessee 37996, USA
2. UT Institute for Advanced Materials and Manufacturing, Knoxville, Tennessee 37996, USA
3. University of Tennessee – Oak Ridge Innovation Institute, Knoxville, Tennessee 37996, USA

*corresponding author: prack@utk.edu

Keywords: combinatorial sputtering, thin films, rare earth alloys and compounds, thermal expansion, x-ray diffraction, neutron diffraction

Author Contributions

This work was originally published in the Journal of Alloys and Compounds. The author of this dissertation was the lead writer and experimentalist for this paper. Synthesis of the film via combinatorial sputtering was conducted by him. The author is responsible for all scanning electron microscopy (SEM), x-ray diffraction (XRD), and 4-point probe resistivity measurements were performed by him. Collaborator Michael Thompson fabricated the bulk samples used in this study. Collaborator William Meier synthesized all single crystal material used in this study. Dustin Gilbert and Cameron Jorgensen are

responsible for all magnetometry and electrical resistance measurements while Eric Lass performed the ThermoCalc modeling. The author performed all data analysis, interpretation, writing, and figure generation for the results included in this paper.

Abstract

$Al_{100-x-y-z}Ce_xNi_yMn_z$ thin films were synthesized via combinatorial sputtering from Al, $Al_{80}Ce_{20}$, $Al_{91}Ni_9$, and $Al_{93}Mn_7$ targets. The resultant as-deposited films exhibit a continuous composition gradient of the various constituents and form a metastable solid-solution over most of the composition space. Subsequent annealing leads to the formation of the thermodynamically stable systems of Al, and α-$Al_{11}Ce_3$, Al_8CeMn_4, and $Al_{23}Ce_4Ni_6$ intermetallics -- where the phases present and fraction depend on the composition. Temperature dependent x-ray diffraction (TDXRD) was used to determine the coefficients of thermal expansion (CTE) for each phase. The thin film Al and $Al_{11}Ce_3$ temperature dependent CTE values are consistent with previously reported results. The thin film Al_8CeMn_4 phase reveals a slight decrease in the CTE with a range from 27×10^{-6} $^oC^{-1}$ to 23×10^{-6} $^oC^{-1}$ in the temperature range 25-550 ^oC. The thin film $Al_{23}Ce_4Ni_6$ phase exhibits a CTE value of $\approx9\times10^{-6}$ $^oC^{-1}$ near room temperature and increases to 14×10^{-6} $^oC^{-1}$ at 550 ^oC. To confirm the thin film results, bulk stoichiometric Al_8CeMn_4 and $Al_{23}Ce_4Ni_6$ samples were prepared and measured under similar conditions. The Al_8CeMn_4 bulk sample confirmed the negative CTE trend observed in the thin film sample. Compared to its thin-film counterpart, the $Al_{23}Ce_4Ni_6$ bulk sample similarly demonstrated a low CTE value near room temperature of 5×10^{-6} $^oC^{-1}$ and an anomalous minimum in the CTE at ≈75 ^oC, which was confirmed via temperature dependent neutron diffraction. Temperature dependent

magnetic and electrical measurements were subsequently taken on $Al_{23}Ce_4Ni_6$, and the anomalous minimum in the CTE coincided with an electronic phase transition.

Introduction

Traditional aluminum alloys, such as those found in the Al-Si system, have been of interest in the automotive and aerospace industries where factors such as weight, high-temperature performance, and cost play important roles in meeting industry needs. While other material classes such as composites have started to be used in these industries, a variety of factors (e.g., demonstrated performance, established manufacturing and fabrication facilities/expertise, and design history) keep aluminum alloys at the forefront in these spaces [78]. Thermal stability (as both phase and dimensional stability) has been a major drawback with traditional aluminum systems, where improvement in this area would greatly increase the role of aluminum-based alloys in many structural applications [78–80]. Likewise, increased thermal stability would enable higher engine power throughput, a key factor in improving fuel efficiency among other performance metrics [81].

Aluminum alloyed with cerium in the range of 1.0-3.5 at.% (6-16 wt.%) has been shown to maintain the weight and cost-savings of traditional aluminum alloys while also providing the needed high-temperature stability due to the formation of intermetallic phases [55–57]. Similarly, it has been shown that cerium-based aluminum alloys significantly improve the high temperature mechanical properties and castability [53,54]. Moreover, it has been demonstrated that adding small amounts of Ce to existing commercial alloys, such as B319, can further increase hardness, strength, and elongation at failure [82]. Ce as an alloying

agent is distinguished from other rare earth elements (REE) by its low relative cost and extremely competitive supply-to-demand ratio. This can be attributed to Ce being mined as an unavoidable byproduct of other rare-earth element mining operations [83]. In 2020, the cost for cerium oxide was $2/kg compared to $50/kg for neodymium oxide and $3800/kg for scandium oxide [84,85]. Furthermore, it has been shown that castable, REE rich aluminum alloys can be produced through direct reduction of REE oxides [86]. Additionally, the price of Si, which has been traditionally used for high temperature Al applications due to its low CTE and formation as primary silicon in the alloy, has risen nearly 300% over the last couple of years to $8/kg [87,88]. The Al-Ce system also demonstrates interesting corrosion behavior where the system creates a Ce-rich outer passivation layer, which limits the oxidation of the Al matrix [60]. As such, surface engineering and coatings utilizing Al-Ce have been explored for corrosion protection [58,59,89].

In the binary Al-Ce system, Al takes on the standard form of a face-centered cubic (FCC) structure with a lattice parameter of 4.04 Å [61]. Cerium crystallizes in two forms at ambient temperature and pressure; one is an FCC structure with a lattice parameter of 5.14 Å, and the other is a hexagonal close-packed (HCP) structure with a=3.65 Å, and c=5.91 Å [62]. This leads to limited solubility in the binary Al-Ce alloy system and the formation of several intermetallic phases. In the composition region of interest (<10 at.% Ce), the binary Al-Ce alloy system forms a two-phase region with a nearly pure Al matrix and the α-$Al_{11}Ce_3$ intermetallic. The α-$Al_{11}Ce_3$ intermetallic forms an orthorhombic structure with a=4.39 Å, b=10.08 Å, and c=13.02 Å [63].

While binary Al-Ce alloys demonstrate interesting behavior, further alloying additions can be used to further refine both mechanical and thermal properties to meet process requirements for mechanical alloys. Manganese has been used as an alloying element in aluminum alloys as Al-Mn alloys have a combination of good mechanical properties, corrosion resistance, and welding/brazing ability [90]. Additionally, Mn acts as a BCC stabilizer in Al-Cu alloys as well as widens the single-phase region to lower temperature and lower A1 content [91]. Mn takes on a unique crystal structure at room temperature known as α-Mn, which is a complex BCC structure with a lattice parameter of 8.903 Å [92]. This structure contains 58 atoms and is the only element to take on this structure at room temperature. Thus, like Ce, Mn and Al have limited mutual solubility and readily form several intermetallics [93,94]. The addition of Ce to the Al-Mn system further expands its complexity and the possible intermetallic phases formed. These intermetallic phases include: $Al_{20}Mn_2Ce$, $Al_{10}Mn_2Ce$, Al_6Mn, and Al_8Mn_4Ce. Al_8Mn_4Ce has a tetragonal crystal structure with a=8.89 Å, b=8.89 Å, c=5.17 Å [95,96]. It has been demonstrated that the Al-Ce-Mn system is extremely versatile in tuning material properties. Yield strength, hardness, and ductility can be optimized by adjusting the relative composition of the alloy to meet various application requirements [97–99].

Nickel has also been investigated as a possible alternative to Al-Si alloys for high temperature applications. The primary driving force to finding an alternative to the Al-Si system is its low eutectic temperature [100]. Thus, its maximum operating temperature is limited to 250 ^{o}C. The Al-Ni system has a eutectic point about 60 ^{o}C higher than Al-Si at a eutectic composition of 3.1 at.% Ni [101,102]. Furthermore, Al-Ni exhibits good

corrosion resistance, fluidity, chemical stability, thermal properties, and a low tendency to hot tear [101–104]. The Al-Ni system also has limited solubility and readily forms intermetallics, with the primary phase in Al-rich alloys being Al_3Ni [105,106]. The primary drawback of the Al-Ni alloys is the mechanical properties, with the resulting eutectic being relatively weak due to the limited solubility between the phases [102]. The introduction of Ce and Mn as additional alloying elements could enhance the mechanical properties while maintaining the desirable thermal and chemical stability of the Al-Ni binary system, as has been seen with the addition of Sc [107].

Only a handful of investigations of the ternary Al-Ce-Ni system have been reported, and the stability of the ternary $Al_{23}Ce_4Ni_6$ compound is still in question. Zarechnyuk et al. [108] and Ferro et al. [109] were the first to report on phase equilibrium in Al-Ce-Ni, and neither reported the existence of $Al_{23}Ce_4Ni_6$. Belov et al. also made no mention of the $Al_{23}Ce_4Ni_6$ phase, although their work was focused on casting and solidification behavior [110,111]. Gout et al. first reported the $Al_{23}Ce_4Ni_6$ phase, synthesizing it from a stoichiometric blend of elemental powders sintered at 800 °C [112]. Tang et al. later reported $Al_{23}Ce_4Ni_6$ in the ternary phase diagram at both 500 °C and 800 °C [113,114]. However, in their later thermodynamic assessment of the system [115], the phase was modeled as stable only between 700 °C and 1000 °C for Al-rich alloys. More recently, Wu et al. [116] investigated the microstructure and creep behavior of cast Al-Ce-Ni alloys near the ternary eutectic $L \rightarrow FCC + Al_{11}Ce_3 + Al_3Ni$ (about Al-2Ce-2.5Ni) but reported no evidence of $Al_{23}Ce_4Ni_6$ in either the as-cast state or after annealing at 590 °C for 24 h. In the Al-Ce-Ni ternary system, several intermetallics form, including Al_4CeNi, Al_5CeNi_2, and $Al_{23}Ce_4Ni_6$. $Al_{23}Ce_4Ni_6$

takes on a monoclinic structure with a=16.042 Å, b=4.140 Å, c=18.380 Å, and β=113.24° [112]. Additionally, this phase has shown heavy fermion behavior [112,117]. Mn in the Al-Ni system has been shown to increase the yield strength from the binary alloys, which can be further fine-tuned through solidification rate or heat treatment through precipitation strengthening [118]. Previous work in the Al-Ce-Ni-Mn quaternary system has shown that this system has excellent creep resistance and exhibits a significant increase in the modulus of elasticity at elevated temperatures, making this system an ideal candidate for high temperature Al applications [119,120].

The coefficient of thermal expansion (CTE) is a material property that is defined by a material's dimensional response to a change in temperature. This phenomenon is critical to processes at elevated temperatures as the change in dimension respective to temperature affects operational tolerances and can lead to failure if excessive [11,12]. Additionally, for parts that have cyclic temperatures, the induced thermal stresses can cause thermal fatigue that can lead to the formation of defects and ultimately failure [13].

The linear coefficient of thermal expansion, α, is defined as:

$$\alpha = \frac{1}{L_0}\frac{dL}{dT} \tag{10}$$

where L_0 is the original dimensional length at the nominal temperature T_0, and dL is the instantaneous change in the dimensional length after expansion by changing the temperature of the system to some temperature T. Conventional dilatometry will directly measure this change is dimensional length with temperature for the net alloy. Due to the size limitations of a thin film, conventional dilatometry and optical techniques cannot be

applied. One common alternative technique is temperature-dependent x-ray diffraction (TDXRD). In this technique, the CTE of individual phases is determined through changes in the interplanar spacing with respect to corresponding changes in temperature [64]. However, this technique does not directly measure the net CTE of the alloy, as is done with conventional dilatometry, but rather that of the individual phases. Instead, an estimation using phase fractions must be calculated.

Equation 1 can be modified such that the CTE can be calculated through the shifts in the XRD peaks as a function of temperature. The linear coefficient of thermal expansion can be calculated by:

$$\frac{\Delta d}{d} = \alpha \Delta T \tag{6}$$

where d is the interplanar spacing determined via Braggs law, α is the CTE, and ΔT is the change in temperature. Using this equation and estimating Δd/d for each temperature increment, the temperature dependent CTEs of the phases of interest can be estimated. Corrections should be made for films below a critical thickness of ≈300 nm on SiO_2/Si substrates to account for the in-plane biaxial compressive stress that develops due to the difference in the substrate and Al CTEs [47,61]. Such corrections were unnecessary in this study as the films were above the critical thickness and cooling cycle data were used. The thin film correction versus film thickness was explored previously in the Al-Ce materials system. Further, the effect of annealing and phase evolution on stress relief was also previously investigated in the Al-Ce binary system via tracking lattice parameters from the

as-deposited state through the annealing cycle of the Al phase [121]. Should the film be below the critical thickness, the correction term is given by:

$$\alpha' = \frac{\alpha_f - \alpha_{sub}}{1-\nu} \quad (7)$$

where α' is the uncorrected CTE, α_f is the corrected CTE of the film , α_{sub} is the CTE of the substrate (SiO_2), and ν is Poisson's ratio. α_{sub} (SiO_2) is taken to be $0.25*10^{-6}$/°C [47], and ν is taken to be 0.33 for Al.

Film thickness, substrate material, near surface effects, and crystallite size have all been shown to influence CTE values in the as-deposited state (typically overestimating CTE values); however it has been shown previously that thin film CTE values are consistent with bulk values once annealed to allow for the relief of stress in the film generated during deposition [46,47,73,122].Additionally, various phases can be measured independently and simultaneously [45]. Recent work exploring temperature dependent XRD on thin films and bulk samples revealed that the CTE of the $Al_{11}Ce_3$ intermetallic is anisotropic but has an average room temperature value of $\approx 15\times10^{-6}$ °C^{-1} (15 ppm/°C), which was also confirmed via dilatometry using bulk samples [121,123]. Moreover, CTE anisotropy has been explored by comparing various reflections in non-cubic systems [48,65].

In this study, we utilize a combinatorial thin film sputtering approach to explore the Al-Ce-Ni-Mn system for the rapid discovery of low CTE phases that can be leveraged in Al-based alloys at operating temperatures similar to or exceeding traditionally used Al-Si alloys (limited to <250 °C). Co-sputtering is able to achieve thin film compositions that cover a large composition range while allowing for the realization of metastable material

configurations; for example, supersaturated solid solutions commonly result in various as-deposited sputtered alloys due to the high energy deposition process and fast cooling rates [5,6,10]. Subsequent annealing of the film can lead to equilibrium states of the system through phase separation, recrystallization, and grain growth though metastable phases may still be present [8,66]. We apply the thin film rapid materials discovery approach to the $Al_{100-x-y-z}Ce_xNi_yMn_z$ system as a cursory technique to identify candidate phases and compositions for various lightweight and high-temperature alloy applications. As the CTE is a critical property to various high-temperature applications, we use the thin film approach to rapidly explore a large composition space to elucidate interesting CTE values and trends of the various intermetallic phases that form to determine their suitability for high temperature cyclic processes. Thus, a combinatorial library of $Al_{100-x-y-z}Ce_xNi_yMn_z$ alloys is co-sputter deposited with the crystal structure, film morphology, and temperature-dependent coefficients of thermal expansion all being correlated to the $Al_{100-x-y-z}Ce_xNi_yMn_z$ composition. These material properties identified in the films are used as a semi-quantitative guideline. Identified compositions of interest are then upscaled into bulk cast alloys for further, more extensive investigation in the desired application space.

Materials and methods

Sputtering conditions

$Al_{100-x-y-z}Ce_xNi_yMn_z$ alloys were co-sputtered from pure Al, $Al_{80}Ce_{20}$ (80-20 at.%), $Al_{91}Ni_9$, and $Al_{93}Mn_7$ targets to form a combinatorial library across a SiO_2-coated (500 nm) Si substrate (500 µm). The substrate was fixed and not rotated to generate the desired

composition gradient. An original base pressure of ≈3×10^{-7} Torr was achieved in the system. The Al target was powered by a 100 W DC source while the $Al_{80}Ce_{20}$, $Al_{91}Ni_9$, and $Al_{93}Mn_7$ targets were each powered by 200 W RF supplies in a 5 mTorr Ar ambient atmosphere for 2 hours such that a near uniform thickness profile of approximately 1 µm is obtained.

A second $Al_{100-x-y}Ce_xNi_y$ ternary sample was sputtered to explore the influence of Mn on the alloy system. As previously described, the Al target was powered by a 100 W DC source while the $Al_{80}Ce_{20}$ and $Al_{91}Ni_9$ targets were powered by 200 W RF supplies in a 5 mTorr Ar ambient atmosphere for 2 hours to again obtain a near uniform thickness profile of ≈1 µm.

Single crystal growth

Elemental Al, Ni and Ce were loaded into a 2 mL alumina Canfield crucible set and then encapsulated in a silica ampoule [124]. This assembly was placed in a furnace, heated to 1100 °C over 6 h, held for 12 h, and then cooled to 800 °C over 100 h to precipitate the crystals. The ampoule was subsequently removed from the furnace and centrifuged to decant away the Al-rich melt from the crystals. This procedure yielded 0.03-1 mm wide needle-like metallic crystals of $Al_{23}Ce_4Ni_6$ up to 9 mm long.

Bulk sample preparation

Pure, bulk Al_8CeMn_4 and $Al_{23}Ce_4Ni_6$ samples were arc melted from a mixture of stoichiometric Al, Ce, Mn, and Ni constituents. Additionally, single crystal samples of the $Al_{23}Ce_4Ni_6$ intermetallic were grown using a flux growth methodology as described in

2.2. Both the cast and single crystal samples were ground into powders using a mortar and pestle for TDXRD measurements to complement the thin film experiments. These samples were ground from the as-cast state. Alloy samples were also arc melted based on compositions of interest in the film from a mixture of the elemental constituents. Alloy samples were cut and polished for XRD measurements.

Thin film annealing conditions

Annealing of the thin film sample was conducted in vacuum with a base pressure of 3×10^{-7} Torr. The sample was radiant heated with halogen lamps from the base temperature (≈15 °C) to 525 °C at a rate of approximately 10 °C/min (≈1 hour in total), held at 525 °C for 10 minutes, and then reduced to 475 °C and 450 °C and held for 10 minutes at each temperature. The sample was cooled at an approximate rate of 10 °C/min from 450 °C to 200 °C. Because the natural cooling rate was slower than 10 ^{o}C/min below 200 ^{o}C, the heater was turned off, and the sample was left to cool to room temperature overnight.

X-ray conditions

Room temperature x-ray diffraction (XRD) patterns were measured using a Malvern Panalytical X'Pert^3 MRD diffractometer, and TDXRD experiments were performed using a Malvern Panalytical Empyrean diffractometer. A 2θ-ω scan with an ω offset of 3° and Cu Kα radiation (λ=0.154 nm) was used for both room temperature and TDXRD experiments. Room temperature XRD experiments on as-deposited and annealed samples were performed from 25° to 60° 2θ with a step size of 0.05° (the total time of each scan was 30 min). To estimate the coefficient of thermal expansion, temperature dependent x-

ray diffraction experiments were performed from 20° to 60° 2θ using a 0.39° step size (the total time of each scan was 30 min). The sample was heated *in situ* from 25 °C to 550 °C in a nitrogen atmosphere with a heating rate of 5 °C/min. Data was collected at 100, 200, 300, 400, 500, and 550 °C after a five-minute hold at each temperature to allow the sample to reach thermal equilibrium. The same conditions were used during the cooling cycle. In total, thirteen measurements were taken for each complete temperature cycle. Additional TDXRD experiments of a cast bulk sample and ground single crystal were performed using a heating rate of 5 °C/min and data collection temperatures of 25, 50, 75, 100, 125, 150, 175, 200, 300, 400, 500, and 550 °C upon both heating and cooling with a 30 minute hold half way through at 550 °C. Cryo-XRD experiments were performed using a Panalytical X'pert Pro MPD with an Oxford PheniX closed-cycle cryostat. Measurements were taken at -250, -225, -200, -175, -125, -785, -50, -15, -5, 10, 15, 25, and 35 °C. The compositions of the phases were assumed to be constant and stoichiometric throughout the heating and cooling cycles. Temperature was measured in the heated stage via a thermocouple. A series of calibration tests were performed before starting TDXRD on samples. Alumina was used as a calibration sample and compared to literature, which can be found in the supplemental information [125–127]. Additionally, successive x-ray experiments were performed at single temperature steps on films to ensure it had equilibrated. Finally, the CTE of the Al phase in each was used as a baseline for analysis.

Scanning Electron Microscopy and Energy dispersive X-ray spectroscopy

Energy dispersive x-ray spectroscopy (EDXS) and scanning electron microscopy (SEM) were conducted on a Carl Zeiss MERLIN SEM. The combinatorially sputtered $Al_{100-x-y-}$

$_zCe_xNi_yMn_z$ (as-deposited and annealed) was measured at 17 equally spaced increments along the full profile of the composition gradients. An accelerating voltage of 10 keV was used for EDXS.

NOMAD experiment

A flux grown bulk single crystal sample of $Al_{23}Ce_4Ni_6$ was ground into a powder and loaded into quartz glass capillaries with 2.8 mm inner and 3 mm outer diameter. The samples were aligned by translating them through the beam while monitoring the scattered intensity. The sample was heated from -135 to 225 ^oC by immersion into an Ar gas stream. Neutron diffraction data were collected at 15 temperatures for an accelerator proton charge of 8 C, corresponding to about 20 minutes of data collection at 1.4 MW accelerator power for each temperature step. Individual measurements were performed using first an empty capillary and then an empty diffractometer. Scattering from a Vanadium rod was used for normalization, and scattering from diamond powder was used for calibration. Refinements and analysis were completed in GSAS-II.

Vibrating sample magnetometry

Magnetometry measurements were performed using a Quantum Design Dynacool Physical Properties Measurement System (PPMS). Ground single crystal powder was loaded into a plastic sample holder that was supported by a brass sample rod. Magnetization versus temperature measurements were performed between 300 K and 400 K in a static field of 100 mT and 2 T. An averaging time of 12 seconds per datapoint was used with a temperature ramp rate of 4 K/min.

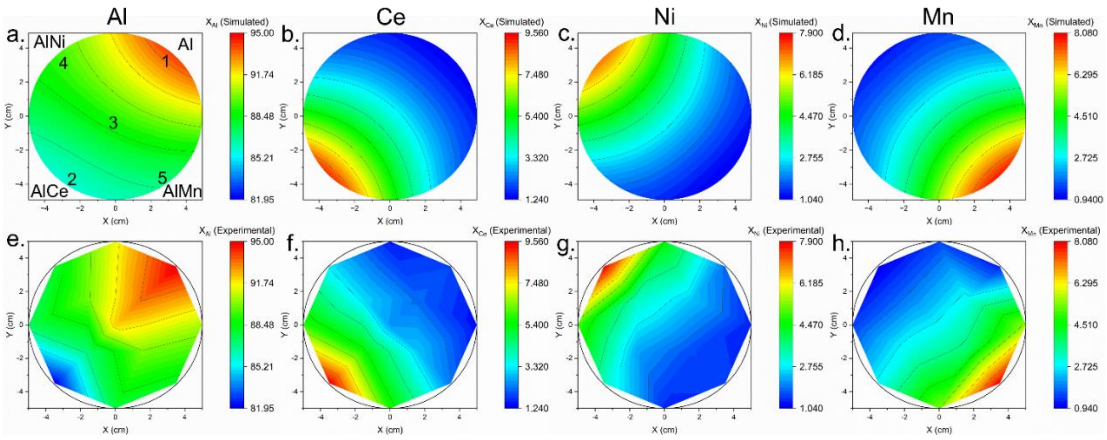

Figure 16. Simulated (a, b, c, d) and experimentally determined (e, f, g, h) composition gradient profiles for Al (a,e), Ce (b,f), Ni (c,g), and Mn (d,h) on the 100 mm diameter combinatorial wafer. Note the approximate target locations relative to the substrate in a. The primary composition (EDS) and XRD positions are denoted as 1-5.

Electric resistance measurements

Temperature-dependent resistance measurements were also performed in the Quantum Design Dynacool PPMS on the powder ground from the single crystal. The measurement apparatus consisted of a pair of copper plungers pressing the powder within an alumina tube. Resistance was measured using a 4-point configuration between the two copper plungers. Control measurements performed without a sample show a contact resistance of <0.01 Ohm, while the measured powder has a resistance of >1 kOhm using a 500 μA excitation. Measurements were performed between 300 K and 400 K in zero magnetic field.

Results and Discussion

Full wafer characterization

Figure 16 illustrates the composition profiles for Al, Ce, Ni, and Mn on the 100 mm diameter combinatorial wafer. The system was oriented such that primary gradients are Al to Ce and Ni to Mn. Figure 16 (a-d) show simulated composition profiles. For the simulated composition profiles, the four sputtering guns were modeled as individual Knudson surface sources, where the parameters specific to our system have been previously determined [4,6,9]. To account for the multi-element targets used in this investigation, duplicate Knudson surface sources were overlayed and effectively modeled as two sources at each gun location to account for multiple species being sputtered. The flux from these targets were divided between the two sources according to the atomic ratios within the alloy target and their relative sputter rates. Figure 16e-h show the experimentally determined composition profiles. Compositions were measured at 17 points across the wafer using

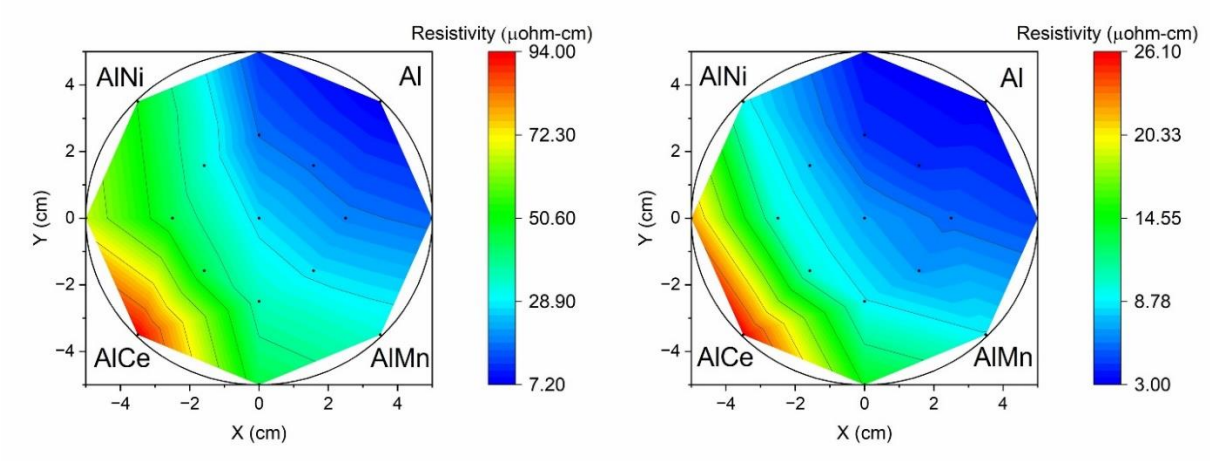

Figure 17. Resistivity maps for as-deposited (left) and annealed (right) films which correlate the measured resistivity to the sample position and, through Figure 1, the film composition.

Table 1. Location and compositions of the five prominent positions on the wafer

Location	Position	Al (at.%)	Ce (at.%)	Ni (at.%)	Mn (at.%)
Al Edge	1	95.00	1.92	1.76	1.32
Ce Edge	2	82.97	10.06	3.73	3.24
Centrepoint	3	92.15	2.60	2.43	2.82
Ni Edge	4	88.00	2.98	8.07	0.95
Mn Edge	5	88.11	2.53	1.28	8.08

EDXS (see sample spectra in supplemental information 2). Good agreement between the simulated and experimental composition and thickness profiles has been shown previously [5,6,10] and is observed by comparing the simulated and experimentally determined composition profiles presented in Figure 16. The Al composition varies from 80 to 95 at.%, Ce from 1 to 10 at.%, and both Mn and Ni from 1 to 8 at.%. The center composition was tuned such that Ce, Ni, and Mn are close to equiatomic (~2.6 at.%) with the balance being Al (92.2 at.%). A list of the primary compositions of interest are listed in Table 1.

Additionally, 4-point probe resistivity measurements were performed using a Lucas Labs Pro4-440N QuadPro Resistivity System with a Keithley 2400 Source Measurement Unit. Resistivity measurements were performed on both the as-deposited and annealed films. A map of the resistivity values with relation to the position on the wafer and target positions can be seen in Figure 17. The pure Al resistivity value for the annealed film is similar to the value of pure Al (2.65 μohm-cm) found in literature [71]. However, in the as-deposited state, this value is approximately 2.5 times larger due to the nature of the deposition process and solid solution effects. The composition range (>80% Al) maintains a percolating network regime based on previous work [121]. The increase in resistivity of the annealed film at lower Al content is therefore attributed to the formation of less conductive intermetallic phases. To examine the crystal structure of the as-deposited $Al_{100-x-y-z}Ce_xNi_yMn_z$ thin film, XRD was conducted at five positions: the center point and the same positions near each sputtering source as the EDXS (positions 1-5 in Figure 1a.), as shown in Figure 18(a-e). The Al (111) reflection dominates in the as-deposited state. Note that the (111) orientation

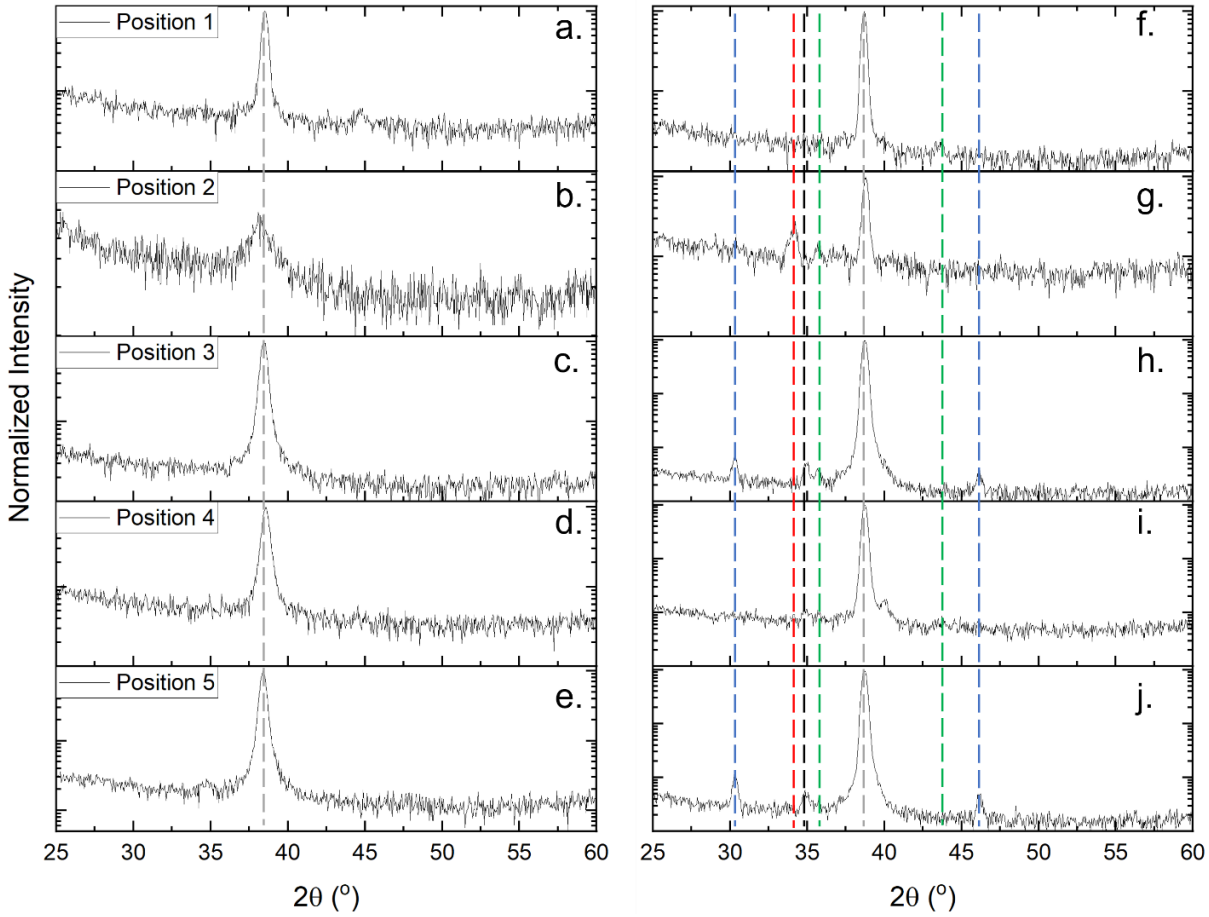

Figure 18. Comparison of as-deposited (a-e) and annealed (f-j) XRD patterns at five locations/compositions of the $Al_{100-x-y-z}Ce_xNi_yMn_z$ alloy (see locations of the measured regions in Figure 1). Gray lines indicate peaks associated with the Al phase, red to the $Al_{11}Ce_3$ phase, blue to the $Al_{23}Ce_4Ni_6$ ternary, green to the Al_8CeMn_4 ternary, and black to quaternary phase.

in FCC crystals has preferred orientation due to the low surface energy [69]. Broadening in this primary peak and shifts in position to lower 2θ suggest the formation of a metastable solid solution in the as-deposited film, which is especially evident in the Ce-rich region (X_{Ce} = ≈10 at.%), which is consistent to what was observed in binary Al-Ce sputtered films [121]. Note that the x-ray intensity drops (as evidenced by the low signal-to-noise ratio) in the Ce-rich region, which is due to the larger size difference between Al and Ce. XRD was measured at 17 locations in the annealed sample; however, 5 locations are shown in Figure 18(f-j) shows the same positions measured in the as-deposited sample. A variety of new peaks emerge at various locations in the annealed sample. Additionally, as expected, the aluminum peak intensity increases, narrows, and shifts to its expected position (higher 2θ) consistent with rejection of Ce, Ni, and Mn in the Al phase. The binary $Al_{11}Ce_3$ phase is evidenced by the (123) peak at 34°. The peaks that emerged at ≈30° and 46° 2θ are attributed to the $Al_{23}Ce_4Ni_6$ phase, while those at ≈36° and 40° 2θ are attributed to the Al_8CeMn_4 phase. The peak present at 35° 2θ is attributed to a quaternary phase that is isomorphic to the cubic (a=8.38 Å) $Al_{7.92}CeCu_{2.64}Mn_{0.44}$ phase [108] and will be discussed in detail in a future study.

Coefficient of thermal expansion determination

Figure 19 shows a sample XRD pattern collected at 550 °C during TDXRD on the film at the center point, which has a composition of $Al_{92.15}Ce_{2.60}Ni_{2.43}Mn_{2.82}$. Consistent with Figure 18, there are peaks corresponding to four phases: Al, $Al_{11}Ce_3$, $Al_{23}Ce_4Ni_6$, and Al_8CeMn_4, with the predominant peak being the Al (111) reflection. Inset in Figure 19 are the overlaid patterns collected during the TDXRD experiment for the Al (111), $Al_{11}Ce_3$

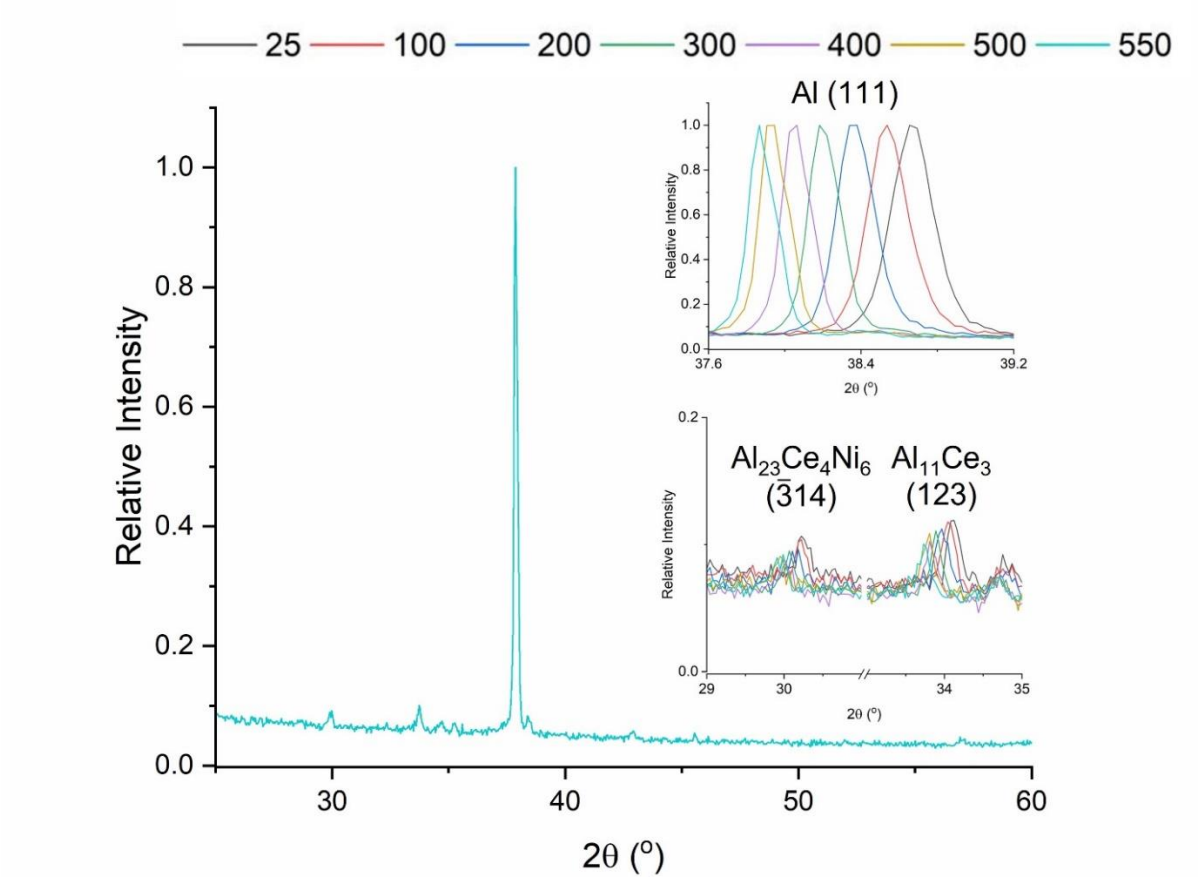

Figure 19. Center thin film sample pattern (position 3) taken during TDXRD (shown is 550 °C) with insets showing representative peak shifts for the Al (111), Al11Ce3 (123), and Al23Ce4Ni6 ($\bar{3}14$) peaks.

(123), and $Al_{23}Ce_4Ni_6$ ($\bar{3}14$) peaks. Al and $Al_{11}Ce_3$ CTE values were used as a baseline in the analysis as previous work showed good agreement between bulk and thin film CTE values for these phases [74,128,121]. Figure 20 summarizes the CTE data of the Al, $Al_{11}Ce_3$, Al_8CeMn_4, and $Al_{23}Ce_4Ni_6$ phases that are present in the center composition of the film. Conveniently, the values for Al and $Al_{11}Ce_3$ from this film were consistent with previously reported values, and a best fit line was applied to the data. Thus, residual stress or Poisson effects in thin films appear to be negligible. Both ternary phases demonstrated interesting CTE behavior. The Al_8CeMn_4 phase exhibited a CTE similar in magnitude to pure Al at low temperatures. However, the CTE decreased with increasing temperature, going from 27.5×10^{-6} $^oC^{-1}$ measured at an average temperature of 50 ^oC to 21.5×10^{-6} $^oC^{-1}$ at 500 ^oC. The $Al_{23}Ce_4Ni_6$ was determined to have a low CTE, ranging from 9×10^{-6} $^oC^{-1}$ to 14×10^{-6} $^oC^{-1}$ measured at an average temperature of 50 ^oC to 500 ^oC, respectively. For comparison, the $Al_{11}Ce_3$ intermetallic has a nearly constant value of $\approx15\times10^{-6}$ $^oC^{-1}$ over the same temperature range. Error was calculated from deviation in the peak fitting for the Al_8CeMn_4 and $Al_{23}Ce_4Ni_6$ phases due to the ratio of signal-to-noise. This suggests that $Al_{23}Ce_4Ni_6$ is an intriguing candidate for low CTE Al-based alloys. While Al_8CeMn_4 is not a suitable phase for these applications due to its higher CTE value, it demonstrates an interesting negative temperature dependent CTE behavior.

Once phases with interesting CTE trends were determined via the thin film approach, bulk samples were prepared to further investigate, confirm, and determine more quantitative results. A bulk stoichiometric $Al_{23}Ce_4Ni_6$ sample was cast, and a bulk single crystal was grown (XRD patterns and Rietveld analysis on the cast sample can be found in

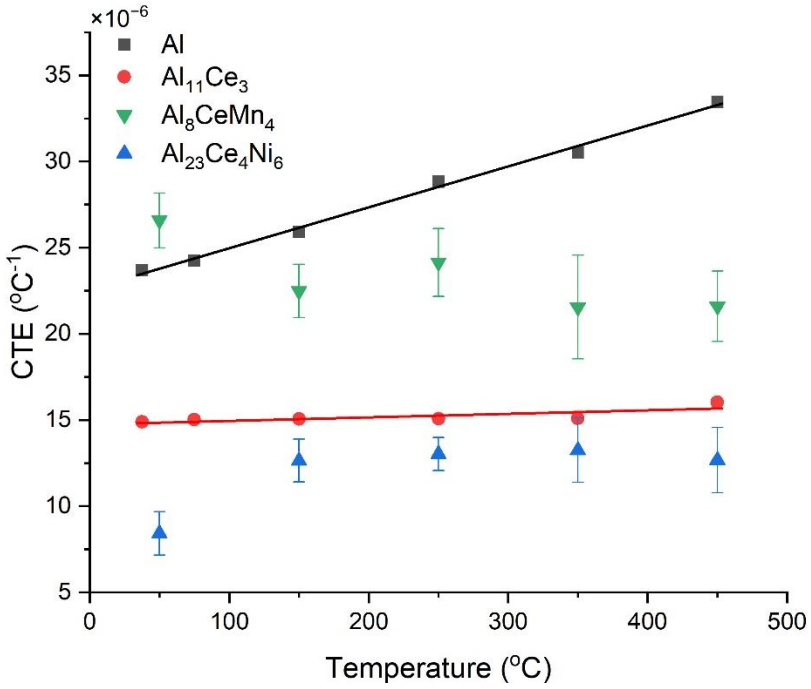

Figure 20. Temperature-dependent coefficients of thermal expansion determined from TDXRD on a thin film region that contained both the $Al_{23}Ce_4Ni_6$ and Al_8CeMn_4 intermetallic phases compared to pure Al and $Al_{11}Ce_3$ intermetallic phases.

supplement). XRD on the cast sample revealed 65 wt.% of the targeted $Al_{23}Ce_4Ni_6$ phase; the remainder of the sample was split between $Al_{11}Ce_3$ and two other AlCeNi ternary phases. These samples were ground into a fine powder and the CTEs were measured under the same conditions as the thin films, but additional temperature increments were added for the $Al_{23}Ce_4Ni_6$ to further explore the temperature dependence in more detail (see supplemental information). The cast bulk sample results with comparisons to pure Al and $Al_{11}Ce_3$ taken from the same measurement are shown in Figure 21. Rietveld analysis on the full XRD patterns were performed to extract each of the lattice parameters at the various temperatures. Bulk Al_8CeMn_4 demonstrates similar behavior to the thin film results and confirms the negative CTE temperature dependence. However, the magnitude of the temperature coefficient is smaller in the bulk Al_8CeMn_4 sample (-3.27×10^{-9}) relative to that of the thin film (-9.09×10^{-9}), consistent with substrate latching. Starting at low temperature, the CTE for $Al_{23}Ce_4Ni_6$ has a small value of $\approx5\times10^{-6}$ $^oC^{-1}$ at -225 ^oC and increases to a local maximum of $\sim15\times10^{-6}$ $^oC^{-1}$ at approximately -100 ^oC. Above -100 ^oC, the CTE decreases to a local minimum of $\sim10\times10^{-6}$ $^oC^{-1}$ at ≈75 ^oC. After reaching this minimum, the CTE increases to $\sim14\times10^{-6}$ $^oC^{-1}$ at 200 ^oC, at which point the CTE remains relatively stable to ≈550 ^oC. A neutron experiment on the NOMAD beamline was also performed to confirm this peculiar behavior and was consistent with x-ray measurements, as shown in Figure 21. The low CTE results of the $Al_{23}Ce_4Ni_6$ phase, particularly in the 25 to 200 ^oC range, make it an intriguing candidate for various applications. Magnetic and electron transport experiments were performed in an attempt to rationalize the anomalous behavior of the CTE around room temperature.

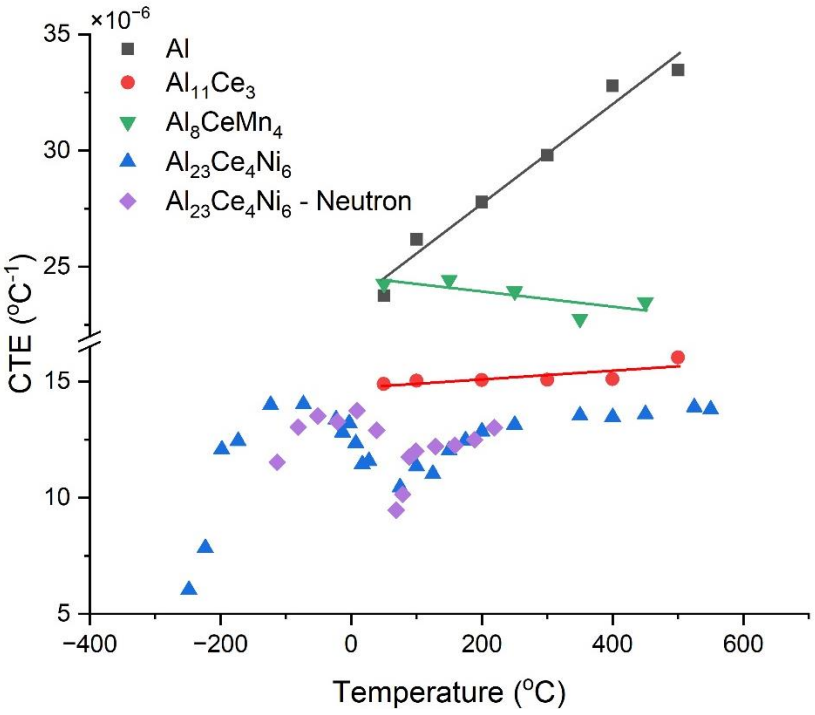

Figure 21. CTE values for bulk $Al_{23}Ce_4Ni_6$ intermetallic collected via XRD and NOMAD (neutron) experiments compared to bulk Al, $Al_{11}Ce_3$, and Al_8CeMn_4

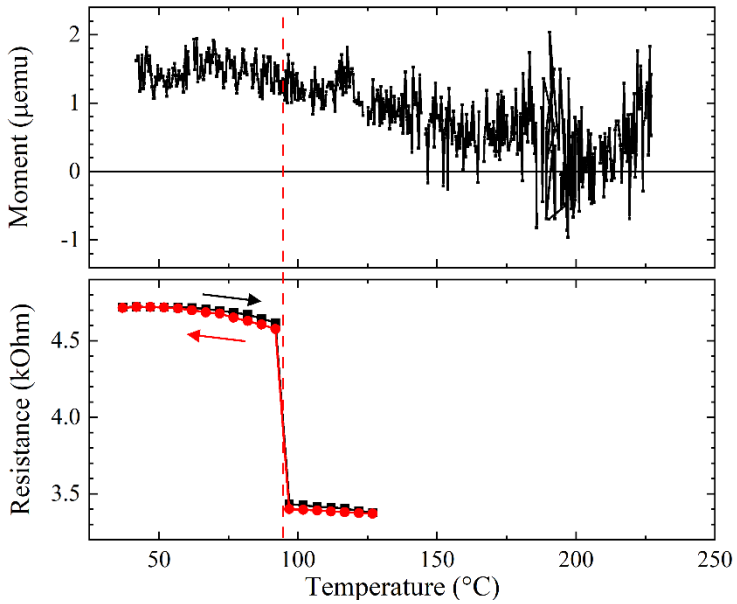

Figure 22. Magnetic moment and resistance measured against temperature for $Al_{23}Ce_4Ni_6$. Resistance measurements were taken on heating (black) and cooling (red) to confirm the discontinuity.

Magnetometry and electrical resistance measurements

Magnetometry versus temperature measurements, as shown in Figure 22, were performed as described in the Materials and methods section. The measurement shows no appreciable change in the magnitude of the measured moment or the temperature-dependent slope in the temperature range of interest; thus, the magnetic measurements suggest that no magnetic phase transition can be correlated to the anomalous CTE feature.

Resistance versus temperature measurements, also shown in Figure 22, were performed between 25 °C and 125 °C. As the temperature is increased from room temperature, the resistance gradually decreases at a rate of ≈4% per 100 °C, behaving as an insulator or semiconductor. At 95 °C the resistance rapidly drops, decreasing by 26% of the measured value over 5 °C. After the drop, the resistance returned to a gradually decreasing trend. Increasing the temperature, the resistance returns to its original value. Using the dashed red line as a guide to the eye confirms that changes to the electronic structure do not generate a corresponding magnetic response. The notable drop in the resistance may indicate some form of charge ordering, such as a change in orbital occupancy, valence of the Ce, or delocalization, all of which will result in changes in the resistivity. Considering the electron density of states [112], there is a large peak resulting from the Ce-4f orbital just above the Fermi level. This peak grows rapidly, starting precisely at the Fermi energy, and achieves a maximum at 430 meV; the thermal energy at 90 ^{o}C is 31 meV, providing a $\Delta E/k_BT$ of 13× at its peak. This indicates that a Mott-like transition is possible: increasing the temperature rapidly increases the probability of thermal excitation of electrons from the Fermi energy to this valance band. It is notable also that Gout et al. [112] reports $Al_{23}Ce_4Ni_6$

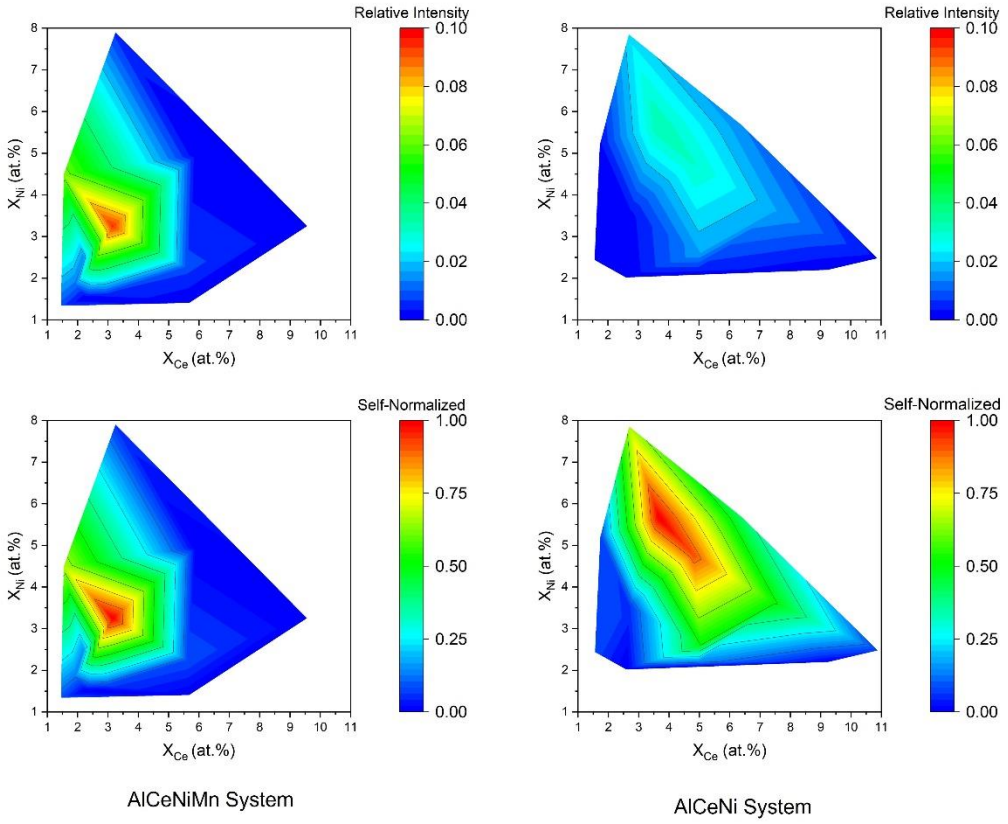

Figure 23.Comparison of the formation range of the Al23Ce4Ni6 intermetallic phase in the quaternary AlCeNiMn system versus the ternary AlCeNi system based on relative intensity of the Al (111) peak. The raw relative intensity values and self-normalized are shown to highlight the stabilizing effect of Mn and their respective formation ranges.

to be a metal (decreasing resistance with decreasing temperature) with an exceedingly flat R versus T curve between -175 and 25 ^{o}C, while the current work sees a slight slope with the opposite polarity (increasing resistance with decreasing temperature) at T>25 ^{o}C, with a behavior more indicative of an insulator or semiconductor.

The CTE can also be affected by these electronic changes. Specifically, the CTE is defined by the symmetry of the Lennard-Jones potential, which itself is determined by an intermolecular pair potential containing the attractive London dispersion force and Pauli repulsion force. The London dispersion force is a consequence of thermally driven inhomogeneities in the electronic orbitals and a resulting electrostatic attraction. The counter force is the Pauli repulsion, which occurs as a consequence of orbital overlap and occupancy. Changes in the orbital occupancy or delocalization effects (which occur as electrons are excited into the unoccupied Ce-4f orbital) will change the balance of these forces. Therefore, the potential well may increase in its symmetry, reducing the CTE. The coupling between a Mott transition and the CTE has been reported previously in metal-organic hybrid structures [129].

Thermodynamic assessment

The $Al_{23}Ce_4Ni_6$ phase was observed in the quaternary $Al_{100-x-y-z}Ce_xNi_yMn_z$ thin film system. To further explore this phase, a new sample was sputtered with only the Al-Ce-Ni ternary system. Interestingly, it was found that the formation range for the $Al_{23}Ce_4Ni_6$ phase shifted to higher Ce and Ni concentrations without the Mn additions. The formation ranges based on the normalized relative intensity of the corresponding $Al_{23}Ce_4Ni_6$ phase peaks are shown in Figure 23. The quaternary system only required approximately 1.5 at.%

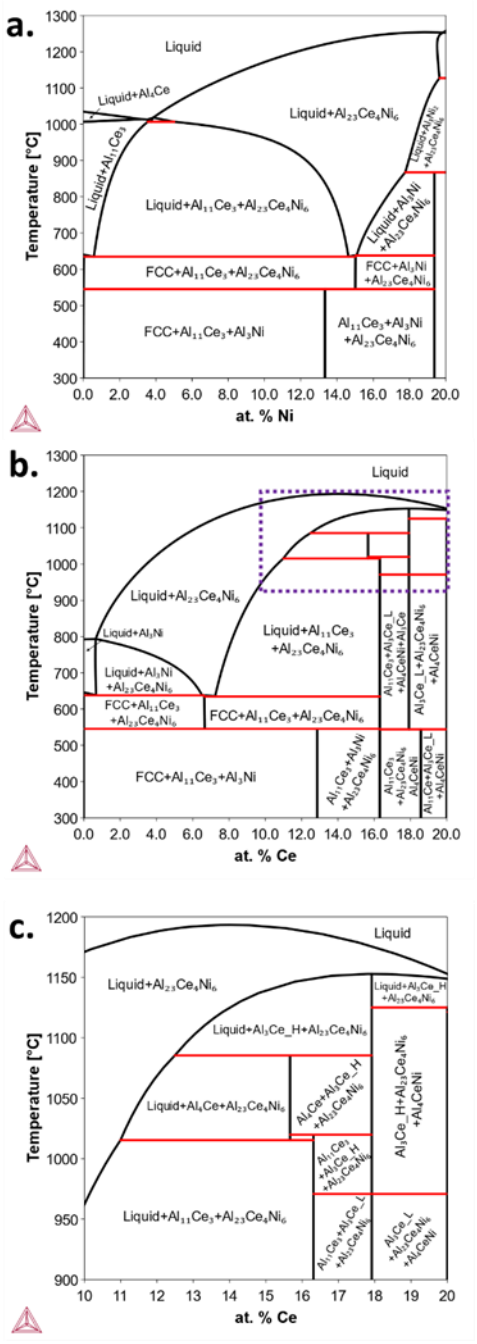

Figure 24. Calculated phase diagram of the Al-Ce-Ni system: a.10 at. % Ce isopleth, b. 10 at. % Ni isopleth, and c. enlarged region indicated in b.

Mn to shift the formation range of the $Al_{23}Ce_4Ni_6$ phase. The non-normalized relative intensities to the Al (111) peak are also given in Figure 23. As can be seen, the Mn containing system has a stronger overall relative intensity compared to that of the ternary Al-Ce-Ni system. This suggests that the formation range shifts with the addition of Mn and that the phase forms more readily in the quaternary system than the ternary system. This behavior was further explored in bulk castings. Two samples of $Al_{94.6}Ce_{2.4}Ni_{2.3}Mn_{0.7}$ and $Al_{95.3}Ce_{2.4}Ni_{2.3}$ were cast. The sample without Mn does not form the $Al_{23}Ce_4Ni_6$ phase, whereas the sample with only 0.7 at.% Mn does form about 3 vol.% of the $Al_{23}Ce_4Ni_6$ phase. The Rietveld refinements are shown in supplemental information for these bulk alloys. Thus, it is believed that Mn acts as a stabilizer for the $Al_{23}Ce_4Ni_6$ phase as it does for other intermetallics in Ti alloys, various steel alloys, and others [130–134]. Further investigation into other stabilizers and compositions can be performed to optimize the formation of the $Al_{23}Ce_4Ni_6$ phase. Additionally, thermal treatments can be explored to optimize the phase fraction.

The ThermoCalc software and TCAL8 [135] thermodynamic database were employed to better understand phase equilibria involving the $Al_{23}Ce_4Ni_6$ phase. Figure 24 presents 10 at. % Ce and 10 at. % Ni calculated vertical sections of the Al-Ce-Ni phase diagram. Both phase diagrams predict $Al_{23}Ce_4Ni_6$ as the primary solidification phase over much of the composition range. In contrast, Tang et al. [114] reported primary solidification of the Al_4CeNi ternary intermetallic phase over nearly the entire composition range with $Al_{23}Ce_4Ni_6$ forming via a peritectic-type reaction,

$$L + Al_4CeNi + Al_5CeNi_2 \rightarrow L + Al_{23}Ce_4Ni_6$$

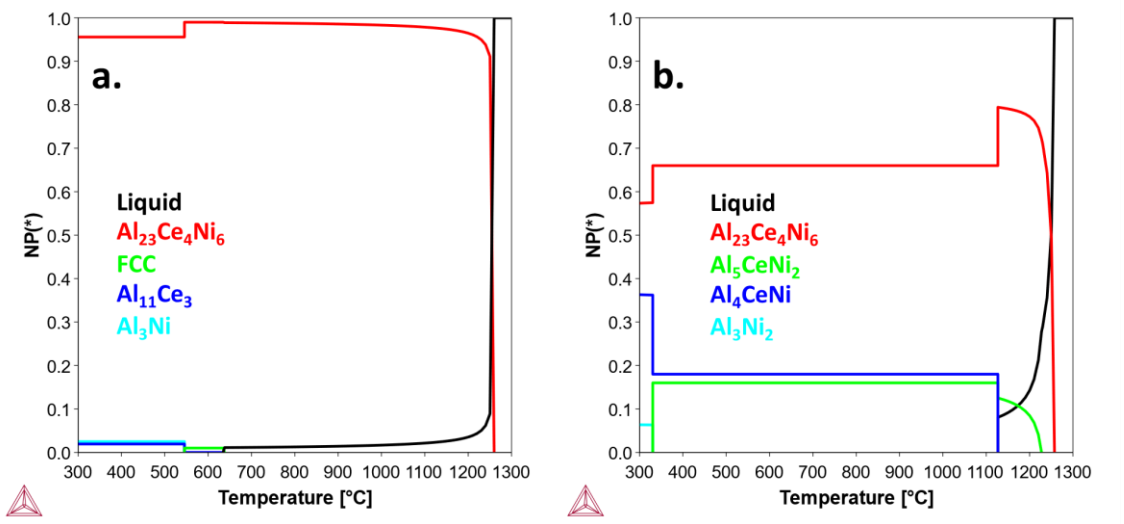

Figure 25. Calculated phases and phase fractions as a function of temperature for the alloys a. Al-12Ce-18Ni and b. Al-13Ce-19Ni.

Wu et al. [116] also reported no ternary $Al_{23}Ce_4Ni_6$ phase, although the compositions of their alloys were lean in Ce and Ni and far from the stoichiometry of $Al_{23}Ce_4Ni_6$.

Figure 25 presents phase diagrams (phase fractions versus temperature) for two alloys, Al-12Ce-18Ni and Al-13Ce-19Ni, which have less than and more than the stoichiometric Ce and Ni concentrations for $Al_{23}Ce_4Ni_6$, respectively. There is a dramatic difference in the amount of the expected phase in the two alloys. If the composition is slightly lower than stoichiometry (Al-12Ce-18Ni), the equilibrium microstructure is predicted to be >90 % $Al_{23}Ce_4Ni_6$ above about 550 °C, with the rest of the microstructure comprised of small amounts of FCC Al, $Al_{11}Ce_3$, and Al_3Ni, Figure 25a. Conversely, when the composition is slightly higher than stoichiometry, the equilibrium microstructure contains only ≈70 % $Al_{23}Ce_4Ni_6$ and 15-20 % each of Al_5CeNi_2 and Al_4CeNi, Figure 25b. The predicted equilibrium microstructure of Al-17Ce-10Ni (not shown) is 65 % FCC Al and 35 % $Al_{23}Ce_4Ni_6$ between 550 °C and the solidus near 630 °C; below 550 °C, $Al_{23}Ce_4Ni_6$ is expected to decompose into $Al_{11}Ce_3$ and Al_3Ni (and FCC Al). Because the current TCAL8 database considers neither the quaternary Al-Ce-Mn-Ni system nor solubility of Mn in $Al_{23}Ce_4Ni_6$, the role that Mn may play in the phase stability of $Al_{23}Ce_4Ni_6$ cannot be probed.

The present work clearly identifies $Al_{23}Ce_4Ni_6$ in the thin film combinatorial library, but subsequent attempts to produce an alloy with a high volume fraction of the ternary phase have been largely unsuccessful. The observed microstructure of the stoichiometric alloy is very similar to that predicted for an alloy with Ce and Ni contents above $Al_{23}Ce_4Ni_6$, strongly suggesting that the actual alloy composition was slightly richer in Ce and Ni than

intended. The Al-17Ce-10Ni composition contained almost no $Al_{23}Ce_4Ni_6$ in either the as-cast state or after annealing at 550 °C for 24 h, despite a calculated fraction of 35 % between 550 °C and melting. The reason that it does not show up in the as-cast material is likely related to kinetics, i.e., the phase is difficult to nucleate upon solidification, allowing the binary intermetallic phase to dominate the solidification microstructure. Further, the chosen annealing temperature of 550 °C is likely too low to promote $Al_{23}Ce_4Ni_6$, either because the driving force for its formation is too low or because the calculated temperature at which it forms is incorrect. The temperature reported by Tang et al. [115] was ≈500 °C. However, most of the available experimental data have been collected at 500 °C and 800 °C, leaving a large uncertainty in the stability limit of the phase [136]. Current work by Kozakevich et al. demonstrates $Al_{23}Ce_4Ni_6$ can be formed in appreciable quantities by adjusting the solidification kinetics through cooling rate in compositions similar to those provided in this study [137]. Additional recent work by Perrin et al. also demonstrates the effect of Mn on the eutectic phase equilibria in Al-Ce-Ni alloys [138].

Conclusion

The crystal structure, film morphology, electrical resistivity, and temperature-dependent coefficients of thermal expansion are all correlated to the $Al_{100-x-y-z}Ce_xNi_yMn_z$ composition. The co-sputtered films form a continuous composition gradient of the various constituents. In the as-deposited state, the Al (111) peak is present. Peak broadening and shifting indicate the formation of a metastable solid solution. Annealing leads to the formation of Al and the α-$Al_{11}Ce_3$, Al_8CeMn_4, and $Al_{23}Ce_4Ni_6$ intermetallics. Temperature-dependent CTE was investigated at a series of fixed composition points along the wafer via temperature-

dependent x-ray diffraction. The phases expand independently of one another. Al and α-$Al_{11}Ce_3$ CTEs were consistent with previously reported values. Al_8CeMn_4 demonstrated a negative temperature coefficient with the CTE decreasing from 27.5×10^{-6} $^oC^{-1}$ measured at an average temperature of 50 ^oC to 21.5×10^{-6} $^oC^{-1}$ at 500 ^oC, which was confirmed with bulk measurements. $Al_{23}Ce_4Ni_6$ exhibited an interesting CTE behavior with an anomalous minimum near room temperature, which was also confirmed with bulk measurements. The CTE for the bulk $Al_{23}Ce_4Ni_6$ intermetallic has a small value of $\approx5\times10^{-6}$ $^oC^{-1}$ at -225 ^oC and increases to a local maximum of $\approx15\times10^{-6}$ $^oC^{-1}$ around -100 ^oC. Subsequently, the CTE turns over to a minimum of $\approx10\times10^{-6}$ $^oC^{-1}$ at 75 ^oC and then increases to 14×10^{-6} $^oC^{-1}$ at 200 ^oC, at which point it seems to stabilize out to 500 ^oC. Further investigation to rationalize this anomalous behavior was conducted. Resistance measurements suggest that there is an electronic transition which is commensurate with the CTE anomaly, while magnetometry measurements show no meaningful changes. Thermodynamic assessment of the alloy system was conducted in an attempt to elucidate a heat treatment to promote the formation of a substantial amount of the $Al_{23}Ce_4Ni_6$ intermetallic to leverage the unique CTE behavior for industrial applications. The Al-17Ce-10Ni composition contained almost no $Al_{23}Ce_4Ni_6$ in either the as-cast state or after annealing at 550 °C for 24 h, despite a calculated fraction of 35 % between 550 °C and melting. Further evaluation suggests annealing at 575 °C should promote the formation of a greater volume fraction of $Al_{23}Ce_4Ni_6$. Further study into the mechanical properties and suitability of these alloys to replace traditional Al-Si alloys is required.

Acknowledgements

This work was supported by the Critical Materials Institute, an Energy Innovation Hub funded by the U.S. Department of Energy, Office of Energy Efficiency and Renewable Energy, Advanced Materials and Manufacturing Technologies Office, and Eck Industries. This work was performed under the auspices of the U.S. DOE. A portion of this research at ORNL's Spallation Neutron Source was sponsored by the Scientific User Facilities Division, Office of Basic Energy Sciences, U.S. DOE. W. R. M. acknowledges support from the Gordon and Betty Moore Foundation's EPiQS Initiative, Grant No. GBMF9069. The authors would like to acknowledge and thank Michael McGuire for performing the low temperature XRD measurements summarized as part of figure 6.

CHAPTER III

THIN FILM COMBINATORIAL SPUTTERING OF TATIHFZR COMPOSITIONALLY COMPLEX ALLOYS FOR RAPID MATERIALS DISCOVERY

Thin film combinatorial sputtering of TaTiHfZr compositionally complex alloys for rapid materials discovery

Reece Emery[1], Stephen B. Puplampu[2], Andrew Wood[2], Dayakar Penumadu[2], Eric A. Lass[1], Tao Liang[1], Haixuan Xu[1], John Lasseter[1], Kinga A. Unocic[3] Dustin A. Gilbert[1], C. Charlotte Buchanan[1], Peter K. Liaw[1], Philip D. Rack[1,*]

1. Department of Materials Science and Engineering, University of Tennessee, Knoxville, Tennessee 37996, USA
2. Department of Civil and Environmental Engineering, University of Tennessee, Knoxville, Tennessee 37996, USA
3. Center for Nanophase Materials Sciences, Oak Ridge National Laboratory, Oak Ridge, Tennessee 37830, USA

*corresponding author: prack@utk.edu

Keywords: combinatorial sputtering, thin films, nanoindentation, x-ray diffraction, high entropy alloys

Author Contributions

This work is in preparation for submission. The author of this dissertation was the lead writer and experimentalist for this paper. Synthesis of the film as well as characterization of the samples including scanning electron microscopy (SEM) and x-ray diffraction (XRD) measurements were performed by him. Collaborator John Lasseter aided in some SEM imaging. Collaborators Stephen Puplampu and Andrew Wood performed the nanoindentation experiments. Collaborator Tao Liang performed the DFT calculations.

The author performed all data analysis, interpretation, writing, and figure generation for the results included in this paper.

Introduction

Developing new materials that can operate under extreme environments such as ultrahigh temperatures (800 to >2200 ^{o}C), stresses (>1 GPa), resistance to energetic particle collisional damage, corrosive environments, and combinations thereof are necessary to achieve targets including cleaner, more efficient energy production and storage concepts (e.g., combined cycle power plants or fusion energy) and advanced propulsion technologies (e.g., hypersonic flight) [139,140]. Identifying and obtaining materials with properties that are optimized for a specific use case is at the core of materials science. However, traditional materials development relies on time-consuming and expensive experimental work. A particularly promising class of structural materials are compositionally complex metallic alloys (CCAs) – alloys containing four or more principal elements [141]. Whereas traditional metallurgy depends on the selection of a primary constituent to confer a primary property, CCAs have the promise to address several property requirements simultaneously. Due to the wide range of elements in the design palette, a plethora of CCAs are candidates for applications involving extreme operating conditions [142–145]. Thus, it is imperative to develop a methodology for the rapid identification and optimization of new compositionally complex alloy systems. Accordingly, this work develops a methodology combining combinatorial thin film sputtering, rapid characterization techniques, and bulk material upscaling.

Refractory CCAs (RCCAs) – or those containing mainly combinations of Ti, V, Zr, Nb, Mo, Cr, Ta, and W among others – are of particular interest for applications in extreme environments due to their high melting points, and combination of room temperature and high temperature mechanical properties [146–149]. RCCAs can take the form of single solid-solution phases rather than forming intermetallics. Typically, they take the form of either a hexagonal-close packed (HCP) or body-center cubic (BCC) crystal structure [150]. $Ta_wTi_xHf_yZr_z$ alloys (TTHZ alloys) and their variations have been of particular interest in the class of materials. TTHZ alloys have shown exceptional promise in biomedical applications where biocompatibility, modulus, corrosion resistance, and radiation compatibility are paramount [151,152]. However, they also show potential in high temperature applications. Specifically, TTHZ alloys have been shown to demonstrate TRansformation Induced Plasticity (TRIP) behavior [153]. TRIP was first observed in high performance steels where a strain-induced martensitic transformation leads to a considerable increase in both strength and plasticity [154–156]. A BCC TTHZ alloy was synthesized by Huang et al. and it was shown that TRIP behavior can be leveraged to inhibit early cracking of the brittle BCC phase providing an effective means to improve both strength and ductility [153]. At room-temperature Ta is the only element of the four that takes on a BCC structure. However, at elevated temperatures Hf, Zr, and Ti each transition to a BCC structure at 1749 ^oC, 863 ^oC, and 893 ^oC, respectively [157]. This suggests that by tuning the composition and phase stability, TRIP behavior may be observed at elevated temperatures thereby improving the high temperature strength and ductility of the alloy.

While these RCCAs are of interest, they can be hard to synthesize due to the high melting point of the constituent elements [149,158]. Therefore, reducing the number of compositions to explore, and thereby reducing the amount of processing optimization, can greatly accelerate materials development. Combinatorial thin films libraries have been utilized as a rapid materials discovery tool [21,33,159]. Co-sputtering is able to achieve thin film compositions that cover a large composition range, while allowing for the realization of metastable material configurations; for example, supersaturated solid solutions commonly result in various as-deposited sputtered alloys due to the high energy deposition process and fast cooling rates [5,6,10]. Subsequent annealing of the film can lead to equilibrium phases of the system through phase separation, recrystallization, and grain growth though metastable phases may still be present [8,66]. We apply the thin film rapid materials discovery approach to the $Ta_wTi_xHf_yZr_z$ system as a cursory technique to identify candidate phases and compositions for various extreme environment applications. Material properties such as crystal structure, mechanical properties (modulus and hardness), thermal stability, and corrosion resistance are all correlated to the $Ta_wTi_xHf_yZr_z$ composition. These material properties identified in the films are used as a semi-quantitative guide to rapidly down select promising alloy compositions. Previous thin film work has shown good agreement between thin film and upscaled materials properties such as coefficient of thermal expansion and other mechanical properties [38,160–164]. Other related work with refractory high entropy alloy (RHEA) thin films suggests combinatorial thin films is a promising and cost-effective way to not only investigate properties (such as mechanical properties and corrosion behavior), but also is promising as tool for advanced

coating materials [165–167]. Identified compositions of interest can be upscaled into bulk cast alloys for further, more extensive investigation in the desired application space.

Elastic and plastic properties are a key criterion in the down selection when transitioning to bulk materials. Substrate effects on the modulus and hardness values obtained through the nanoindentation of thin films have been studied at length [37,39,164,168–170]. Doerner and Nix first developed a method for extracting mechanical properties from nanoindentation, which adopted the Loubet et al. solution of Sneddon for the elastic deformation of an isotropic elastic material with a flat-ended cylindrical punch [171–173]. The standard modulus analysis for thin films is the Oliver and Pharr method where the reduced (measured) modulus, E_r is given by:

$$\frac{1}{E_r} = \frac{(1-\nu_i^2)}{E_i} + \frac{(1-\nu^2)}{E} \quad (1)$$

where ν_i and E_i are the Poisson's ratio and elastic modulus, respectively, of the diamond Berkovich indenter tip and ν and E are the Poisson's ratio and elastic modulus of the material being tested. However, this equation only holds true in monolithic systems (i.e. when the film and substrate have similar elastic properties [174–176]. King modified the Doerner and Nix relationship to account for materials deposited on non-similar substrates. Here the reduced modulus is defined as:

$$\frac{1}{E_r} = \frac{(1-\nu_i^2)}{E_i} + \frac{(1-\nu_f^2)}{E_f}\left(1 - e^{-\frac{\alpha t}{a}}\right) + \frac{(1-\nu_s^2)}{E_s}\left(e^{-\frac{\alpha t}{a}}\right) \quad (2)$$

where *s* denotes the elastic properties of the substrate, *f* denotes the elastic properties of the film, *a* is the square root of the projected contact area, *t* is the thickness of the film below the indentation, and α is a numerical scaling factor that is a function of *a/t* and the indenter geometry [177,178].

Materials and methods

Sputtering Conditions

$Ta_wTi_xHf_yZr_z$ alloys were co-sputtered from pure Ta, Ti, Hf, and Zr targets to form a combinatorial libraries across a 100 mm diameter SiO_2-coated (500 nm) Si substrate (500 µm) and a fused silica substrate. The substrates were fixed (not rotated) to generate the desired composition gradient. An original base pressure of $\approx 3\times10^{-7}$ Torr was achieved in the system. The Ta target was powered by a 120 W DC source, the Ti by a 190 W DC source, Hf by a 165 W RF source, and Zr by a 145 W RF source in a 5 mTorr Ar ambient atmosphere for 70 minutes such that a minimum thickness of approximately 2 µm is obtained with a target center composition of $Ta_{40}Ti_{20}Hf_{20}Zr_{20}$. The approximate deposition rate at the respective target powers at the substrate center were Ta = 13.5 nm/min, Ti = 5.00 nm/min, Hf = 8.30 nm/min, and Zr = 6.14 nm/min.

Thin film annealing conditions

To measure the nanoindentation, the film was cut into 1" squares. Subsequent to measuring the as-deposited indentation, these chips were annealed in a vacuum furnace with a base pressure of $\approx 3\times10^{-7}$ Torr by radiation heating from halogen lamps to 1000 ^{o}C where they were held for one hour. Larger samples for further characterization were annealed in a 4" tube furnace that was pumped out with a roughing pump and then back filled with an Ar + 2.5% H mixture. These samples were heated to 1200 °C, held for one hour, and allowed to furnace cool.

X-ray conditions

Room temperature x-ray diffraction (XRD) patterns were measured using a Malvern Panalytical X'Pert^3 MRD diffractometer, and temperature-dependent XRD (TDXRD) experiments were performed using a Malvern Panalytical Empyrean diffractometer. A 2θ-ω scan with an ω offset of 3° and Cu Kα radiation (λ=0.154 nm) was used for all experiments. Room temperature XRD experiments on as-deposited and annealed samples were performed from 25° to 80° 2θ with a step size of 0.05° (the total time of each scan was 30 min). Following annealing, the XRD experiment was repeated with the same conditions to compare the change in crystal structure. TDXRD experiments were performed from 20° to 70° 2θ using a 0.39° step size (the total time of each scan was 30 min). The sample was heated *in situ* from 25 °C to 1100 °C in an Ar-3% Hydrogen atmosphere with a heating rate of 5 °C/min. Data was collected at 25, 200, 400, 600, 800, 1000 and 1100 °C after a five-minute hold at each temperature to allow the sample to reach thermal equilibrium. The same conditions were used during the cooling cycle. In total, thirteen measurements were taken for each complete temperature cycle. Temperature was measured in the heated stage via a thermocouple. A series of calibration tests were performed before starting TDXRD on samples. Alumina was used as a calibration sample and compared to literature, which can be found in the supplemental information [125–127].

Scanning Electron Microscopy and Energy dispersive X-ray spectroscopy

Energy dispersive x-ray spectroscopy (EDXS) and scanning electron microscopy (SEM) were conducted on a Carl Zeiss MERLIN SEM. The combinatorially sputtered

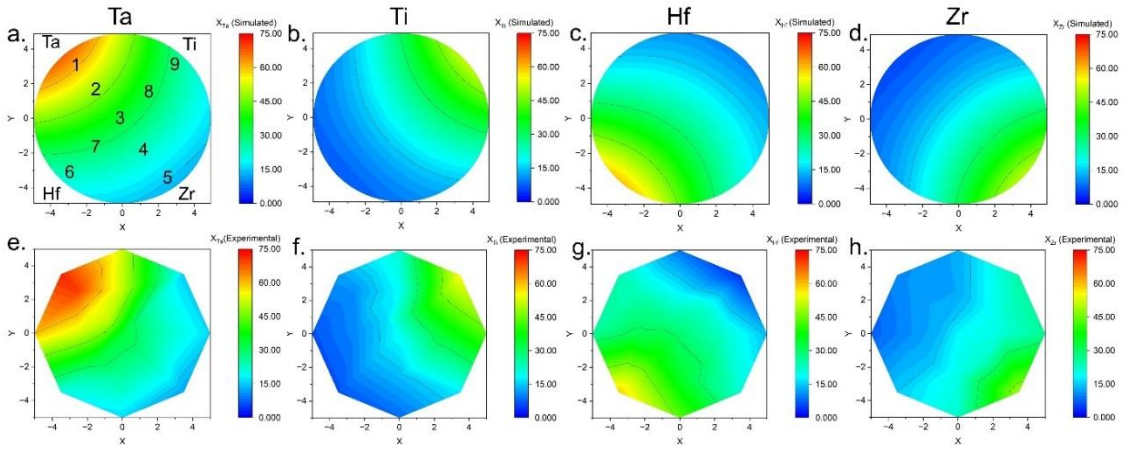

Figure 26. Simulated (a, b, c, d) and experimentally determined (e, f, g, h) composition gradient profiles for Ta (a,e), Ti (b,f), Hf (c,g), and Zr (d,h) on the 100 mm diameter combinatorial wafer. Note the approximate target locations relative to the substrate in a. The numbers in a denote the locations of XRD patterns taken in the as-deposited state. The approximate equiatomic location is position 4.

$Ta_wTi_xHf_yZr_z$ as-deposited sample was measured at 17 equally spaced increments across the wafer. An accelerating voltage of 10 keV was used for EDXS.

Nanoindentation

Indentation testing was carried out on an iMicro (NanoMechanics Inc.) nano indenter equipped with a Berkovich (three-sided pyramid, 65.3° cone angle) diamond tip. Modulus and hardness values were obtained as a function of depth based on the Oliver-Pharr continuous stiffness method (CSM) [174,182]. Substrate effects on measured modulus and hardness values were evaluated by analyzing the modulus and hardness versus depth. Indents depths of 50 nm, 100 nm, 200 nm, 300 nm, and 500 nm were compared. 175 nm was determined to be the optimal indentation depth with a 160 nm reporting depth (90% of total depth) for modulus and hardness values. Modulus was then corrected with equation 2. Grids of 6 by 6 indents were made using 3 μm spacing between indents. Other fixed parameters that were set for testing include Poison's ratio is assumed to be 0.3, a tapering constant of 350, and stiffness for contact 50 N/m. Additionally, pile ups were considered, and a depth correction Q was integrated into the hardness and modulus versus depth curves. Relative indentation locations as well as surface roughness can be found in supplemental information.

Results and Discussion

Full Wafer Characterization

Figure 16 illustrates the composition profiles for Ta, Ti, Hf, and Zr across the 100 mm diameter combinatorial wafer. The system was oriented such that primary gradients are Ta

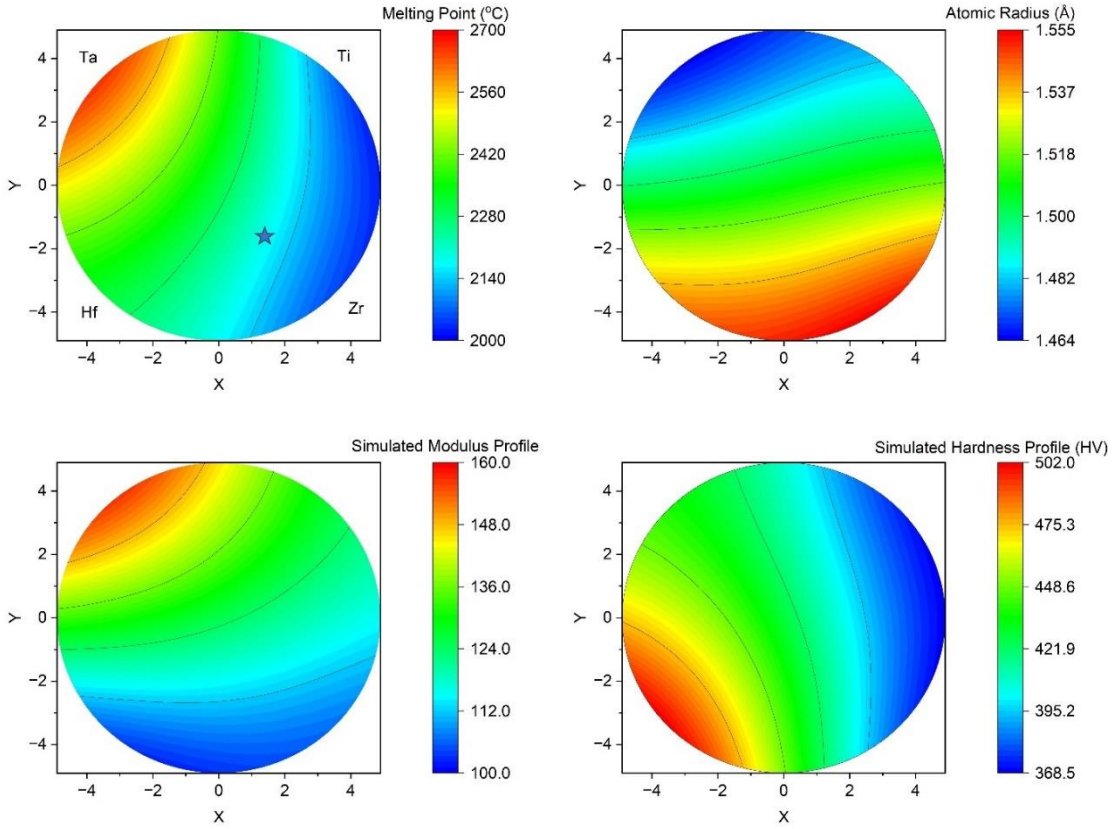

Figure 27. Rule of mixture approximations for melting point, atomic radius, modulus, and hardness determined from the simulated combinatorial composition gradient. The star in a denotes the equiatomic position.

to Zr and Ti to Hf. Figure 26 (a-d) show simulated composition profiles. For the simulated composition profiles, the four sputtering guns were modeled as individual Knudson surface sources, where the parameters specific to our system have been previously determined [4,6,9]. Figure 26e-h show the experimentally determined composition profiles. Compositions were measured at 17 points across the wafer using EDXS (see sample spectra in supplemental information 2). Good agreement between the simulated and experimental composition and thickness profiles has been shown previously [5,6,10] and is observed in Figure 26. The Ta composition varies from ~20 to 75 at.%, Ti, Hf and Zr each from ~5 to 55 at.%. The center composition was tuned such that Ti, Hf and Zr are close to equiatomic (~20.8 at.%) with the balance being Ta (37.5 at.%).

Rule of mixture approximations of the melting temperature, atomic radius, modulus and hardness based on the simulated composition profiles were generated to provide an initial guideline for the material system. Further, the data collected was directly compared to these approximations to determine their deviation and understand the unique attributes of this material system. These approximations are shown in Figure 27. Note the values assume the hexagonal close packed (HCP) crystal structure for Hf, Zr and Ti, and tetragonal phase (β) for the Ta, where β-Ta has been shown to have a significantly higher hardness value than BCC Ta while only having a mild effect on the modulus value [183–185].

To examine the crystal structure of the films in the as-deposited state of the $Ta_wTi_xHf_yZr_z$ thin film, XRD measurements were performed at 9 points across the sample. Five equispaced points were measured along the Ta to Zr gradient and 4 points were taken along the Hf to Ti gradient with the center point from the Ta to Zr scans being shared for a total

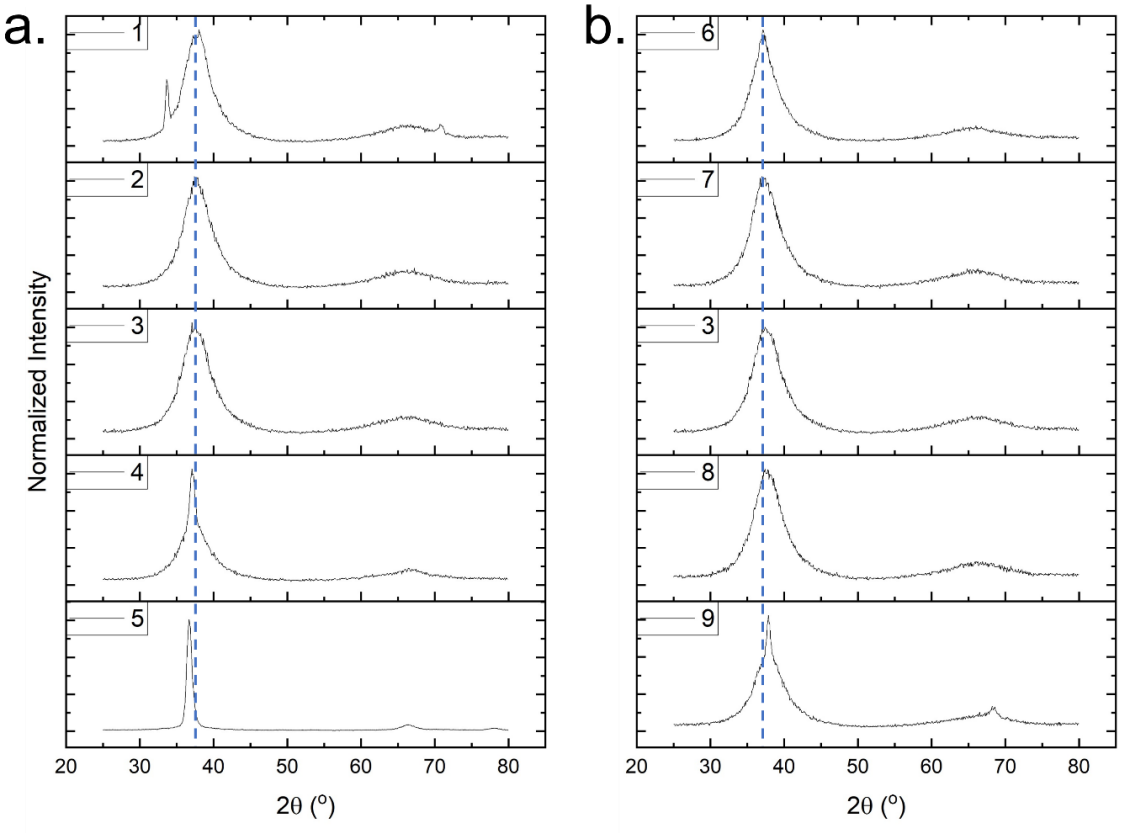

Figure 28. As-deposited XRD patterns for 10 points across the sample. 4a moves equispaced from the Ta to Zr rich edge. 4b moves equispaced from the Hf to Ti rich edge with the center points being the same for both.

of 5 points along each primary gradient line (see Figure 26a for positions). The as-deposited XRD results are shown in Figure 28. The BCC (110) reflection dominates in the as-deposited state. Note that the (110) orientation in BCC crystals has preferred orientation due to the low surface energy [186,187]. Broadening in this primary peak and shifts in the 2θ position suggest the formation of a metastable solid solution in the as-deposited film. The shifts in the peaks are consistent with the change in average atomic radius seen in Figure 27 with Ta having a smaller atom and shifting the peak to higher 2θ with increasing Ta concentration. While BCC is not the equilibrium phase for Hf, Ti, and Zr [157], it has been shown that these elements will take on a BCC structure during thin film deposition by varying deposition parameters and adding only nominal amounts of a BCC former such as Ta or Nb [169,188–193]. Slight peak sharpening also occurs at the Hf and Ti edges. This sharpening is also consistent with the relative melting points of Zr, Hf, and Ti. Additionally, at the high Ta edge, a secondary tetragonal peak emerges as shown in Figure 28a. While bulk tantalum normally has BCC structure (α-Ta), it has been shown that the metastable β-Ta can form in thin films depending on the deposition parameters [194–197]. XRD was also performed on an equivalent sample deposited on fused silica and cut into squares that for nanoindentation. The general locations of these squares are denoted in Figure 29a. Similarly, as in Figure 28, The BCC (110) reflection dominates in the as-deposited state shown in *Figure 29*(b-g). Broadening in this peak indicates a nanogranular film is realized and a solid solution is achieved in the as-deposited film state. XRD was repeated on these squares following a 1000 ^{o}C anneal as presented in *Figure 29*(h-m). Interestingly, the upper two squares with the highest Ta content showed little to no

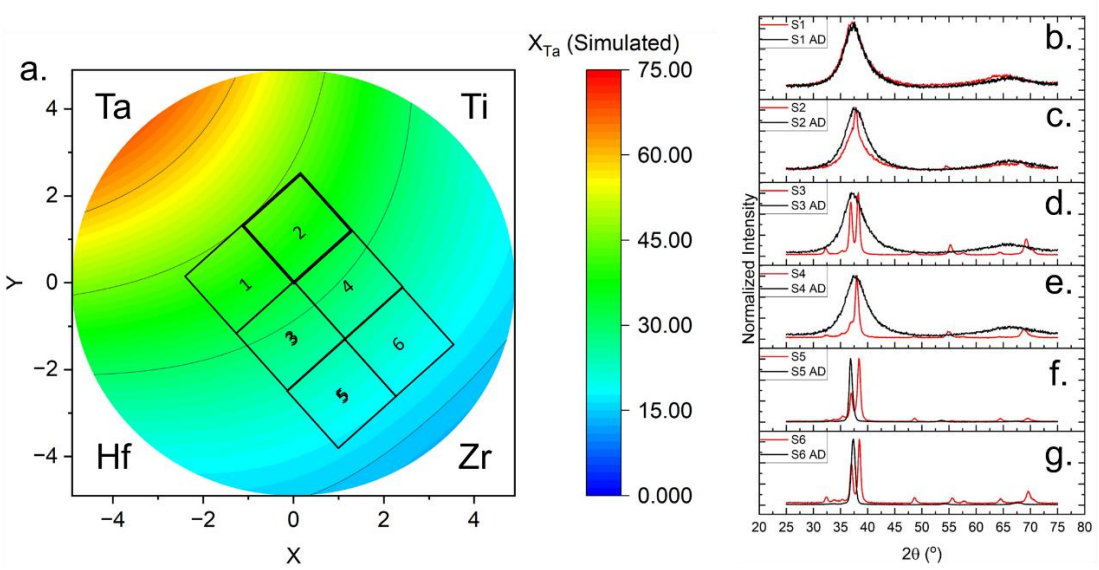

Figure 29. (a) Chips that were surveyed by nanoindentation.(b-g) Comparison of as-deposited and annealed XRD patterns at the center of the four nanoindentation chips of the $Ta_wTi_xHf_yZr_z$ alloy.

crystallization. This is consistent with the rule of mixtures melting temperature approximation, which suggests these compositions require a higher annealing temperature for recrystallization to occur (for alloys ~ 0.5 T_m). The middle two squares (S3 and S4) show good recrystallization. Rietveld analysis reveals that S3 recrystallizes as 68% BCC and 32% HCP and S4 recrystallizes as 62% BCC and 38% HCP. Further the two squares farthest from Ta (S5 and S6) also show good recrystallization. S5 recrystallizes as 56% BCC and 44% HCP with S6 recrystallizing as 52% BCC and 48% HCP. This trend underscores the effect of Ta on the stability in the BCC phase. The Rietveld analysis can be found in supplement information.

To understand the phase evolution during annealing, temperature-dependent x-ray diffraction was performed at the equiatomic position as shown in Figure 30. The system remains in a solid solution and the peak shifts lower 2θ up to 400 ºC. Recrystallization and an BCC-to-HCP phase transformation begins around 600 ℃ and recrystallization occurs at 800 ℃. Evolution of the phases shows a near 50/50 mix of HCP/BCC at 1100 ℃. Interestingly, upon slow cooling, the film is almost completely HCP, which is different from the annealed sample behavior in Figure 29. The main differentiating factor between the TDXRD sample and nanoindentation sample annealing recipes was cooling rate. The TDXRD sample was slow, program cooled at 10 ℃/min over the course of several hours while the nanoindentation samples cooled at a faster rate (the lamps were shut off and cooled as fast system would allow). This suggests the cooling rate plays a significant role in the phase evolution of this quaternary system.

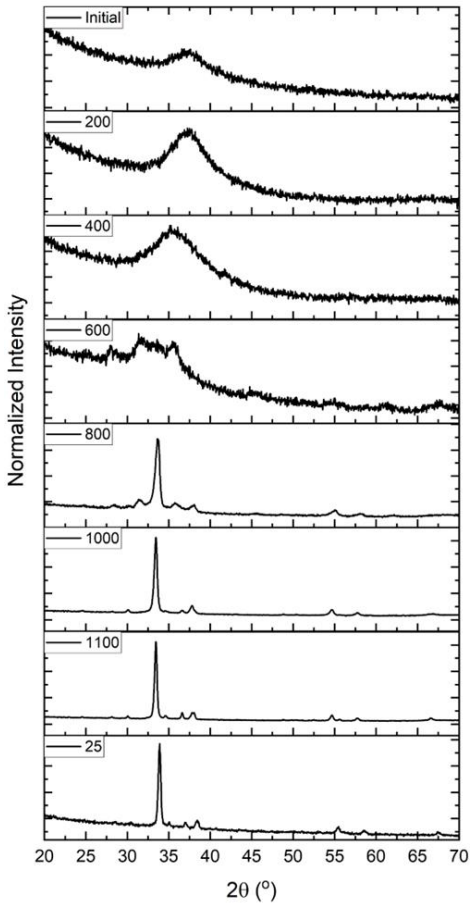

Figure 30. Temperature-dependent XRD scans performed on the approximately equiatomic composition.

Further investigation of the cooling rate was done on a bulk $Ta_{12.5}Ti_{29.2}Hf_{29.2}Zr_{29.2}$ alloy which was as-cast (fast cooled) and a slow furnace cooled. All illustrated in figure 30a), the as-cast state shows an entirely BCC structure. However, Figure 30c) shows that allowing the system to furnace cool after homogenization shows a dual phase HCP+BCC structure with the HCP phase being dominate at 92% of the phase fraction. Another processing methodology explored for its impact on phase equilibrium was cold rolling which should transform some amount of the material from BCC to HCP under some load. Figure 30c) shows that cold rolling the as-case sample to a 25% reduction leads to an entirely HCP structure. This indicates that this composition is extremely susceptible to TRIP behavior as previously reported in this alloy system [15]. Further, the furnace cooled sample that is predominantly HCP cannot be cold rolled without crumbling. This distinct change in rollability emphasizes the BCC-to-HCP TRIP behavior.

DFT calculations were performed to aid in the understanding of the phase stability and cooling rate dependence in the TTHZ alloy system. Based on the BCC to HCP formation energy difference shown in Figure 32, the energy barrier to form the HCP phase versus the expected BCC phase is very low. This is particularly true in indentation squares S5 and S6 where these values are approximately equal. This is in line with the observed near 50/50 phase ratio of BCC to HCP determined via XRD and Rietveld refinement. Similarly, as we move toward the Ta side, we see this ratio shift up to approximately 70/30 in S3 and 60/40 in S4. The change in ratio of BCC to HCP is consistent with the difference in formation energy shown in Figure 32. However, this is nonlinear which is consistent with the difference in ratio between S3 and S4 where S3 seems more BCC form.

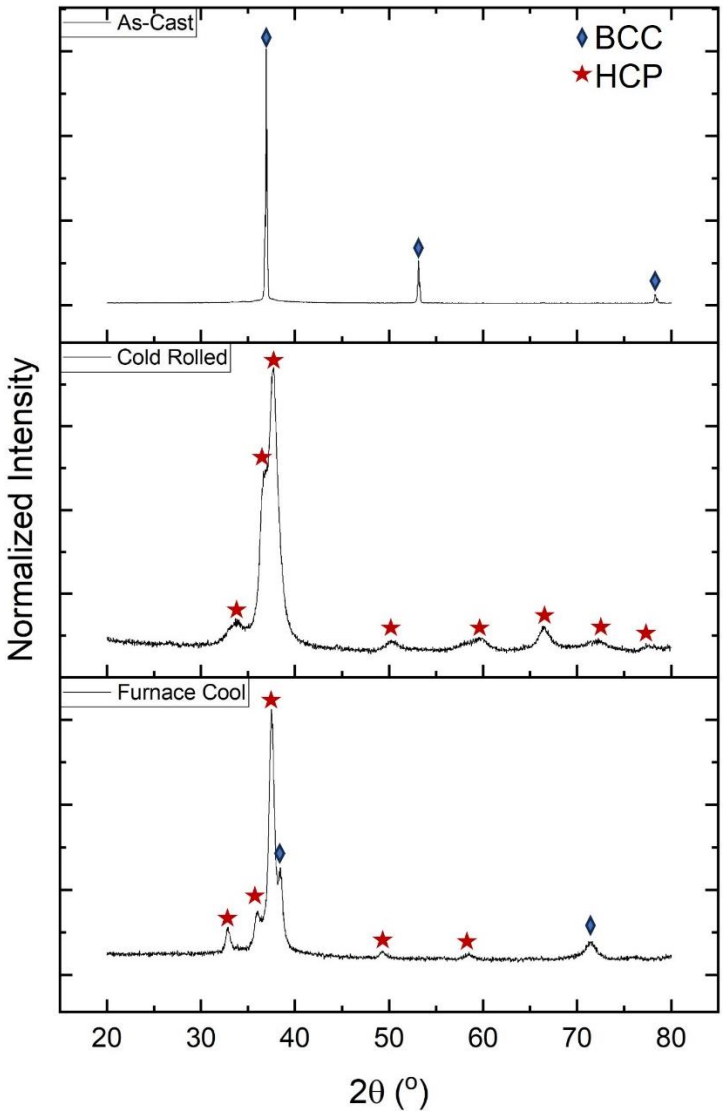

Figure 31. X-ray diffraction patterns for three bulk samples: as-cast, cold rolled, and furnace cooled after homogenization.

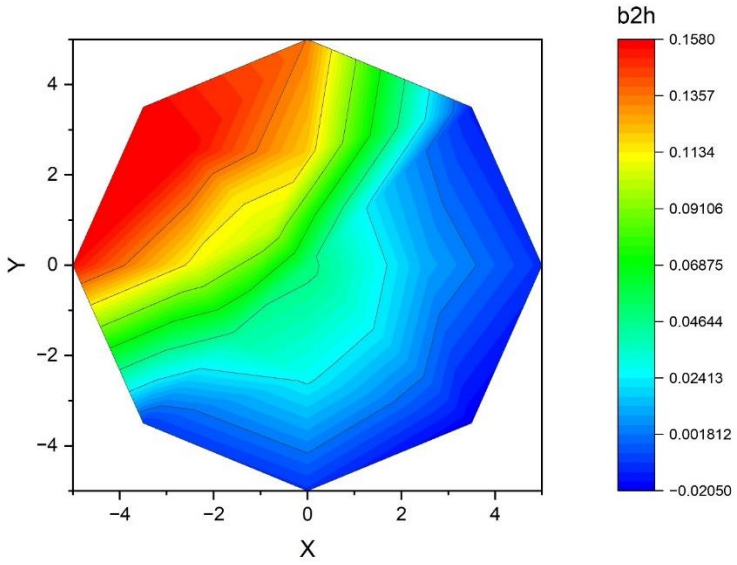

Figure 32. Computation modeling of BCC versus HCP phase stability. More positive values indicate higher BCC stability.

Nanoindentation

Nanoindentation results, specifically modulus and hardness, for the as-deposited sample are shown in Figure 33a and b, respectively. The as-deposited modulus results in general follow the rule of mixtures results, where the b Ta phase has the largest modulus and Zr is the lowest, thus the gradient along the Ta-Zr axis. The slight gradient in S5 and S6 that has a lower-to-higher gradient along the Ti-Hf gradient is counter to the rule of mixtures approximation. The hardness values for the composition range explored peak towards the high tantalum region whereas the rule of mixtures estimation suggests that the peak should appear in the Hf-rich region. While the Ta-Hf corner is the hardest, we attribute the observed hardness trend to convolution of the composition and grain size as Tantalum has the highest melting temperature and thus will tend toward smaller as-deposited grain size. SEM images confirm this trend. The system further deviates from both rule of mixtures approximations upon subsequent annealing. The modulus of the annealed film shown in *Figure **33***c homogenizes and reveals a minimum in the Ti rich square S4 and another minimum at the bottom of S5, which is rich in the low modulus Zr. The hardness on the other hand increases by almost a factor of two and the trend shifts from the as-deposited state. The increased hardness is attributed to precipitation hardening of the dual phase BCC and HCP system. The highest hardness in the annealed state is in S1 and S3 along the Hf edge. These trends are due to the high hardness of Hf and competing grain size effects as the tantalum content increases the melting temperature and thus less recrystallization and smaller grain size. Interestingly, there is also a local minimum in hardness around S2. Further, there seems to be a clear delineation in the hardness in the bottom two squares of

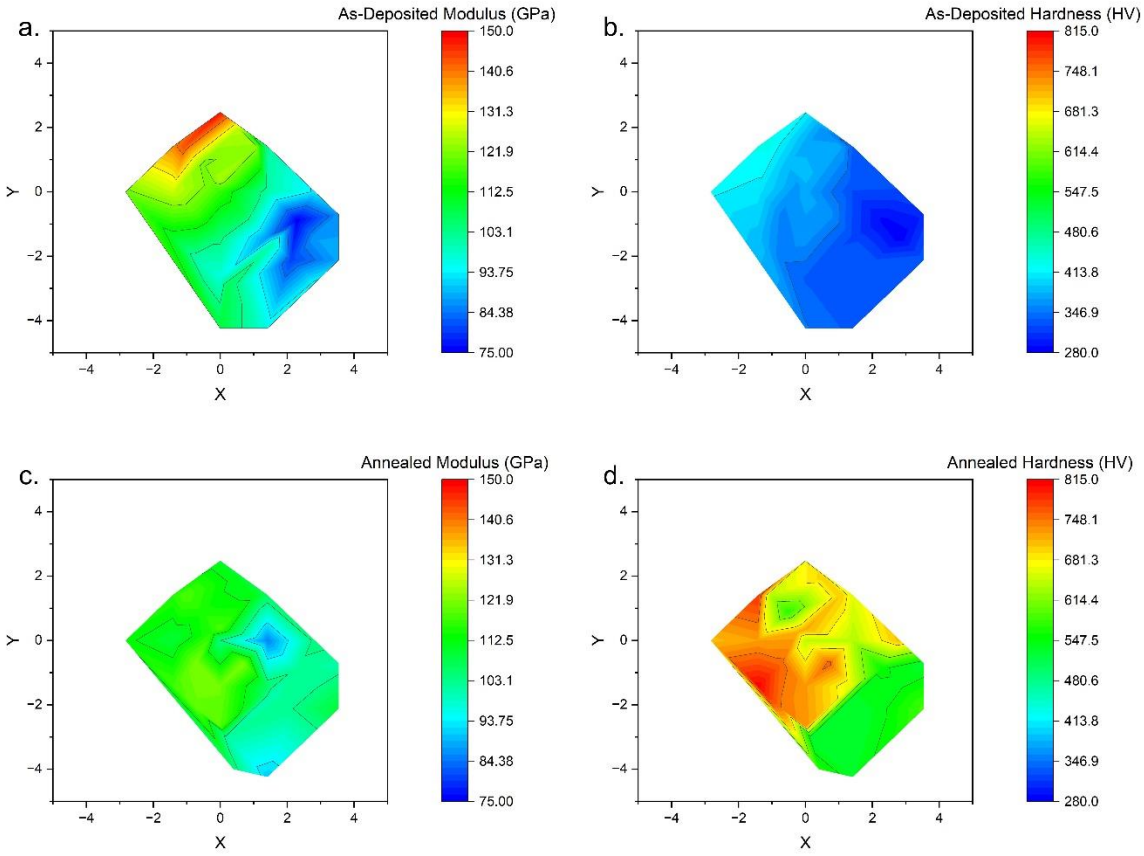

Figure 33. Modulus and Hardness maps for the as-deposited and annealed $Ta_wTi_xHf_yZr_z$ films.

the annealed samples. While this could just be variations due to the sample chemistry, this could be an indicator of TRIP behavior.

TRIP behavior can be identified in nanoindentation data through two means: dislocation bursts which leads to “pop-in” behavior resulting in discontinuities in the load depth curve and deviations where the slope of the load depth curve changes [78–83]. Both mechanisms are observed in the TTHZ films as shown in *Figure 34*. The “pop-in” behavior was observed primarily in the Ta rich regions. It should also be noted that this “pop-in” behavior can also be indicative of crack initiation [84,85]. Based on SEM imaging shown in *Figure 34*, it is likely that the pop-ins observed in these regions are likely due to their brittle nature and crack initiation. However, larger scale fluctuation behavior was seen in the low Ta regions. Hardness and modulus values versus depth are plotted for a few indents to illustrate this behavior. In *Figure 34*a, the hardness shows discontinuities in line with the load versus depth relationship, however, the modulus seems less sensitive to the “pop-in” dislocation bursts. On the other hand, the annealed sample in *Figure 34*b shows dramatic fluctuations in the hardness and modulus versus depth behavior in line with the deviations in the load depth curve. As stated previously, this behavior is predominantly seen in the annealed, low Ta regions. This is consistent with the lowest energy barrier between BCC and HCP phase formations determined by DFT calculations in *Figure **32*** and consistent with our bulk results above and [15]. Further, the grain size of the film is significantly smaller than the indentation size thereby limiting the grain boundary effects. AFM (S5) was performed on the sample and revealed a root mean square roughness of approximately 10 nm. All hardness and modulus data were reported starting at 20 nm to limit tip contact variation on

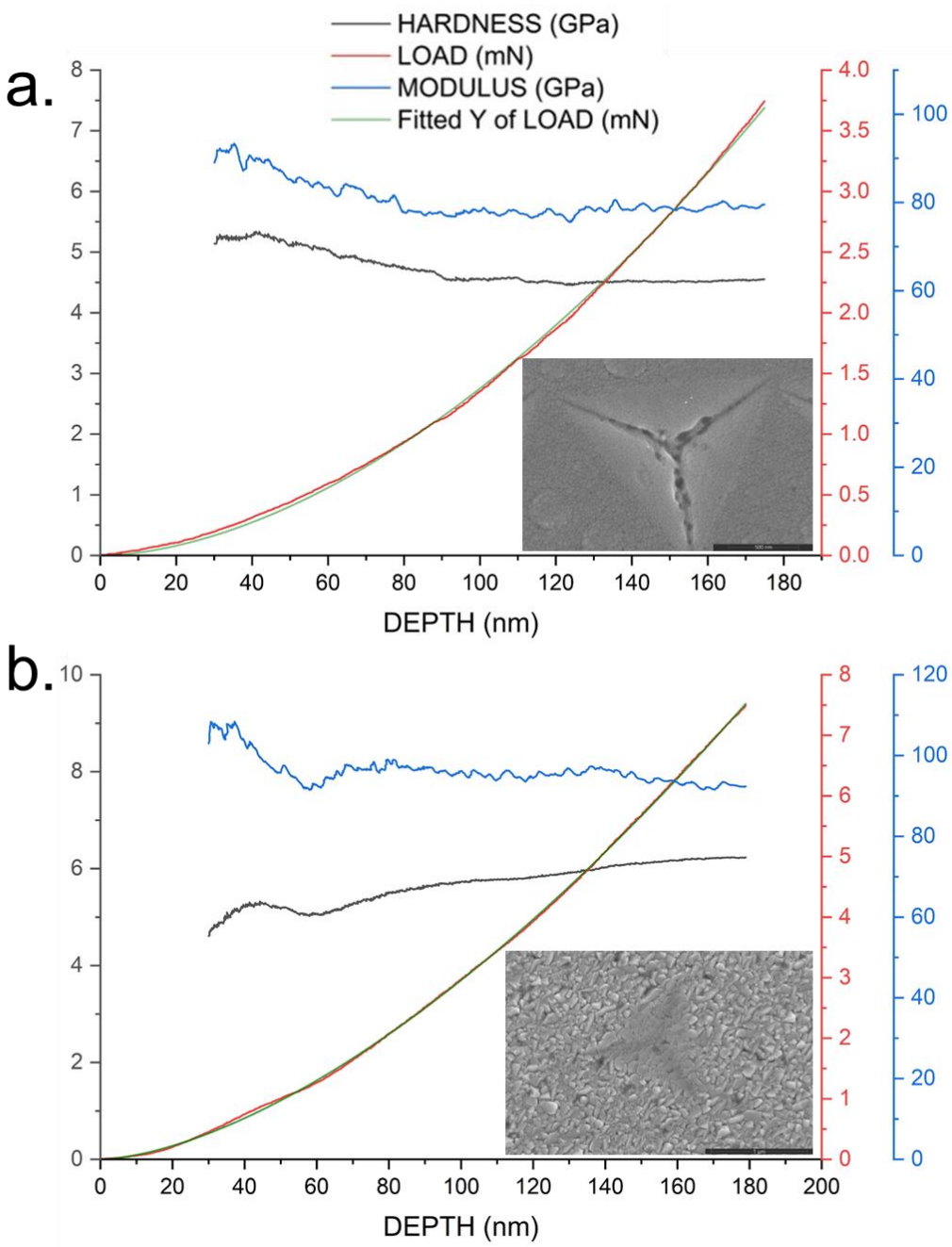

Figure 34. Plots of load, modulus and hardness versus depth showcasing the two means for identifying TRIP in nanoindentation data: (a) "pop-ins" and (b) "deviations or wobbles."

the sample. An example plot of load, hardness, and modulus versus depth for curves in S3 and S4 that do not show TRIP behavior is shown in supplement.

Conclusions

The crystal structure, film morphology, and mechanical properties (i.e. modulus and hardness) were all correlated to $Ta_wTi_xHf_yZr_z$ composition. The presence of Transformation Induced Plasticity (TRIP) was also explored and correlated to the $Ta_wTi_xHf_yZr_z$ composition. In the as-deposited state, the film shows a rule of mixtures based gradient in the properties of the film with the hardness and modulus being highest with the highest Ta content. Upon annealing, the film forms a dual phase BCC+HCP structure with the relative amounts of each phase being dependent on the Ta content. This is consistent with the relative difference in formation energy between the two phases as calculated with DFT. Further, the overall hardness of the film doubles upon annealing while the modulus values homogenize. By extracting the load-depth curves from indentation TRIP behavior can be seen via “wobbles” or deviations in the slope. TRIP is observed in the recrystallized section of the film with the lowest Ta content.

Acknowledgements

This research was primarily supported by the National Science Foundation Materials Research Science and Engineering Center program through the UT Knoxville Center for Advanced Materials and Manufacturing (DMR-2309083). XRD was performed at the Institute for Advanced Materials & Manufacturing (IAMM) Diffraction Facility, located at the University of Tennessee, Knoxville.

REFERENCES

[1] About the Critical Materials Institute | Ames Laboratory, (n.d.). https://www.ameslab.gov/cmi/about-critical-materials-institute (accessed June 9, 2022).

[2] AdNaNoTek Magnetron Sputtering Deposition, Sputter System | e Beam Evaporator | PLD | Pulsed Laser Deposition (n.d.). https://www.adnano-tek.com/magnetron-sputtering-deposition-msd.html (accessed June 8, 2022).

[3] S. Swann, Magnetron sputtering, Physics in Technology 19 (1988) 67–75. https://doi.org/10.1088/0305-4624/19/2/304.

[4] J.D. Fowlkes, J.M. Fitz-Gerald, P.D. Rack, Ultraviolet emitting (Y1−xGdx)2O3−δ thin films deposited by radio frequency magnetron sputtering: Combinatorial modeling, synthesis, and rapid characterization, Thin Solid Films 510 (2006) 68–76. https://doi.org/10.1016/j.tsf.2005.12.309.

[5] R. Collette, Y. Wu, P.D. Rack, Correlating the optical property evolution in the Au-Ni binary thin films: From metastable solid solution to phase separated alloy, Journal of Alloys and Compounds 793 (2019) 695–704. https://doi.org/10.1016/j.jallcom.2019.04.207.

[6] W.L. Boldman, D.A. Garfinkel, R. Collette, C.S. Jorgenson, D.K. Pradhan, D.A. Gilbert, P.D. Rack, Exploring the composition, phase separation and structure of AgFe alloys for magneto-optical applications, Materials Science and Engineering: B 266 (2021) 115044. https://doi.org/10.1016/j.mseb.2021.115044.

[7] Y. Wu, C. Liu, T.M. Moore, G.A. Magel, D.A. Garfinkel, J.P. Camden, M.G. Stanford, G. Duscher, P.D. Rack, Exploring Photothermal Pathways via in Situ Laser Heating in the Transmission Electron Microscope: Recrystallization, Grain Growth, Phase Separation, and Dewetting in Ag0.5Ni0.5 Thin Films, Microsc. Microanal. 24 (2018) 647–656. https://doi.org/10.1017/S1431927618015465.

[8] E.J. Sullivan, J.A. Tomko, J.M. Skelton, J.M. Fitz-Gerald, P.E. Hopkins, J.A. Floro, Lamellar instabilities during scanning laser melting of Al–Cu eutectic and hypoeutectic thin films, Journal of Alloys and Compounds 865 (2021) 158800. https://doi.org/10.1016/j.jallcom.2021.158800.

[9] M. Ohring, Film Thickness and Uniformity, in: Materials Science of Thin Films, 2nd ed., Academic Press, San Diego, 2002: pp. 106–115.

[10] D.A. Garfinkel, N. Tang, G. Pakeltis, R. Emery, I.N. Ivanov, D.A. Gilbert, P.D. Rack, Magnetic and Optical Properties of Au–Co Solid Solution and Phase-Separated Thin Films and Nanoparticles, ACS Applied Materials & Interfaces 14 (2022) 15047–15058. https://doi.org/10.1021/acsami.2c02028.

[11] T.C. Lu, J. Yang, Z. Suo, A.G. Evans, R. Hecht, R. Mehrabian, Matrix cracking in intermetallic composites caused by thermal expansion mismatch, Acta

Metallurgica et Materialia 39 (1991) 1883–1890. https://doi.org/10.1016/0956-7151(91)90157-V.
[12] M. Martena, D. Botto, P. Fino, S. Sabbadini, M.M. Gola, C. Badini, Modelling of TBC system failure: Stress distribution as a function of TGO thickness and thermal expansion mismatch, Engineering Failure Analysis 13 (2006) 409–426. https://doi.org/10.1016/j.engfailanal.2004.12.027.
[13] D. Klobčar, J. Tušek, B. Taljat, Thermal fatigue of materials for die-casting tooling, Materials Science and Engineering: A 472 (2008) 198–207. https://doi.org/10.1016/j.msea.2007.03.025.
[14] N.A. Roberts, G.A. Magel, C.D. Hartfield, T.M. Moore, J.D. Fowlkes, P.D. Rack, *In situ* laser processing in a scanning electron microscope, Journal of Vacuum Science & Technology A: Vacuum, Surfaces, and Films 30 (2012) 041404. https://doi.org/10.1116/1.4731254.
[15] A.V. Polijanczuk, D.G. Whitehead, Semiconductor lasers for microsoldering, in: IEE Colloquium on Advances in Interconnection Technology, 1991: p. 6/1-6/4.
[16] E. Kennedy, G. Byrne, D.N. Collins, A review of the use of high power diode lasers in surface hardening, Journal of Materials Processing Technology 155–156 (2004) 1855–1860. https://doi.org/10.1016/j.jmatprotec.2004.04.276.
[17] L. Li, The advances and characteristics of high-power diode laser materials processing, Optics and Lasers in Engineering 34 (2000) 231–253. https://doi.org/10.1016/S0143-8166(00)00066-X.
[18] D.J. Hwang, N. Misra, C.P. Grigoropoulos, A.M. Minor, S.S. Mao, *In situ* monitoring of material processing by a pulsed laser beam coupled via a lensed fiber into a scanning electron microscope, Journal of Vacuum Science & Technology A: Vacuum, Surfaces, and Films 26 (2008) 1432–1438. https://doi.org/10.1116/1.2987946.
[19] Jun. Funatsu, Laser assisted focused-ion-beam-induced deposition of copper, J. Vac. Sci. Technol. B 14 (1996) 179. https://doi.org/10.1116/1.589023.
[20] X.-D. Xiang, Combinatorial materials synthesis and screening: An integrated materials chip approach to discovery and optimization of functional materials, Annual Review of Materials Science 29 (1999) 149.
[21] R.W. Cahn, Rapid alloy assessment, Nature 410 (2001) 643–644. https://doi.org/10.1038/35070692.
[22] K. Kennedy, T. Stefansky, G. Davy, V.F. Zackay, E.R. Parker, Rapid Method for Determining Ternary-Alloy Phase Diagrams, Journal of Applied Physics 36 (1965) 3808–3810. https://doi.org/10.1063/1.1713952.
[23] J.J. Hanak, The “multiple-sample concept” in materials research: Synthesis, compositional analysis and testing of entire multicomponent systems, J Mater Sci 5 (1970) 964–971. https://doi.org/10.1007/BF00558177.

[24] S.A. Wilson, R.P.J. Jourdain, Q. Zhang, R.A. Dorey, C.R. Bowen, M. Willander, Q.U. Wahab, M. Willander, S.M. Al-hilli, O. Nur, E. Quandt, C. Johansson, E. Pagounis, M. Kohl, J. Matovic, B. Samel, W. van der Wijngaart, E.W.H. Jager, D. Carlsson, Z. Djinovic, M. Wegener, C. Moldovan, R. Iosub, E. Abad, M. Wendlandt, C. Rusu, K. Persson, New materials for micro-scale sensors and actuators, Materials Science and Engineering: R: Reports 56 (2007) 1–129. https://doi.org/10.1016/j.mser.2007.03.001.

[25] A. Ludwig, J. Cao, B. Dam, R. Gremaud, Opto-mechanical characterization of hydrogen storage properties of Mg–Ni thin film composition spreads, Applied Surface Science 254 (2007) 682–686. https://doi.org/10.1016/j.apsusc.2007.05.093.

[26] J. Jin, M. Prochaska, D. Rochefort, D.K. Kim, L. Zhuang, F.J. DiSalvo, R.B. van Dover, H.D. Abruña, A high-throughput search for direct methanol fuel cell anode electrocatalysts of type PtxBiyPbz, Applied Surface Science 254 (2007) 653–661. https://doi.org/10.1016/j.apsusc.2007.06.077.

[27] J.M. Gregoire, M.E. Tague, S. Cahen, S. Khan, H.D. Abruña, F.J. DiSalvo, R.B. van Dover, Improved Fuel Cell Oxidation Catalysis in $Pt_{1-x}Ta_{x}$, Chem. Mater. 22 (2010) 1080–1087. https://doi.org/10.1021/cm9020782.

[28] C.Y. Wang, Y.S. Meng, G. Ceder, Y. Li, Electrochemical Properties of Nanostructured Al1−xCux Alloys as Anode Materials for Rechargeable Lithium-Ion Batteries, Journal of The Electrochemical Society (n.d.) 9.

[29] S. Kyrsta, R. Cremer, D. Neuschütz, M. Laurenzis, P. Haring Bolivar, H. Kurz, Deposition and characterization of Ge–Sb–Te layers for applications in optical data storage, Applied Surface Science 179 (2001) 55–60. https://doi.org/10.1016/S0169-4332(01)00263-X.

[30] M. Laurenzis, A. Heinrici, P.H. Bolivar, H. Kurz, S. Krysta, J.M. Schneider, Composition spread analysis of phase change dynamics in GexSbyTe1−x−y films embedded in an optical multilayer stack, IEE Proceedings - Science, Measurement and Technology 151 (2004) 394–397. https://doi.org/10.1049/ip-smt:20041082.

[31] A.F. Murray, D. Bryan, D.A. Garfinkel, C.S. Jogensen, N. Tang, E.A. Lass, Y. Yang, P.D. Rack, T.G. Denes, D.A. Gilbert, Anti-microbial properties of a multi-component alloy, (n.d.) 24.

[32] M. Hans, P. Keuter, A. Saksena, J.A. Sälker, M. Momma, H. Springer, J. Nowak, D. Zander, D. Primetzhofer, J.M. Schneider, Opportunities of combinatorial thin film materials design for the sustainable development of magnesium-based alloys, Sci Rep 11 (2021) 17454. https://doi.org/10.1038/s41598-021-97036-6.

[33] T. Gebhardt, D. Music, T. Takahashi, J.M. Schneider, Combinatorial thin film materials science: From alloy discovery and optimization to alloy design, Thin Solid Films 520 (2012) 5491–5499. https://doi.org/10.1016/j.tsf.2012.04.062.

[34] M. Javidani, D. Larouche, Application of cast Al–Si alloys in internal combustion engine components, International Materials Reviews 59 (2014) 132–158. https://doi.org/10.1179/1743280413Y.0000000027.
[35] C.H. Olk, M. Lukitsch, D.B. Haddad, Combinatorial investigation of the mechanical properties of aluminum-silicon thin film nanocomposites, Journal of Materials Research 22 (2007) 1029–1036. https://doi.org/10.1557/jmr.2007.0139.
[36] C.H. Olk, D.B. Haddad, Characterization and control of microstructure in combinatorially prepared aluminum-silicon thin film nanocomposites, Journal of Materials Research 21 (2006) 1221–1228. https://doi.org/10.1557/jmr.2006.0164.
[37] S.M. Han, R. Shah, R. Banerjee, G.B. Viswanathan, B.M. Clemens, W.D. Nix, Combinatorial studies of mechanical properties of Ti–Al thin films using nanoindentation, Acta Materialia 53 (2005) 2059–2067. https://doi.org/10.1016/j.actamat.2005.01.017.
[38] R. Saha, W.D. Nix, Effects of the substrate on the determination of thin film mechanical properties by nanoindentation, Acta Materialia 50 (2002) 23–38. https://doi.org/10.1016/S1359-6454(01)00328-7.
[39] J.A. C. Santos, L. M. Rebêlo, A. C. Araujo, E. B. Barros, J.S. de Sousa, Thickness-corrected model for nanoindentation of thin films with conical indenters, Soft Matter 8 (2012) 4441–4448. https://doi.org/10.1039/C2SM07062F.
[40] Standard Test Method for Linear Thermal Expansion of Solid Materials by Thermomechanical Analysis, ASTM, n.d.
[41] Y. Shi, B. Yang, P.D. Rack, S. Guo, P.K. Liaw, Y. Zhao, High-throughput synthesis and corrosion behavior of sputter-deposited nanocrystalline Al (CoCrFeNi)100- combinatorial high-entropy alloys, Materials & Design 195 (2020) 109018. https://doi.org/10.1016/j.matdes.2020.109018.
[42] O.N. Senkov, J.D. Miller, D.B. Miracle, C. Woodward, Accelerated exploration of multi-principal element alloys with solid solution phases, Nat Commun 6 (2015) 6529. https://doi.org/10.1038/ncomms7529.
[43] J.D. James, J.A. Spittle, S.G.R. Brown, R.W. Evans, A review of measurement techniques for the thermal expansion coefficient of metals and alloys at elevated temperatures, Measurement Science and Technology 12 (2001) R1–R15. https://doi.org/10.1088/0957-0233/12/3/201.
[44] Standard Test Method for Linear Thermal Expansion of Solid Materials With a Push Rod Dilatometer, ASTM, n.d.
[45] C.L. Chen, R.C. Thomson, Study on thermal expansion of intermetallics in multicomponent Al–Si alloys by high temperature X-ray diffraction, Intermetallics 18 (2010) 1750–1757. https://doi.org/10.1016/j.intermet.2010.05.015.
[46] Y. Kuru, M. Wohlschlögel, U. Welzel, E.J. Mittemeijer, Coefficients of thermal expansion of thin metal films investigated by non-ambient X-ray diffraction stress

analysis, Surface and Coatings Technology 202 (2008) 2306–2309. https://doi.org/10.1016/j.surfcoat.2007.08.002.
[47] Y. Zoo, D. Adams, J.W. Mayer, T.L. Alford, Investigation of coefficient of thermal expansion of silver thin film on different substrates using X-ray diffraction, Thin Solid Films 513 (2006) 170–174. https://doi.org/10.1016/j.tsf.2006.02.005.
[48] G. Rodrigues, C.A. Nunes, P.A. Suzuki, G.C. Coelho, Thermal expansion of the Ti5Si3 and Ti6Si2B phases investigated by high-temperature X-ray diffraction, Intermetallics 14 (2006) 236–240. https://doi.org/10.1016/j.intermet.2005.05.007.
[49] L. Saturday, L. Wilson, S. Retterer, N.J. Evans, D. Briggs, P.D. Rack, N. Lavrik, Thermal conductivity of nano- and micro-crystalline diamond films studied by photothermal excitation of cantilever structures, Diamond and Related Materials 113 (2021) 108279. https://doi.org/10.1016/j.diamond.2021.108279.
[50] W. Fang, H.-C. Tsai, C.-Y. Lo, Determining thermal expansion coefficients of thin films using micromachined cantilevers, Sensors and Actuators A: Physical 77 (1999) 21–27. https://doi.org/10.1016/S0924-4247(99)00019-9.
[51] D. Grbovic, N.V. Lavrik, S. Rajic, P.G. Datskos, Arrays of SiO2 substrate-free micromechanical uncooled infrared and terahertz detectors, Journal of Applied Physics 104 (2008) 054508. https://doi.org/10.1063/1.2959574.
[52] W. Fang, C.-Y. Lo, On the thermal expansion coefficients of thin films, Sensors and Actuators A: Physical 84 (2000) 310–314. https://doi.org/10.1016/S0924-4247(00)00311-3.
[53] E.T. Stromme, H.B. Henderson, Z.C. Sims, M.S. Kesler, D. Weiss, R.T. Ott, F. Meng, S. Kassoumeh, J. Evangelista, G. Begley, O. Rios, Ageless Aluminum-Cerium-Based Alloys in High-Volume Die Casting for Improved Energy Efficiency, JOM 70 (2018) 866–871. https://doi.org/10.1007/s11837-018-2861-9.
[54] Z.C. Sims, O.R. Rios, D. Weiss, P.E.A. Turchi, A. Perron, J.R.I. Lee, T.T. Li, J.A. Hammons, M. Bagge-Hansen, T.M. Willey, K. An, Y. Chen, A.H. King, S.K. McCall, High performance aluminum–cerium alloys for high-temperature applications, Materials Horizons 4 (2017) 1070–1078. https://doi.org/10.1039/C7MH00391A.
[55] Z.C. Sims, D. Weiss, S.K. McCall, M.A. McGuire, R.T. Ott, T. Geer, O. Rios, P.A.E. Turchi, Cerium-Based, Intermetallic-Strengthened Aluminum Casting Alloy: High-Volume Co-product Development, JOM 68 (2016) 1940–1947. https://doi.org/10.1007/s11837-016-1943-9.
[56] J. Stroh, D. Sediako, D. Weiss, Development of Cerium-Reinforced Specialty Aluminum Alloy with Application of X-ray and Neutron Diffraction, Inter Metalcast 15 (2021) 29–39. https://doi.org/10.1007/s40962-020-00467-6.

[57] D. Weiss, High Performance Aluminum Casting Alloys for Engine Applications, SAE International, Warrendale, PA, 2016. https://doi.org/10.4271/2016-32-0019.
[58] M.A. Domínguez-Crespo, A.M. Torres-Huerta, S.E. Rodil, E. Ramírez-Meneses, G.G. Suárez-Velázquez, M.A. Hernández-Pérez, Effective corrosion protection of AA6061 aluminum alloy by sputtered Al–Ce coatings, Electrochimica Acta 55 (2009) 498–503. https://doi.org/10.1016/j.electacta.2009.09.002.
[59] M.A. Domínguez-Crespo, S.E. Rodil, A.M. Torres-Huerta, E. Ramírez-Meneses, G. Suárez-Velázquez, Structural and electrochemical performance of sputtered Al–Ce films on AA6061 aluminum alloy substrates, Surface and Coatings Technology 204 (2009) 571–579. https://doi.org/10.1016/j.surfcoat.2009.08.041.
[60] A.C. Crossland, G.E. Thompson, P. Skeldon, G.C. Wood, C.J.E. Smith, H. Habazaki, K. Shimizu, Anodic Oxidation of Al-Ce Alloys and Inhibitive Behaviour of Cerium Species, Corrosion Science 40 (1998) 871–885.
[61] E.R. Jette, F. Foote, Precision Determination of Lattice Constants, The Journal of Chemical Physics 3 (1935) 605–616. https://doi.org/10.1063/1.1749562.
[62] A.W. Lawson, T.-Y. Tang, Concerning the High Pressure Allotropic Modification of Cerium, Physical Review 76 (1949) 301–302. https://doi.org/10.1103/PhysRev.76.301.
[63] F. Czerwinski, Thermal stability of aluminum–cerium binary alloys containing the Al–Al11Ce3 eutectic, Materials Science and Engineering: A 809 (2021) 140973. https://doi.org/10.1016/j.msea.2021.140973.
[64] O. Kraft, W.D. Nix, Measurement of the lattice thermal expansion coefficients of thin metal films on substrates, Journal of Applied Physics 83 (1998) 3035–3038. https://doi.org/10.1063/1.367118.
[65] P. Staron, A. Stark, N. Schell, P. Spoerk-Erdely, H. Clemens, Thermal Expansion of a Multiphase Intermetallic Ti-Al-Nb-Mo Alloy Studied by High-Energy X-ray Diffraction, Materials 14 (2021) 727. https://doi.org/10.3390/ma14040727.
[66] Y. Wu, C. Liu, T.M. Moore, G.A. Magel, D.A. Garfinkel, J.P. Camden, M.G. Stanford, G. Duscher, P.D. Rack, Exploring Photothermal Pathways via *in Situ* Laser Heating in the Transmission Electron Microscope: Recrystallization, Grain Growth, Phase Separation, and Dewetting in $Ag_{0.5}Ni_{0.5}$ Thin Films, Microscopy and Microanalysis 24 (2018) 647–656. https://doi.org/10.1017/S1431927618015465.
[67] F. Czerwinski, B. Shalchi Amirkhiz, On the Al–Al11Ce3 Eutectic Transformation in Aluminum–Cerium Binary Alloys, Materials 13 (2020) 4549. https://doi.org/10.3390/ma13204549.
[68] D. Weiss, Castability and Characteristics of High Cerium Aluminum Alloys, InTech Open (2017). https://www.intechopen.com/chapters/58487 (accessed April 4, 2022).

[69] D.N. Lee, Textures and structures of vapor deposits, Journal of Materials Science 34 (1999) 2575–2582.
[70] J. Peltonen, M. Murtomaa, K. Robinson, J. Salonen, The electrical resistivity and relative permittivity of binary powder mixtures, Powder Technology 325 (2018) 228–233. https://doi.org/10.1016/j.powtec.2017.10.060.
[71] R.A. Serway, in: Principles of Physics, 2nd ed., Saunders College Pub., Fort Worth, Texas, 1998: p. 602.
[72] C. S. Garde, T. Takeuchi, Y. Nakano, Y. Takeda, Y. Ota, Y. Miyauchi, K. Sugiyama, M. Hagiwara, K. Kindo, F. Honda, R. Settai, Y. Ōnuki, Electrical and Magnetic Properties of R_3Al_{11} (R = La, Ce, Pr, and Nd), Journal of the Physical Society of Japan 77 (2008) 124704. https://doi.org/10.1143/JPSJ.77.124704.
[73] W. Fang, C.-Y. Lo, On the thermal expansion coefficients of thin films, Sensors and Actuators A: Physical 84 (2000) 310–314. https://doi.org/10.1016/S0924-4247(00)00311-3.
[74] A.J.C. Wilson, The thermal expansion of aluminium from 0 to 650 C, Proceedings of the Physical Society 53 (1941) 235–244. https://doi.org/10.1088/0959-5309/53/3/305.
[75] A. Reuss, Berechnung der Fließgrenze von Kristallen auf Grund der Plastizitätsbedingung für Einkristalle, Zeitschrift Für Angewandte Mathematik Und Mechanik 9 (1922) 49–58.
[76] W. Voigt, Theoretische Studien über die Elastizitätsverhältnisse der Krystalle, Annalen Der Physik 274 (1889) 573–587.
[77] M. Toda, N. Inomata, T. Ono, I. Voiculescu, Cantilever beam temperature sensors for biological applications, IEEJ Transactions on Electrical and Electronic Engineering 12 (2017) 153–160. https://doi.org/10.1002/tee.22360.
[78] E.A. Starke, J.T. Staley, Application of modern aluminum alloys to aircraft, Progress in Aerospace Sciences 32 (1996) 131–172. https://doi.org/10.1016/0376-0421(95)00004-6.
[79] F. Czerwinski, Thermal Stability of Aluminum Alloys, Materials 13 (2020) 3441. https://doi.org/10.3390/ma13153441.
[80] J.M. Boileau, C.A. Cloutier, L.A. Godlewski, P.A. Reeber-Symanksi, C. Wolverton, J.E. Allison, The Dimensional Stability of Cast 319 Aluminum, SAE Transactions 112 (2003) 385–395.
[81] F. Czerwinski, W. Kasprzak, D. Sediako, D. Emadi, S. Shaha, J. Friedman, D. Chen, High-temperature aluminum alloys for automotive powertrains; cast aluminum alloys were developed with high-temperature tensile and fatigue strengths to withstand elevated-temperature applications in modern engines, Advanced Materials & Processes 174 (2016) 16–21.

[82] E. Aghaie, J. Stroh, D. Sediako, A. Rashidi, A.S. Milani, Improving the mechanical properties of the B319 aluminum alloy by addition of cerium, Materials Science and Engineering: A 793 (2020) 139899. https://doi.org/10.1016/j.msea.2020.139899.
[83] Z.C. Sims, M.S. Kesler, H.B. Henderson, E. Castillo, T. Fishman, D. Weiss, P. Singleton, R. Eggert, S.K. McCall, O. Rios, How Cerium and Lanthanum as Coproducts Promote Stable Rare Earth Production and New Alloys, Journal of Sustainable Metallurgy 8 (2022) 1225–1234. https://doi.org/10.1007/s40831-022-00562-4.
[84] F. Czerwinski, Cerium in aluminum alloys, Journal of Materials Science 55 (2020) 24–72. https://doi.org/10.1007/s10853-019-03892-z.
[85] J. Gambogi, Rare Earths, US Geological Survey, 2022.
[86] O. Rios, H.B. Henderson, M.S. Kesler, B.A. Moyer, Z. Sims, D. Weiss, R. Ott, C. Anderson, H. Cui, Production of castable light rare earth rich light metal compositions from direct reduction processes, US20210355565A1, 2021.
[87] Emily K. Schnebele, Silicon in July 2022, U.S. Geological Survey, 2022.
[88] Silicon's 300% Surge Throws Another Price Shock at the World, Bloomberg.Com (2021). https://www.bloomberg.com/news/articles/2021-10-01/silicon-s-300-surge-throws-another-price-shock-at-the-world.
[89] T.G. Harvey, Cerium-based conversion coatings on aluminium alloys: a process review, Corrosion Engineering, Science and Technology 48 (2013) 248–269. https://doi.org/10.1179/1743278213Y.0000000089.
[90] A. Bahadur, Intermetallic phases in Al-Mn alloys, J Mater Sci 23 (1988) 48–54. https://doi.org/10.1007/BF01174033.
[91] R. Kainuma, S. Takahashi, K. Ishida, Thermoelastic martensite and shape memory effect in ductile Cu-Al-Mn alloys, Metall Mater Trans A 27 (1996) 2187–2195. https://doi.org/10.1007/BF02651873.
[92] A.J. Bradley, J. Thewlis, W.L. Bragg, The crystal structure of α-manganese, Proceedings of the Royal Society of London. Series A, Containing Papers of a Mathematical and Physical Character 115 (1927) 456–471. https://doi.org/10.1098/rspa.1927.0103.
[93] A. Shukla, A.D. Pelton, Thermodynamic Assessment of the Al-Mn and Mg-Al-Mn Systems, Journal of Phase Equilibria and Diffusion 30 (2009) 28–39. https://doi.org/10.1007/s11669-008-9426-5.
[94] H.W.L. Phillips, The constitution of alloys of aluminium with manganese silicon and iron, Journal of the Institute of Metals 69 (1942) 275–316.
[95] F.G. Coury, E.L. Pires, W. Wolf, F.H. Paes de Almeida, A.L. Costa e Silva, W.J. Botta, C.S. Kiminami, M.J. Kaufman, Insight into the complex ternary phase

behavior in Al-Mn-Ce alloys, Journal of Alloys and Compounds 727 (2017) 460–468. https://doi.org/10.1016/j.jallcom.2017.08.136.
[96] K.H.J. Buschow, J.H.N. Van Vucht, W.W. Van Den Hoogenhof, Note on the crystal structure of the ternary rare earth-3d transition metal compounds of the type RT4Al8, Journal of the Less Common Metals 50 (1976) 145–150. https://doi.org/10.1016/0022-5088(76)90261-7.
[97] F.G. Coury, C.S. Kiminami, W.J. Botta, C. Bolfarini, M.J. Kaufman, Design and production of Al-Mn-Ce alloys with tailored properties, Materials & Design 110 (2016) 436–448. https://doi.org/10.1016/j.matdes.2016.08.008.
[98] X. Li, W. Xia, H. Yan, J. Chen, X. Li, Improving strength and corrosion resistance of high Mg alloyed Al–Mg–Mn alloys through Ce addition, Corrosion Engineering, Science and Technology 55 (2020) 381–391. https://doi.org/10.1080/1478422X.2020.1735716.
[99] Y. Yang, S. Bahl, K. Sisco, M. Lance, D. Shin, A. Shyam, A. Plotkowski, R.R. Dehoff, Primary solidification of ternary compounds in Al-rich Al–Ce–Mn alloys, Journal of Alloys and Compounds 844 (2020) 156048. https://doi.org/10.1016/j.jallcom.2020.156048.
[100] F. Stadler, H. Antrekowitsch, W. Fragner, H. Kaufmann, P.J. Uggowitzer, Effect of main alloying elements on strength of Al–Si foundry alloys at elevated temperatures, International Journal of Cast Metals Research 25 (2012) 215–224. https://doi.org/10.1179/1743133612Y.0000000004.
[101] T. Koutsoukis, M.M. Makhlouf, Alternatives to the Al-Si Eutectic System in Aluminum Casting Alloys, International Journal of Metalcasting 10 (2016) 342–347. https://doi.org/10.1007/s40962-016-0042-6.
[102] N.A. Belov, A.N. Alabin, D.G. Eskin, Improving the properties of cold-rolled Al–6%Ni sheets by alloying and heat treatment, Scripta Materialia 50 (2004) 89–94. https://doi.org/10.1016/j.scriptamat.2003.09.033.
[103] C.S. Tiwary, S. Kashyap, D.H. Kim, K. Chattopadhyay, Al based ultra-fine eutectic with high room temperature plasticity and elevated temperature strength, Materials Science and Engineering: A 639 (2015) 359–369. https://doi.org/10.1016/j.msea.2015.05.024.
[104] Y. Fan, M.M. Makhlouf, The effect of introducing the Al–Ni eutectic composition into Al–Zr–V alloys on microstructure and tensile properties, Materials Science and Engineering: A 654 (2016) 228–235. https://doi.org/10.1016/j.msea.2015.12.044.
[105] H.-L. Chen, E. Doernberg, P. Svoboda, R. Schmid-Fetzer, Thermodynamics of the Al3Ni phase and revision of the Al–Ni system, Thermochimica Acta 512 (2011) 189–195. https://doi.org/10.1016/j.tca.2010.10.005.

[106] H. Wang, Z. Li, Z. Chen, B. Yang, Thermodynamic Optimization of the Ni-Al-Ce Ternary System, Journal of Phase Equilibria and Diffusion 37 (2016) 222–228. https://doi.org/10.1007/s11669-015-0447-6.
[107] L.S. Toropova, D.G. Eskin, M.L. Kharakterova, T.V. Dobatkina, Advanced Aluminum Alloys Containing Scandium: Structure and Properties, Routledge, 2017.
[108] O. Zarechnyuk, P. Kripyakevich, I. Kolobnev, E. Cherkashin, The quaternary compound Ce3 Mn Cu8 Al24 and its crystal structure, Izv. Akad. Nauk SSSR Neorg. Mater. 3 (1967) 182–183.
[109] R. Ferro, G. Zanicchi, R. Marazza, Aluminium-Cerium-Nickel, in: Ternary Alloys, Weinheim, Germany, 1991: pp. 86–90.
[110] N.A. Belov, E.S. Naumova, Prospects for preparation of structural casting eutectic alloys based on the Al-Ce-Ni system, METALLY-ROSSIISKAIA AKADEMIIA NAUK (1996) 146–152.
[111] N.A. Belov, E.A. Naumova, D.G. Eskin, Casting alloys of the Al–Ce–Ni system: microstructural approach to alloy design, Materials Science and Engineering: A 271 (1999) 134–142. https://doi.org/10.1016/S0921-5093(99)00343-3.
[112] D. Gout, E. Benbow, O. Gourdon, G.J. Miller, Crystallographic, electronic and magnetic studies of Ce4Ni6Al23: a new ternary intermetallic compound in the cerium–nickel–aluminum phase diagram, Journal of Solid State Chemistry 174 (2003) 471–481. https://doi.org/10.1016/S0022-4596(02)00167-6.
[113] C. Tang, Y. Du, H.H. Xu, W. Xiong, L.J. Zhang, F. Zheng, H.Y. Zhou, Experimental investigation of the Al–Ce–Ni system at 800°C, Intermetallics 16 (2008) 432–439. https://doi.org/10.1016/j.intermet.2007.12.003.
[114] C. Tang, Y. Du, H. Zhou, The phase equilibria of the Al–Ce–Ni system at 500°C, Journal of Alloys and Compounds 470 (2009) 222–227. https://doi.org/10.1016/j.jallcom.2008.03.034.
[115] C. Tang, Y. Du, J. Wang, H. Zhou, L. Zhang, F. Zheng, J. Lee, Q. Yao, Correlation between thermodynamics and glass forming ability in the Al–Ce–Ni system, Intermetallics 18 (2010) 900–906. https://doi.org/10.1016/j.intermet.2009.12.027.
[116] T. Wu, A. Plotkowski, A. Shyam, D.C. Dunand, Microstructure and creep properties of cast near-eutectic Al–Ce–Ni alloys, Materials Science and Engineering: A 833 (2022) 142551. https://doi.org/10.1016/j.msea.2021.142551.
[117] D. Gout, E. Benbow, O. Gourdon, G.J. Miller, Theoretical studies on cerium nickel aluminides: polar intermetallics with heavy fermion behavior, Journal of Solid State Chemistry 176 (2003) 538–548. https://doi.org/10.1016/S0022-4596(03)00301-3.

[118] Y. Fan, K. Huang, M.M. Makhlouf, Precipitation Strengthening in Al-Ni-Mn Alloys, Metallurgical and Materials Transactions A 46 (2015) 5830–5841. https://doi.org/10.1007/s11661-015-3119-6.
[119] J. Kozakevich, J. Stroh, V. Mallouhi, D. Sediako, D. Weiss, Interplay Between Cooling Rate, Microstructure, and Mechanical Properties of an Al-Ce-Ni-Mn Alloy, in: D. Eskin (Ed.), Light Metals 2022, Springer International Publishing Ag, Cham, 2022: pp. 83–91. https://doi.org/10.1007/978-3-030-92529-1_11.
[120] R.A. Michi, K. Sisco, S. Bahl, Y. Yang, J.D. Poplawsky, L.F. Allard, R.R. Dehoff, A. Plotkowski, A. Shyam, A creep-resistant additively manufactured Al-Ce-Ni-Mn alloy, Acta Materialia 227 (2022) 117699. https://doi.org/10.1016/j.actamat.2022.117699.
[121] R. Emery, O.R. Rios, M.J. Thompson, D. Weiss, P.D. Rack, Thin film combinatorial sputtering of Al-Ce alloys: Investigating the phase separation of as-deposited solid solutions and determining the coefficient of thermal expansion, Journal of Alloys and Compounds (2022) 165271. https://doi.org/10.1016/j.jallcom.2022.165271.
[122] M. Kiguchi, T. Yokoyama, D. Matsumura, H. Kondoh, O. Endo, T. Ohta, Surface structures and thermal vibrations of Ni and Cu thin films studied by extended x-ray-absorption fine structure, Phys. Rev. B 61 (2000) 14020–14027. https://doi.org/10.1103/PhysRevB.61.14020.
[123] T. Wu, D.C. Dunand, Microstructure and thermomechanical properties of Al11Ce3, Intermetallics 148 (2022) 107636. https://doi.org/10.1016/j.intermet.2022.107636.
[124] P.C. Canfield, T. Kong, U.S. Kaluarachchi, N.H. Jo, Use of frit-disc crucibles for routine and exploratory solution growth of single crystalline samples, Philosophical Magazine 96 (2016) 84–92. https://doi.org/10.1080/14786435.2015.1122248.
[125] A.R. Drews, Calibration of a High Temperature X-Ray Diffraction Stage by Differential Thermal Expansion, Advances in X-Ray Analysis 44 (2001) 44–49.
[126] N.E. Brown, S.M. Swapp, C.L. Bennett, A. Navrotsky, High-temperature X-ray diffraction: solutions to uncertainties in temperature and sample position, J Appl Crystallogr 26 (1993) 77–81. https://doi.org/10.1107/S002188989200877X.
[127] S.T. Misture, Large-volume atmosphere-controlled high-temperature x-ray diffraction furnace, Meas. Sci. Technol. 14 (2003) 1091. https://doi.org/10.1088/0957-0233/14/7/326.
[128] R.O. Simmons, Use of fcc Metals as Internal Temperature Standards in X-Ray Diffraction, Journal of Applied Physics 41 (2003) 2235–2240. https://doi.org/10.1063/1.1659193.

[129] E. Gati, U. Tutsch, A. Naji, M. Garst, S. Köhler, H. Schubert, T. Sasaki, M. Lang, Effects of Disorder on the Pressure-Induced Mott Transition in κ-(BEDT-TTF)2Cu[N(CN)2]Cl, Crystals 8 (2018) 38. https://doi.org/10.3390/cryst8010038.
[130] F.-S. Sun, C.-X. Cao, M.-G. Yan, S.-E. Kim, Yong-Tailee, Alloying mechanism of beta stabilizers in a TiAl alloy, Metallurgical and Materials Transactions A 32 (2001) 1573–1589. https://doi.org/10.1007/s11661-001-0136-4.
[131] G.N. Irving, J. Stringer, D.P. Whittle, Effect of the possible fcc stabilizers Mn, Fe, and Ni on the high-temperature oxidation of Co-Cr alloys, Oxidation of Metals 8 (1974) 393–407. https://doi.org/10.1007/BF00603389.
[132] Y. Yamamoto, M.L. Santella, C.T. Liu, N.D. Evans, P.J. Maziasz, M.P. Brady, Evaluation of Mn substitution for Ni in alumina-forming austenitic stainless steels, Materials Science and Engineering: A 524 (2009) 176–185. https://doi.org/10.1016/j.msea.2009.06.043.
[133] R.L. Klueh, P.J. Maziasz, E.H. Lee, Manganese as an austenite stabilizer in Fe-Cr-Mn-C steels, Materials Science and Engineering: A 102 (1988) 115–124. https://doi.org/10.1016/0025-5416(88)90539-3.
[134] M. Ikeda, M. Ueda, R. Matsunaga, M. Niinomi, Phase Constitution and Heat Treatment Behavior of Ti-7mass% Mn-Al Alloys, Materials Science Forum 654–656 (2010) 855–858. https://doi.org/10.4028/www.scientific.net/MSF.654-656.855.
[135] ThermoCalc AB, ThermoCalc 2023a, (2023).
[136] ASM International, ASM Alloy Phase Diagram Database, (2023).
[137] J.R. Kozakevich, J. Stroh, D. Sediako, D. Weiss, Solidification Kinetics of an Al-Ce Alloy with Additions of Ni and Mn, Metals 13 (2023) 955. https://doi.org/10.3390/met13050955.
[138] A.E. Perrin, R.A. Michi, D.N. Leonard, K.D. Sisco, A.J. Plotkowski, A. Shyam, J.D. Poplawsky, L.F. Allard, Y. Yang, Effect of Mn on eutectic phase equilibria in Al-rich Al-Ce-Ni alloys, Journal of Alloys and Compounds 965 (2023) 171455. https://doi.org/10.1016/j.jallcom.2023.171455.
[139] S. Eswarappa Prameela, T.M. Pollock, D. Raabe, M.A. Meyers, A. Aitkaliyeva, K.-L. Chintersingh, Z.C. Cordero, L. Graham-Brady, Materials for extreme environments, Nat Rev Mater 8 (2023) 81–88. https://doi.org/10.1038/s41578-022-00496-z.
[140] R.J. Hemley, G.W. Crabtree, M.V. Buchanan, Materials in extreme environments, Physics Today 62 (2009) 32–37. https://doi.org/10.1063/1.3265234.
[141] E.P. George, D. Raabe, R.O. Ritchie, High-entropy alloys, Nat Rev Mater 4 (2019) 515–534. https://doi.org/10.1038/s41578-019-0121-4.

[142] B. Cantor, I.T.H. Chang, P. Knight, A.J.B. Vincent, Microstructural development in equiatomic multicomponent alloys, Materials Science and Engineering: A 375–377 (2004) 213–218. https://doi.org/10.1016/j.msea.2003.10.257.
[143] O.N. Senkov, J.D. Miller, D.B. Miracle, C. Woodward, Accelerated exploration of multi-principal element alloys for structural applications, Calphad 50 (2015) 32–48. https://doi.org/10.1016/j.calphad.2015.04.009.
[144] O.N. Senkov, J.D. Miller, D.B. Miracle, C. Woodward, Accelerated exploration of multi-principal element alloys with solid solution phases, Nat Commun 6 (2015) 6529. https://doi.org/10.1038/ncomms7529.
[145] E.P. George, W.A. Curtin, C.C. Tasan, High entropy alloys: A focused review of mechanical properties and deformation mechanisms, Acta Materialia 188 (2020) 435–474. https://doi.org/10.1016/j.actamat.2019.12.015.
[146] O.N. Senkov, G.B. Wilks, D.B. Miracle, C.P. Chuang, P.K. Liaw, Refractory high-entropy alloys, Intermetallics 18 (2010) 1758–1765. https://doi.org/10.1016/j.intermet.2010.05.014.
[147] O.N. Senkov, S.V. Senkova, C. Woodward, D.B. Miracle, Low-density, refractory multi-principal element alloys of the Cr–Nb–Ti–V–Zr system: Microstructure and phase analysis, Acta Materialia 61 (2013) 1545–1557. https://doi.org/10.1016/j.actamat.2012.11.032.
[148] O.N. Senkov, G.B. Wilks, J.M. Scott, D.B. Miracle, Mechanical properties of Nb25Mo25Ta25W25 and V20Nb20Mo20Ta20W20 refractory high entropy alloys, Intermetallics 19 (2011) 698–706. https://doi.org/10.1016/j.intermet.2011.01.004.
[149] W. Xiong, A.X.Y. Guo, S. Zhan, C.-T. Liu, S.C. Cao, Refractory high-entropy alloys: A focused review of preparation methods and properties, Journal of Materials Science & Technology 142 (2023) 196–215. https://doi.org/10.1016/j.jmst.2022.08.046.
[150] W. Li, P. Liu, P.K. Liaw, Microstructures and properties of high-entropy alloy films and coatings: a review, Materials Research Letters 6 (2018) 199–229. https://doi.org/10.1080/21663831.2018.1434248.
[151] J. Lin, S. Ozan, Y. Li, D. Ping, X. Tong, G. Li, C. Wen, Novel Ti-Ta-Hf-Zr alloys with promising mechanical properties for prospective stent applications, Sci Rep 6 (2016) 37901. https://doi.org/10.1038/srep37901.
[152] L. Seenappa, H.C. Manjunatha, K.N. Sridhar, C. Hanumantharayappa, Gamma and X-ray radiation compatibility of Ti–Ta–Hf–Zr alloys used for coronary stent applications, NUCL SCI TECH 29 (2017) 3. https://doi.org/10.1007/s41365-017-0339-z.
[153] H. Huang, Y. Wu, J. He, H. Wang, X. Liu, K. An, W. Wu, Z. Lu, Phase-Transformation Ductilization of Brittle High-Entropy Alloys via Metastability

Engineering, Advanced Materials 29 (2017) 1701678. https://doi.org/10.1002/adma.201701678.
[154] M.F. Buchely, D.M. Field, D.C. Van Aken, Analysis of Hot- and Cold-Rolled Loads in Medium-Mn TRIP Steels, Metall Mater Trans B 50 (2019) 1180–1192. https://doi.org/10.1007/s11663-019-01566-4.
[155] S.T. Pisarik, D.C. Van Aken, Thermodynamic Driving Force of the γ → ε Transformation and Resulting MS Temperature in High-Mn Steels, Metall Mater Trans A 47 (2016) 1009–1018. https://doi.org/10.1007/s11661-015-3265-x.
[156] G. Frommeyer, U. Brüx, P. Neumann, Supra-Ductile and High-Strength Manganese-TRIP/TWIP Steels for High Energy Absorption Purposes, ISIJ Int. 43 (2003) 438–446. https://doi.org/10.2355/isijinternational.43.438.
[157] S. Vrtnik, P. Koželj, A. Meden, S. Maiti, W. Steurer, M. Feuerbacher, J. Dolinšek, Superconductivity in thermally annealed Ta-Nb-Hf-Zr-Ti high-entropy alloys, Journal of Alloys and Compounds 695 (2017) 3530–3540. https://doi.org/10.1016/j.jallcom.2016.11.417.
[158] M.C. Gao, B. Zhang, S. Yang, S.M. Guo, Senary Refractory High-Entropy Alloy HfNbTaTiVZr, Metall Mater Trans A 47 (2016) 3333–3345. https://doi.org/10.1007/s11661-015-3105-z.
[159] A. Ludwig, Discovery of new materials using combinatorial synthesis and high-throughput characterization of thin-film materials libraries combined with computational methods, Npj Computational Materials (2019) 7.
[160] R. Emery, O.R. Rios, E.A. Lass, C.S. Jorgensen, D.A. Gilbert, W.R. Meier, M.R. Koehler, P.D. Rack, Identification of low coefficient of thermal expansion in Al23Ce4Ni6 via combinatorial sputtering of Al-Ce-Ni-Mn thin films and upscaling to bulk materials, Journal of Alloys and Compounds 968 (2023) 172220. https://doi.org/10.1016/j.jallcom.2023.172220.
[161] R. Emery, O.R. Rios, M.J. Thompson, D. Weiss, P.D. Rack, Thin film combinatorial sputtering of Al-Ce alloys: Investigating the phase separation of as-deposited solid solutions and determining the coefficient of thermal expansion, Journal of Alloys and Compounds 913 (2022) 165271. https://doi.org/10.1016/j.jallcom.2022.165271.
[162] Z. Wen, Y. Wang, J. Ling, W. Chen, L. Zhang, Y. Du, High-throughput determination of the composition-dependent mechanical and diffusion properties in β Ti–Nb–Zr–Hf refractory alloys, Journal of Alloys and Compounds 876 (2021) 160150. https://doi.org/10.1016/j.jallcom.2021.160150.
[163] J. Sakurai, H. Kozako, N. Mukai, Y. Ohnuma, T. Takahashi, S. Hata, Combinatorial Search for Ni–Nb–Ti Thin Film Amorphous Alloys with High Corrosion Resistances, Jpn. J. Appl. Phys. 50 (2011) 087201. https://doi.org/10.1143/JJAP.50.087201.

[164] S. Zak, C.O.W. Trost, P. Kreiml, M.J. Cordill, Accurate measurement of thin film mechanical properties using nanoindentation, Journal of Materials Research 37 (2022) 1373–1389. https://doi.org/10.1557/s43578-022-00541-1.
[165] S. Alvi, D.M. Jarzabek, M.G. Kohan, D. Hedman, P. Jenczyk, M.M. Natile, A. Vomiero, F. Akhtar, Synthesis and Mechanical Characterization of a CuMoTaWV High-Entropy Film by Magnetron Sputtering, ACS Appl. Mater. Interfaces 12 (2020) 21070–21079. https://doi.org/10.1021/acsami.0c02156.
[166] B. Song, Y. Li, Z. Cong, Y. Li, Z. Song, J. Chen, Effects of deposition temperature on the nanomechanical properties of refractory high entropy TaNbHfZr films, Journal of Alloys and Compounds 797 (2019) 1025–1030. https://doi.org/10.1016/j.jallcom.2019.05.121.
[167] S.K. Bachani, C.-J. Wang, B.-S. Lou, L.-C. Chang, J.-W. Lee, Microstructural characterization, mechanical property and corrosion behavior of VNbMoTaWAl refractory high entropy alloy coatings: Effect of Al content, Surface and Coatings Technology 403 (2020) 126351. https://doi.org/10.1016/j.surfcoat.2020.126351.
[168] Y.-G. Jung, B.R. Lawn, M. Martyniuk, H. Huang, X.Z. Hu, Evaluation of elastic modulus and hardness of thin films by nanoindentation, Journal of Materials Research 19 (2004) 3076–3080. https://doi.org/10.1557/JMR.2004.0380.
[169] C. Cheng, X. Zhang, M.J.R. Haché, Y. Zou, Magnetron co-sputtering synthesis and nanoindentation studies of nanocrystalline (TiZrHf)x(NbTa)1−x high-entropy alloy thin films, Nano Res. 15 (2022) 4873–4879. https://doi.org/10.1007/s12274-021-3805-1.
[170] W.C. Oliver, G.M. Pharr, Nanoindentation in materials research: Past, present, and future, MRS Bull. 35 (2010) 897–907. https://doi.org/10.1557/mrs2010.717.
[171] M.F. Doerner, W.D. Nix, A method for interpreting the data from depth-sensing indentation instruments, Journal of Materials Research 1 (1986) 601–609. https://doi.org/10.1557/JMR.1986.0601.
[172] J.L. Loubet, J.M. Georges, O. Marchesini, G. Meille, Vickers Indentation Curves of Magnesium Oxide (MgO), Journal of Tribology 106 (1984) 43–48. https://doi.org/10.1115/1.3260865.
[173] I.N. Sneddon, The relation between load and penetration in the axisymmetric boussinesq problem for a punch of arbitrary profile, International Journal of Engineering Science 3 (1965) 47–57. https://doi.org/10.1016/0020-7225(65)90019-4.
[174] W.C. Oliver, G.M. Pharr, An improved technique for determining hardness and elastic modulus using load and displacement sensing indentation experiments, Journal of Materials Research 7 (1992) 1564–1583. https://doi.org/10.1557/JMR.1992.1564.

[175] W.D. Nix, Mechanical properties of thin films, Metall Trans A 20 (1989) 2217–2245. https://doi.org/10.1007/BF02666659.
[176] D.L. Joslin, W.C. Oliver, A new method for analyzing data from continuous depth-sensing microindentation tests, Journal of Materials Research 5 (1990) 123–126. https://doi.org/10.1557/JMR.1990.0123.
[177] R.B. King, Elastic analysis of some punch problems for a layered medium, International Journal of Solids and Structures 23 (1987) 1657–1664. https://doi.org/10.1016/0020-7683(87)90116-8.
[178] R. Saha, W.D. Nix, Effects of the substrate on the determination of thin film mechanical properties by nanoindentation, Acta Materialia 50 (2002) 23–38. https://doi.org/10.1016/S1359-6454(01)00328-7.
[179] J. Chen, X. Zhou, W. Wang, B. Liu, Y. Lv, W. Yang, D. Xu, Y. Liu, A review on fundamental of high entropy alloys with promising high–temperature properties, Journal of Alloys and Compounds 760 (2018) 15–30. https://doi.org/10.1016/j.jallcom.2018.05.067.
[180] B.X. Cao, T. Yang, L. Fan, J.H. Luan, Z.B. Jiao, C.T. Liu, Refractory alloying additions on the thermal stability and mechanical properties of high-entropy alloys, Materials Science and Engineering: A 797 (2020) 140020. https://doi.org/10.1016/j.msea.2020.140020.
[181] M. Vaidya, K. Guruvidyathri, B.S. Murty, Phase formation and thermal stability of CoCrFeNi and CoCrFeMnNi equiatomic high entropy alloys, Journal of Alloys and Compounds 774 (2019) 856–864. https://doi.org/10.1016/j.jallcom.2018.09.342.
[182] W.C. Oliver, G.M. Pharr, Measurement of hardness and elastic modulus by instrumented indentation: Advances in understanding and refinements to methodology, Journal of Materials Research 19 (2004) 3–20. https://doi.org/10.1557/jmr.2004.19.1.3.
[183] G. Abadias, J.J. Colin, D. Tingaud, Ph. Djemia, L. Belliard, C. Tromas, Elastic properties of α- and β-tantalum thin films, Thin Solid Films 688 (2019) 137403. https://doi.org/10.1016/j.tsf.2019.06.053.
[184] M. Zhang, B. Yang, J. Chu, T.G. Nieh, Hardness enhancement in nanocrystalline tantalum thin films, Scripta Materialia 54 (2006) 1227–1230. https://doi.org/10.1016/j.scriptamat.2005.12.027.
[185] S. Shiri, C. Zhang, A. Odeshi, Q. Yang, Growth and characterization of tantalum multilayer thin films on CoCrMo alloy for orthopedic implant applications, Thin Solid Films 645 (2018) 405–408. https://doi.org/10.1016/j.tsf.2017.11.017.
[186] J.M.E. Harper, K.P. Rodbell, E.G. Colgan, R.H. Hammond, Control of in-plane texture of body centered cubic metal thin films, Journal of Applied Physics 82 (1997) 4319–4326. https://doi.org/10.1063/1.366239.

[187] R. Krishnan, M. Riley, S. Lee, T.-M. Lu, Formation of biaxially textured molybdenum thin films under the influence of recrystallization conditions, Thin Solid Films 519 (2011) 5429–5432. https://doi.org/10.1016/j.tsf.2011.02.048.
[188] M. Červená, R. Čerstvý, T. Dvořák, J. Rezek, P. Zeman, Metastable structures in magnetron sputtered W–Zr thin-film alloys, Journal of Alloys and Compounds 888 (2021) 161558. https://doi.org/10.1016/j.jallcom.2021.161558.
[189] S. Fritze, C.M. Koller, L. von Fieandt, P. Malinovskis, K. Johansson, E. Lewin, P.H. Mayrhofer, U. Jansson, Influence of Deposition Temperature on the Phase Evolution of HfNbTiVZr High-Entropy Thin Films, Materials 12 (2019) 587. https://doi.org/10.3390/ma12040587.
[190] S. Achache, S. Lamri, A. Alhussein, A. Billard, M. François, F. Sanchette, Gum Metal thin films obtained by magnetron sputtering of a Ti-Nb-Zr-Ta target, Materials Science and Engineering: A 673 (2016) 492–502. https://doi.org/10.1016/j.msea.2016.07.096.
[191] G.B. Thompson, R. Banerjee, S.A. Dregia, M.K. Miller, H.L. Fraser, A Comparison of Pseudomorphic Bcc Phase Stability in Zr/Nb and Ti/Nb Thin Film Multilayers, Journal of Materials Research 19 (2004) 707–715. https://doi.org/10.1557/jmr.2004.19.3.707.
[192] G.B. Thompson, R. Banerjee, S.A. Dregia, H.L. Fraser, Phase stability of bcc Zr in Nb/Zr thin film multilayers, Acta Materialia 51 (2003) 5285–5294. https://doi.org/10.1016/S1359-6454(03)00380-X.
[193] J. Kong, H. Shen, B. Chen, Z. Li, W. Shi, W. Yao, Zh. Qi, The abnormal structure of nanocrystalline titanium films prepared by d.c. sputtering, Thin Solid Films 207 (1992) 51–53. https://doi.org/10.1016/0040-6090(92)90100-P.
[194] M. Zhang, Y.F. Zhang, P.D. Rack, M.K. Miller, T.G. Nieh, Nanocrystalline tetragonal tantalum thin films, Scripta Materialia 57 (2007) 1032–1035. https://doi.org/10.1016/j.scriptamat.2007.07.041.
[195] J.J. Colin, G. Abadias, A. Michel, C. Jaouen, On the origin of the metastable β-Ta phase stabilization in tantalum sputtered thin films, Acta Materialia 126 (2017) 481–493. https://doi.org/10.1016/j.actamat.2016.12.030.
[196] R. Bansal, N. Behera, A. Kumar, P.K. Muduli, Crystalline phase dependent spin current efficiency in sputtered Ta thin films, Applied Physics Letters 110 (2017) 202402. https://doi.org/10.1063/1.4983677.
[197] R.B. Marcus, S. Quigley, Formation of f.c.c., b.c.c. and β-tantalum films by evaporation, Thin Solid Films 2 (1968) 467–477. https://doi.org/10.1016/0040-6090(68)90060-6.
[198] Z.H. Cao, P.Y. Li, X.K. Meng, Nanoindentation creep behaviors of amorphous, tetragonal, and bcc Ta films, Materials Science and Engineering: A 516 (2009) 253–258. https://doi.org/10.1016/j.msea.2009.03.019.

[199] S. Sinha, R.A. Mirshams, T. Wang, S.S. Nene, M. Frank, K. Liu, R.S. Mishra, Nanoindentation behavior of high entropy alloys with transformation-induced plasticity, Sci Rep 9 (2019) 6639. https://doi.org/10.1038/s41598-019-43174-x.
[200] A. Vemulapally, R. Kali, T.K. Bhandakkar, A. Mukhopadhyay, Transformation Plasticity Provides Insights into Concurrent Phase Transformation and Stress Relaxation Observed during Electrochemical Li Alloying of Sn Thin Film, J. Phys. Chem. C 122 (2018) 16561–16573. https://doi.org/10.1021/acs.jpcc.8b04065.
[201] F. Siska, J. Cech, P. Hausild, H. Hadraba, Z. Chlup, R. Husak, L. Stratil, Twinning in CoCrFeNiMn high entropy alloy induced by nanoindentation, Materials Science and Engineering: A 784 (2020) 139297. https://doi.org/10.1016/j.msea.2020.139297.
[202] N. Wang, Q. Cao, X. Wang, S. Ding, D. Zhang, J.-Z. Jiang, Unusual deformation-induced martensitic transformation in Fe-Co-Ni-Cr-Mn high entropy alloy thin films, Journal of Alloys and Compounds 920 (2022) 165959. https://doi.org/10.1016/j.jallcom.2022.165959.

APPENDIX

Supplemental Information

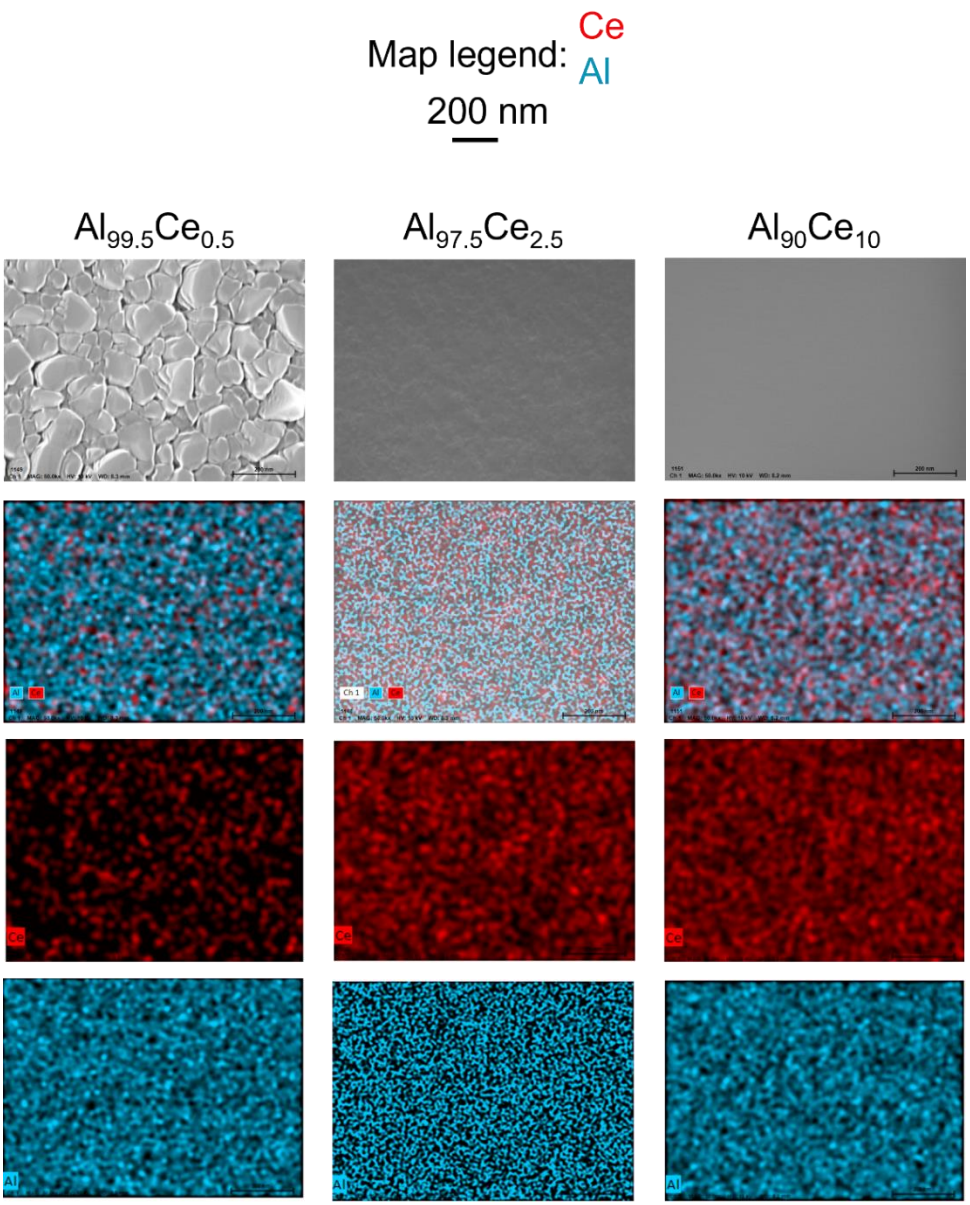

Figure 35. EDS maps for as-deposited compositions: $Al_{99.5}Ce_{0.5}$, $Al_{97.5}Ce_{2.5}$, $Al_{90}Ce_{10}$ showing homogeneous distribution of Al and Ce

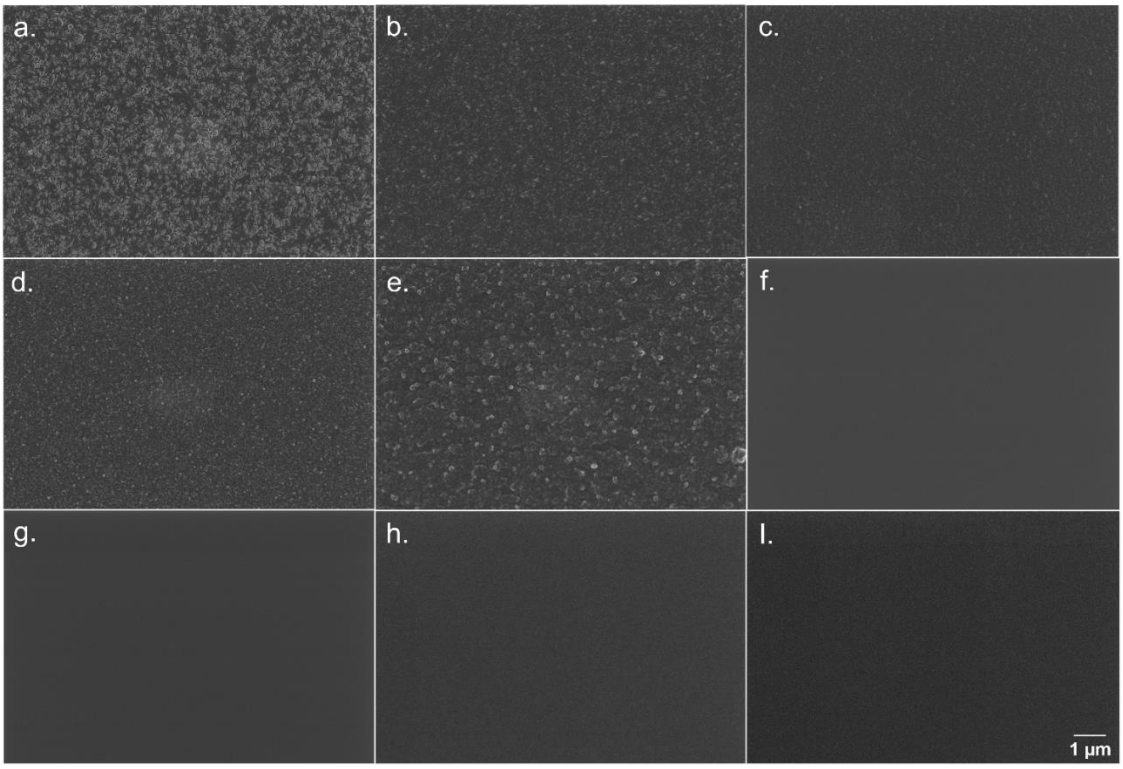

Figure 36. Plane view SEM images of the as-deposited films where (a) $Al_{99.5}Ce_{0.5}$, (b) $Al_{99.0}Ce_{1.0}$, (c) $Al_{98.5}Ce_{1.5}$, (d) $Al_{97.0}Ce_{3.0}$, (e) $Al_{95.5}Ce_{4.5}$, (f) $Al_{92.5}Ce_{7.5}$, (g) $Al_{89.5}Ce_{10.5}$, (h) $Al_{85.0}Ce_{15.0}$, and (i) $Al_{80.0}Ce_{20.0}$.

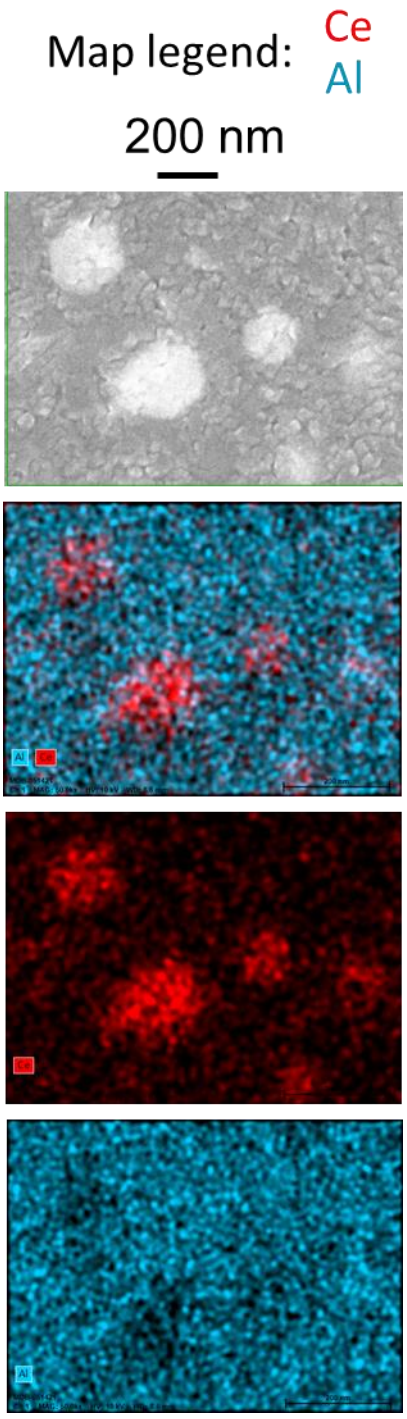

Figure 37. EDS maps for annealed $Al_{97.5}Ce_{2.5}$ showing phase separation.

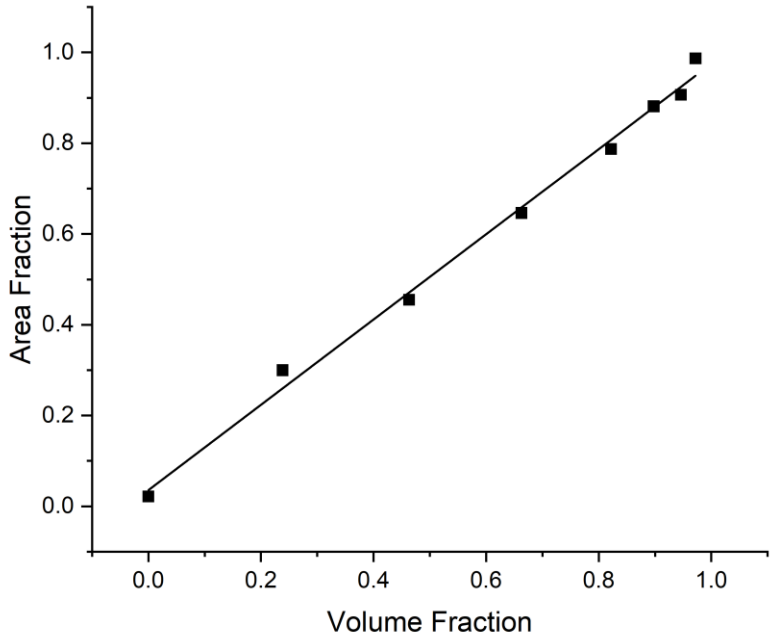

Figure 38. Comparison of area fraction determined from image analysis of SEM micrographs in figure 3 and calculated volume fraction using the lever rule on the equilibrium phase diagram.

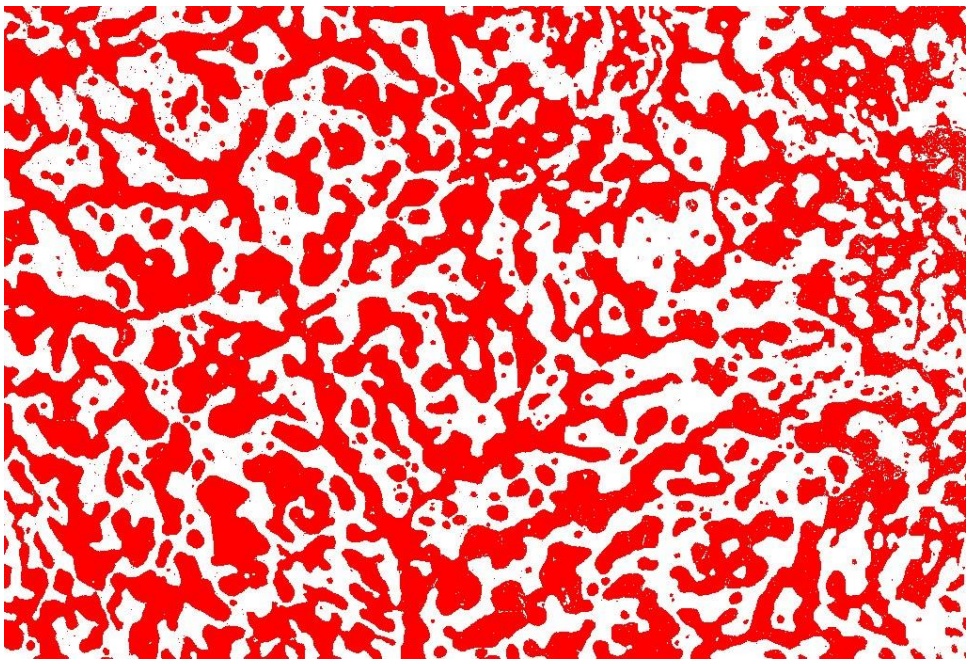

Figure 39. Example of thresholding performed on SEM micrographs in figure 3 via ImageJ thresholding functionality. This is the $Al_{92.5}Ce_{7.5}$ composition and shows 45.5% Al phase and 54.5 $Al_{11}Ce_3$ phase.

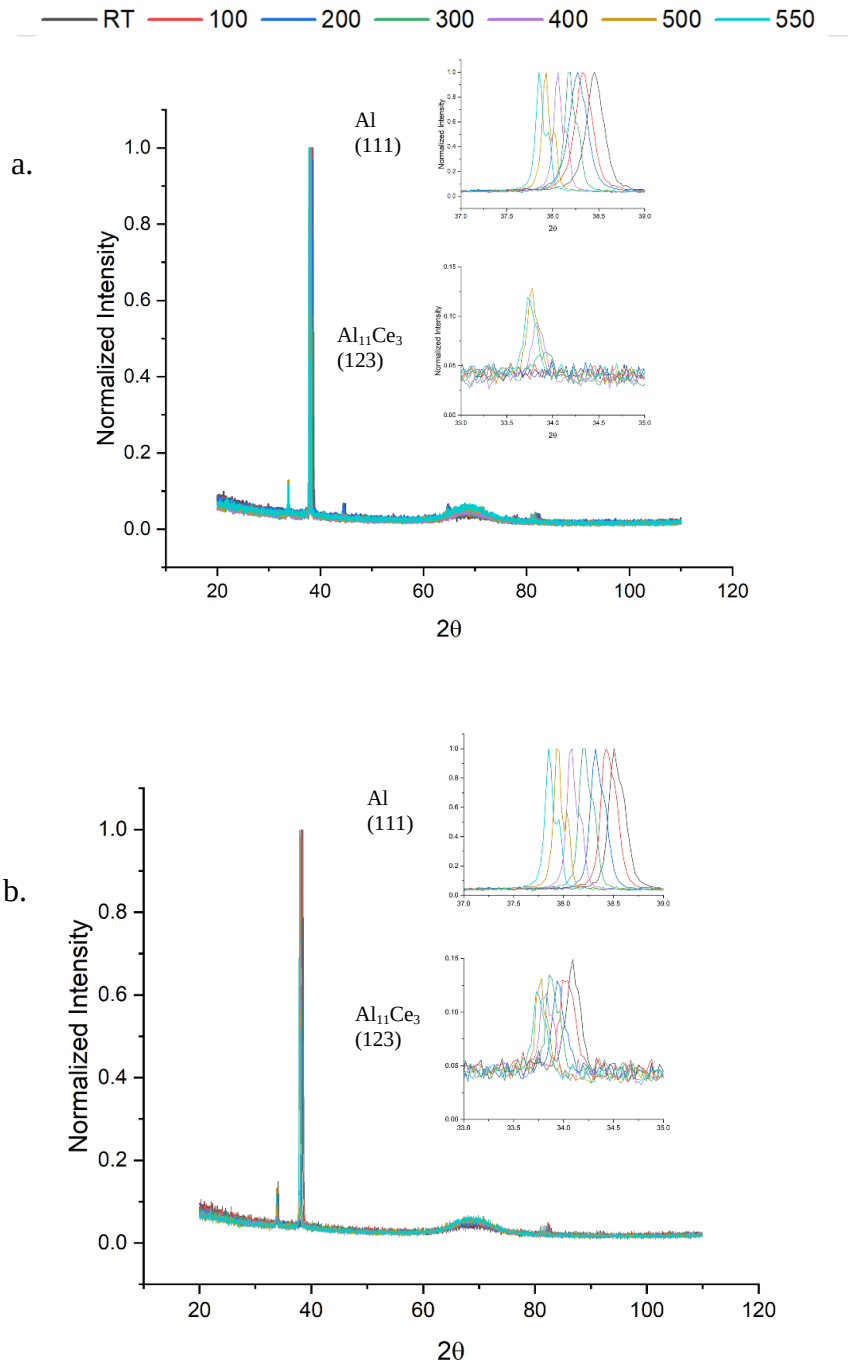

Figure 40. XRD results of the $Al_{99.5}Ce_{0.5}$ composition for (a) the heating cycle from room temperature to 550°C, and (b) the cooling cycle from 550°C back to room temperature. Inset are the normalized Al (111) peaks, and the $Al_{11}Ce_3$ (123) intermetallic peaks.

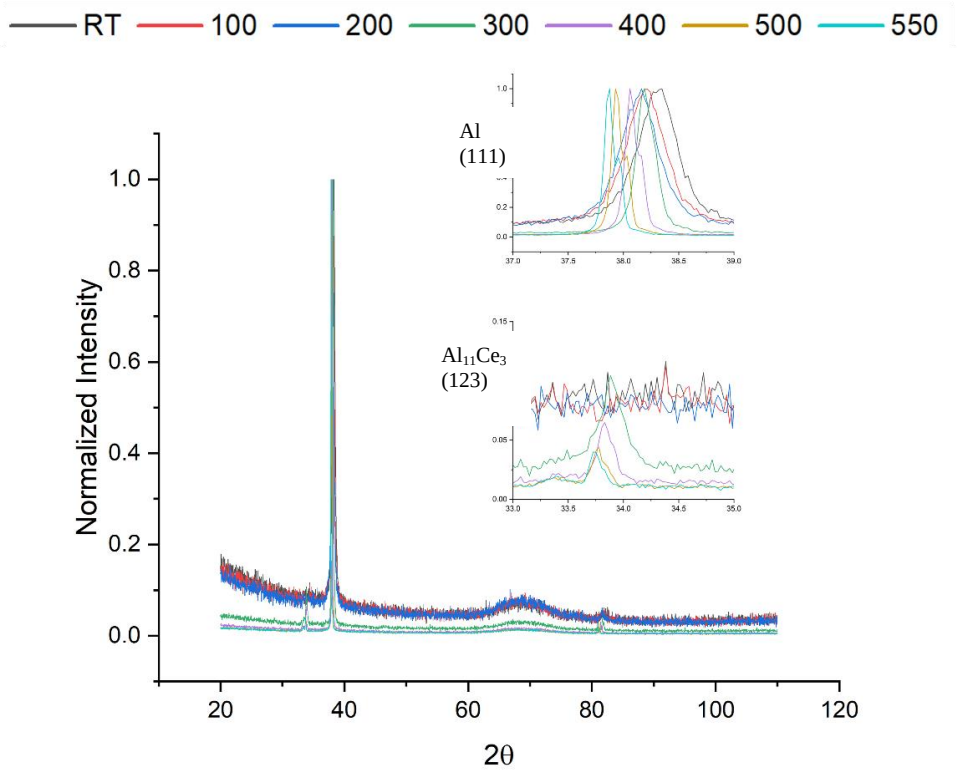

Figure 41. XRD results of the pre-annealed $Al_{92.5}Ce_{7.5}$ composition for the heating cycle from room temperature to 550°C. Inset are the normalized Al (111) peaks, and the $Al_{11}Ce_3$ (123) intermetallic peaks.

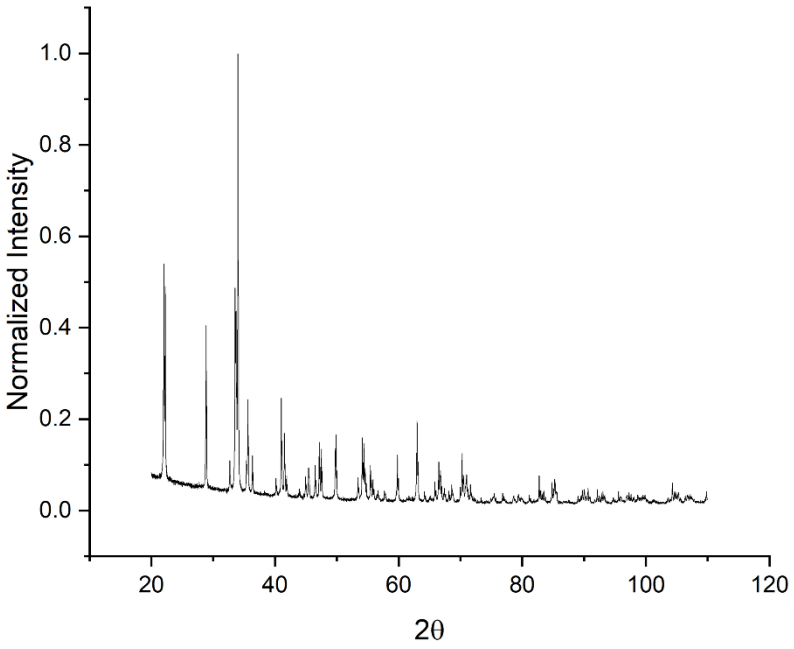

Figure 42. XRD results for the bulk $Al_{11}Ce_3$ phase

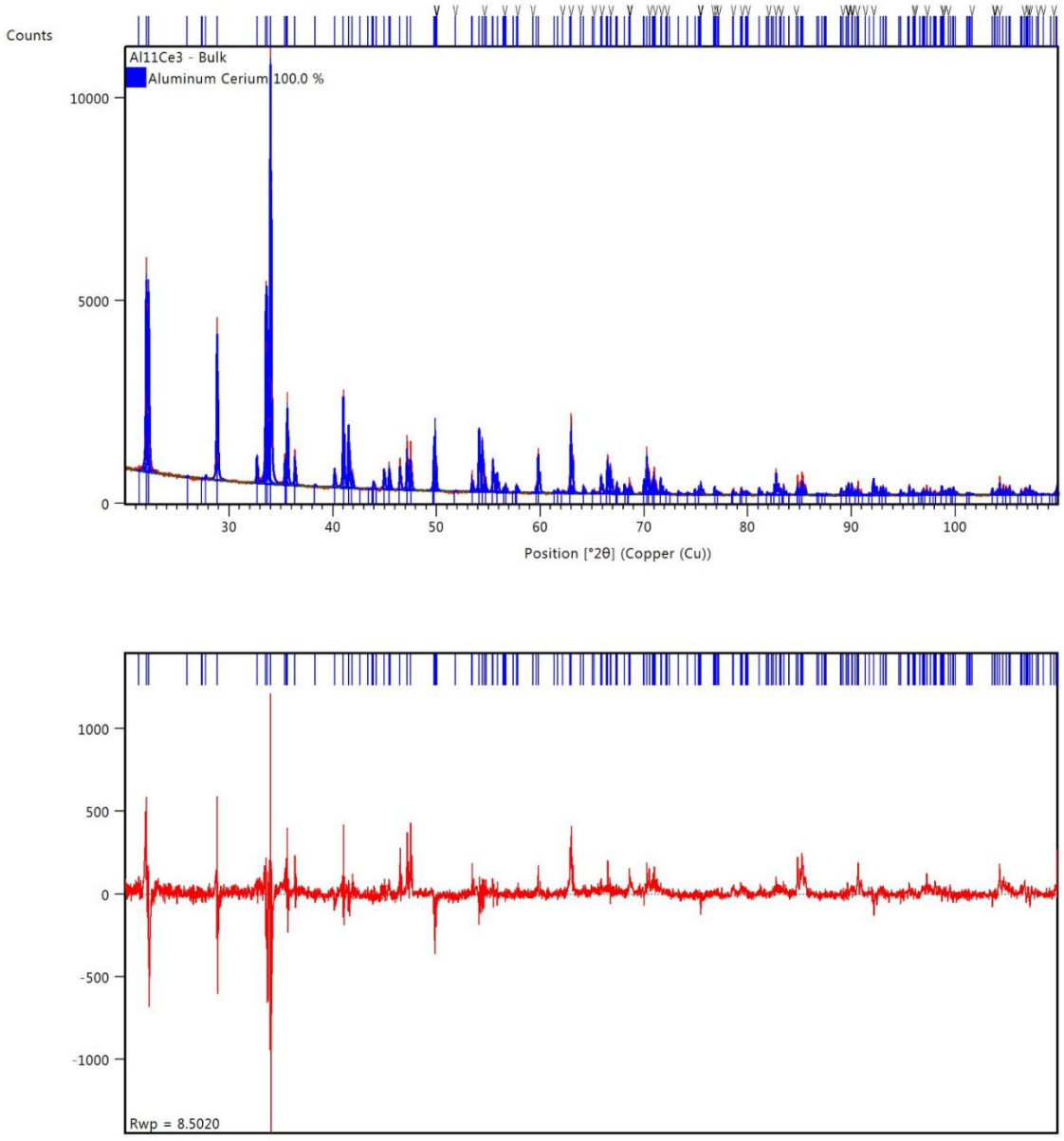

Figure 43. Expanded Rietveld analysis that accounts for preferred orientation performed on the bulk $Al_{11}Ce_3$ sample (compared to reference code 04-001-3600 with a score of 92)

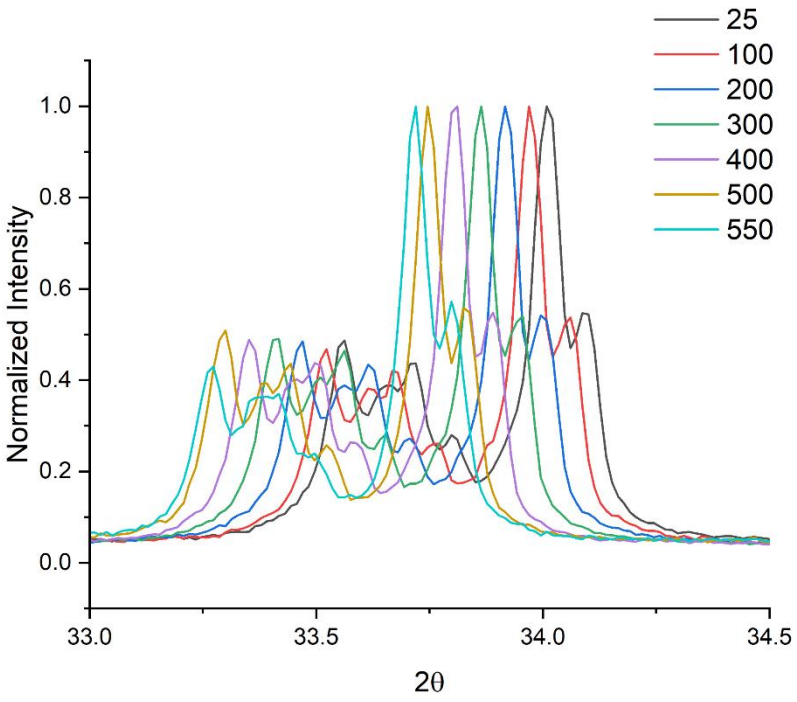

Figure 44. HTXRD results of the (123) plane from the bulk $Al_{11}Ce_3$ phase showing the peak shifts from room temperature 25°C to 550°C

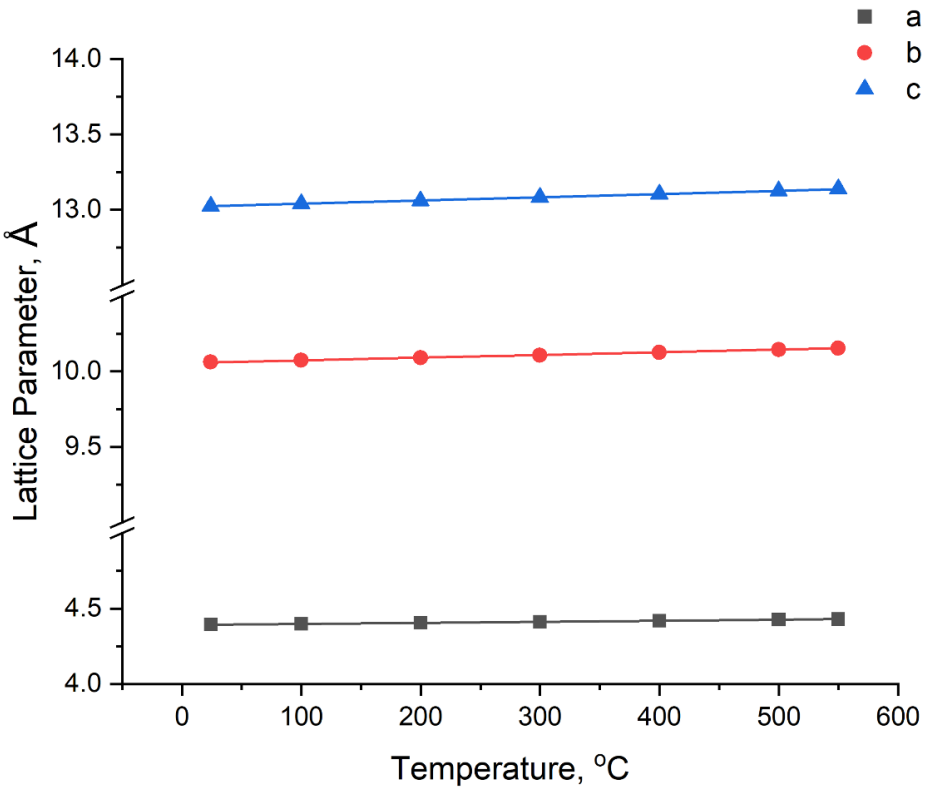

Figure 45. Refined lattice parameter values from the pure $Al_{11}Ce_3$ bulk sample with respect to temperature

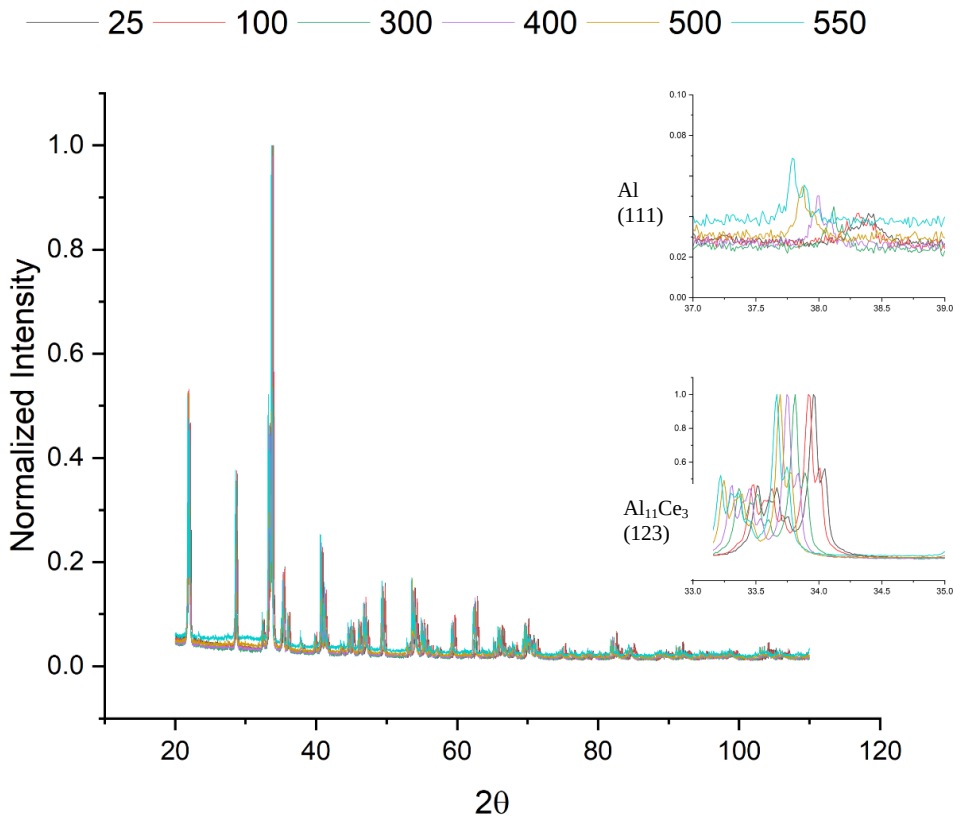

Figure 46. HTXRD results for the $Al_{11}Ce_3$ (minus 1 wt.% Ce) composition with Al (111) and $Al_{11}Ce_3$ (123) insets for room temperature to 550°C

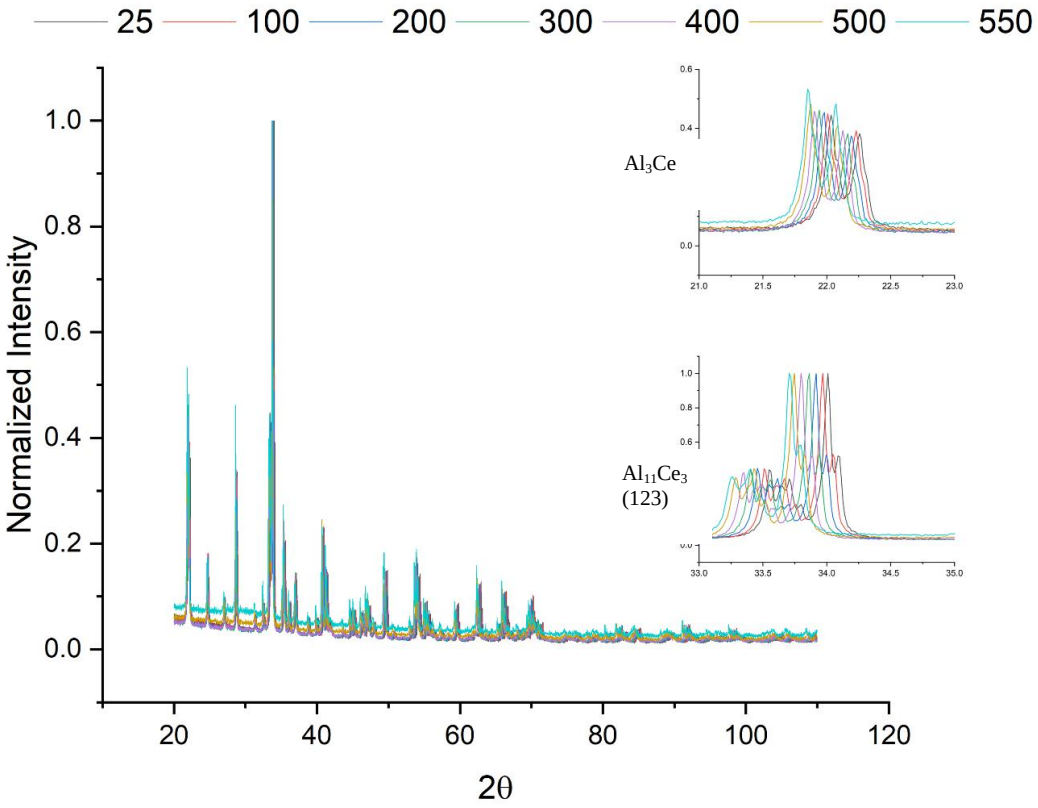

Figure 47. HTXRD results for the $Al_{11}Ce_3$ (plus 1 wt.% Ce) composition with Al_3Ce and $Al_{11}Ce_3$ (123) insets for room temperature to 550°C

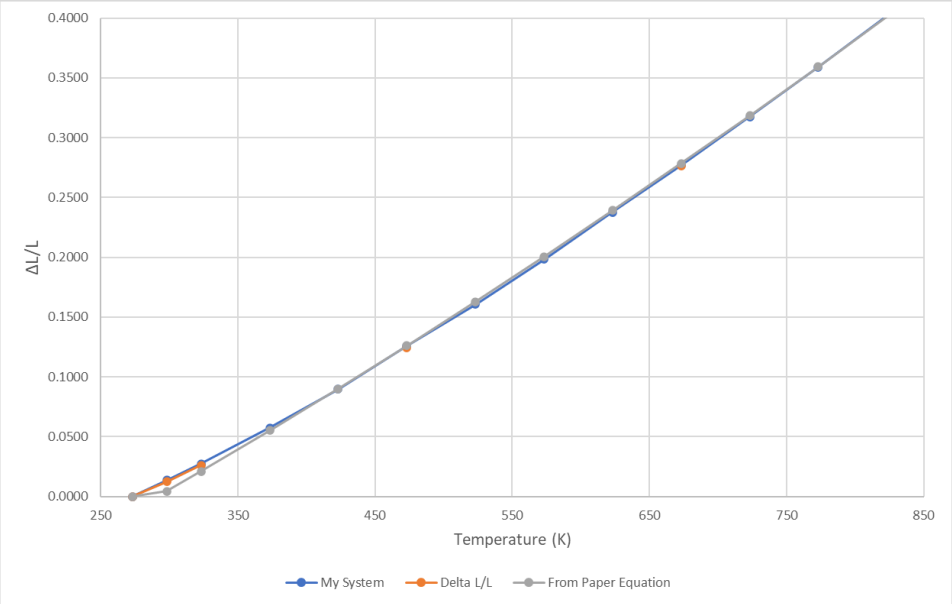

Figure 48. Calibration of high temperature XRD stage using alumina as a standard

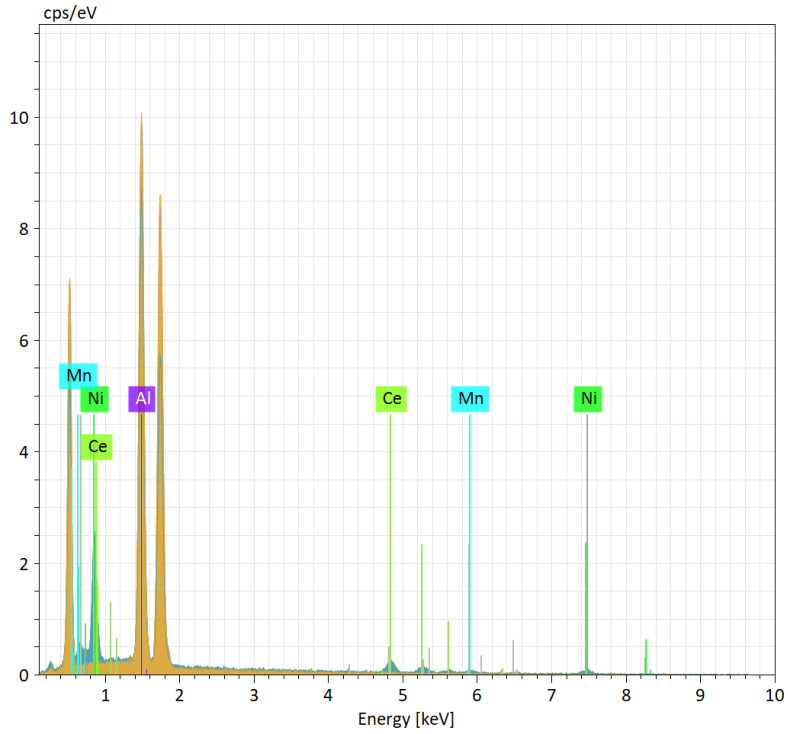

Figure 49. Sample EDXS spectrum for the quaternary thin film.

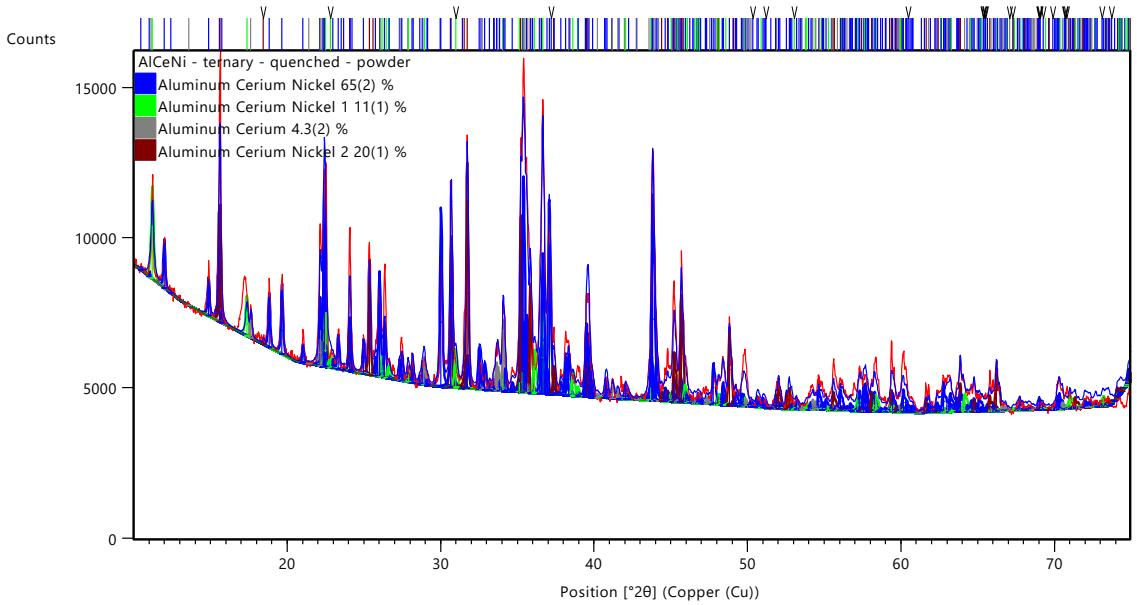

Figure 50. Sample Rietveld refinement on the annealed and quenched $Al_{23}Ce_4Ni_6$ stoichiometric casting.

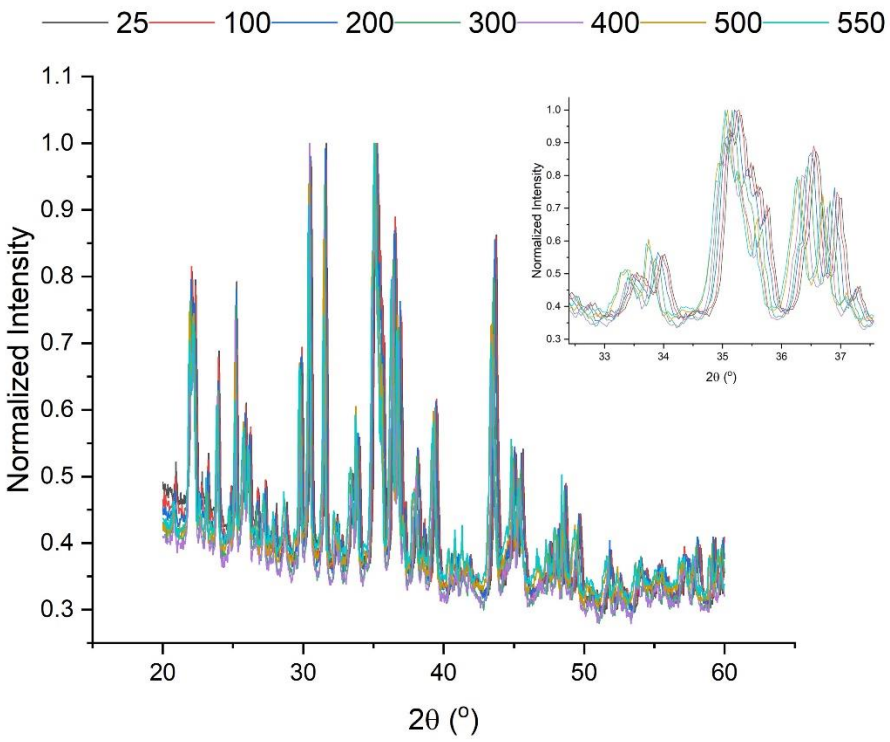

Figure 51. Overlayed TDXRD plot for single crystal $Al_{23}Ce_4Ni_6$ with inset to highlight minimal peak shifts

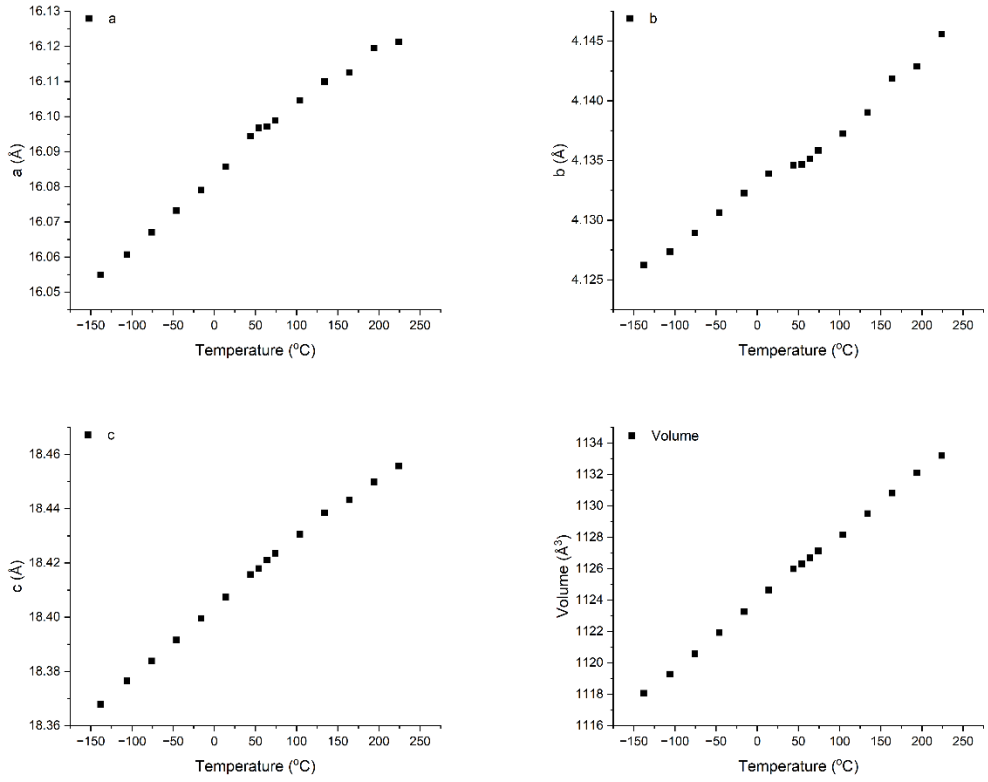

Figure 52. Temperature dependent lattice parameters and volume for the $Al_{23}Ce_4Ni_6$ phase from the powderized single crystal neutron data

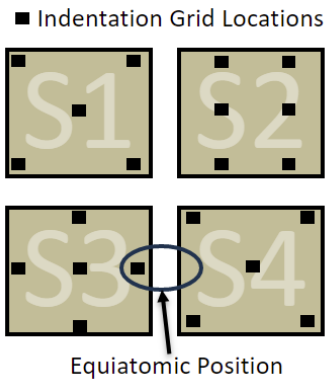

Figure 53. Relative indentation locations for each square along with the equiatomic composition location

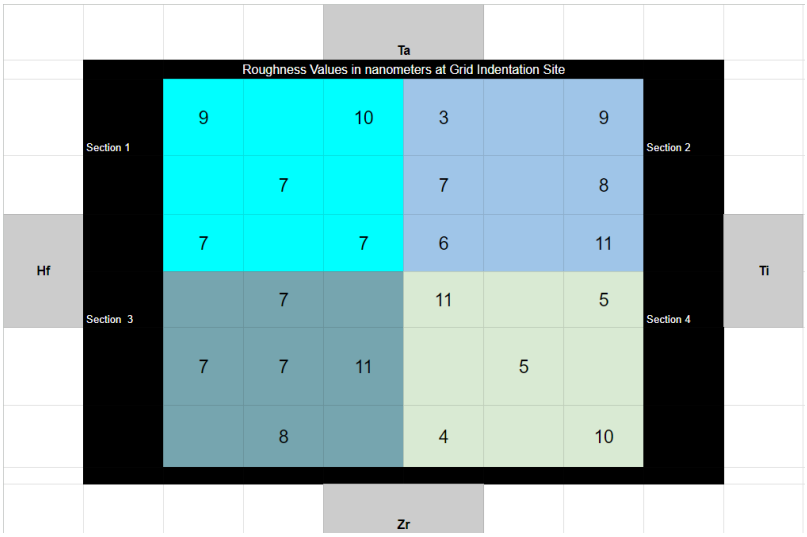

Figure 54. Relative surface roughness values for each square tested.

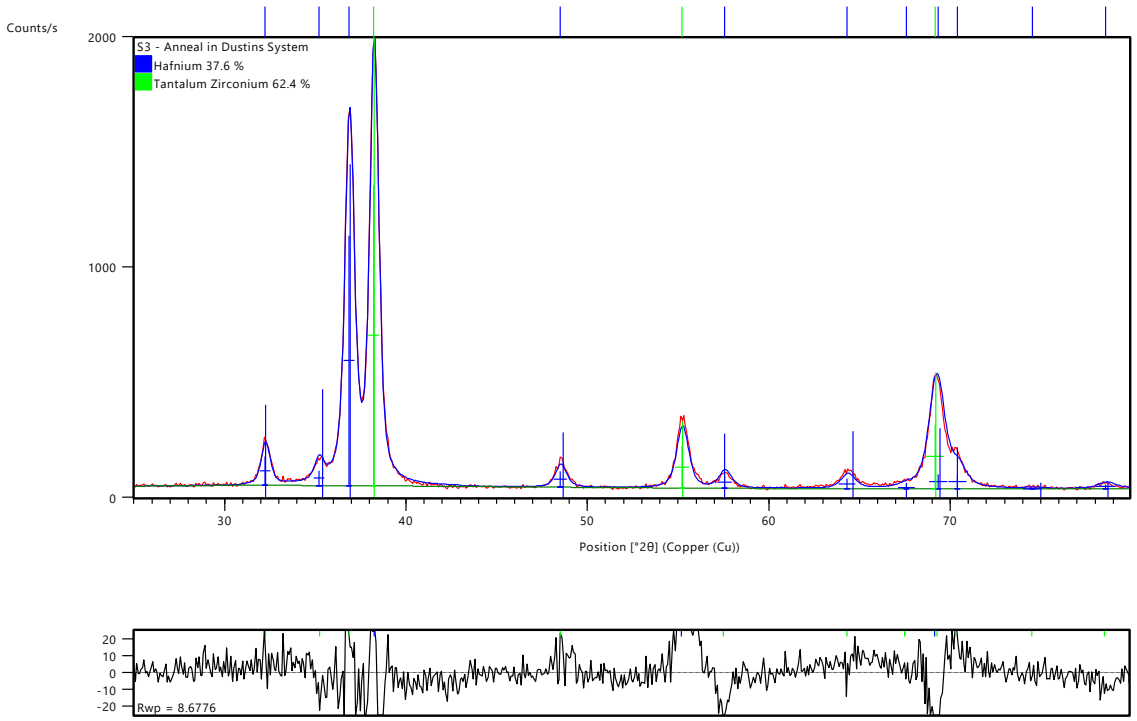

Figure 55. Rietveld fit analysis and RWP for S3.

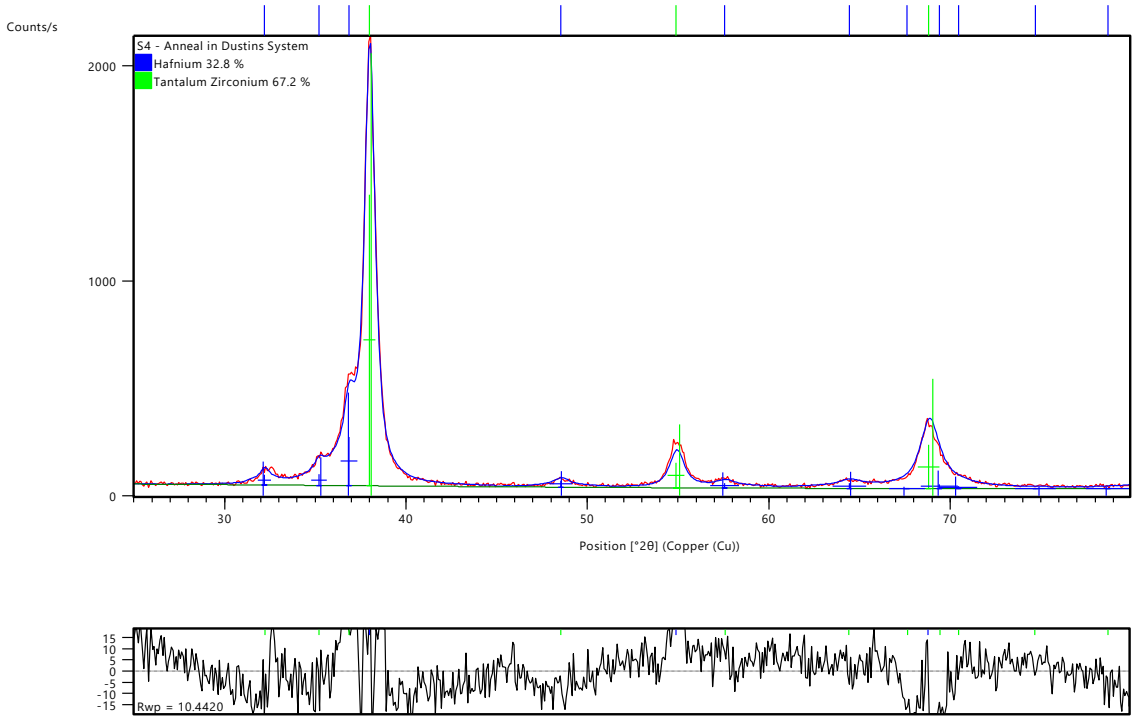

Figure 56. Rietveld fit analysis and RWP for S4.

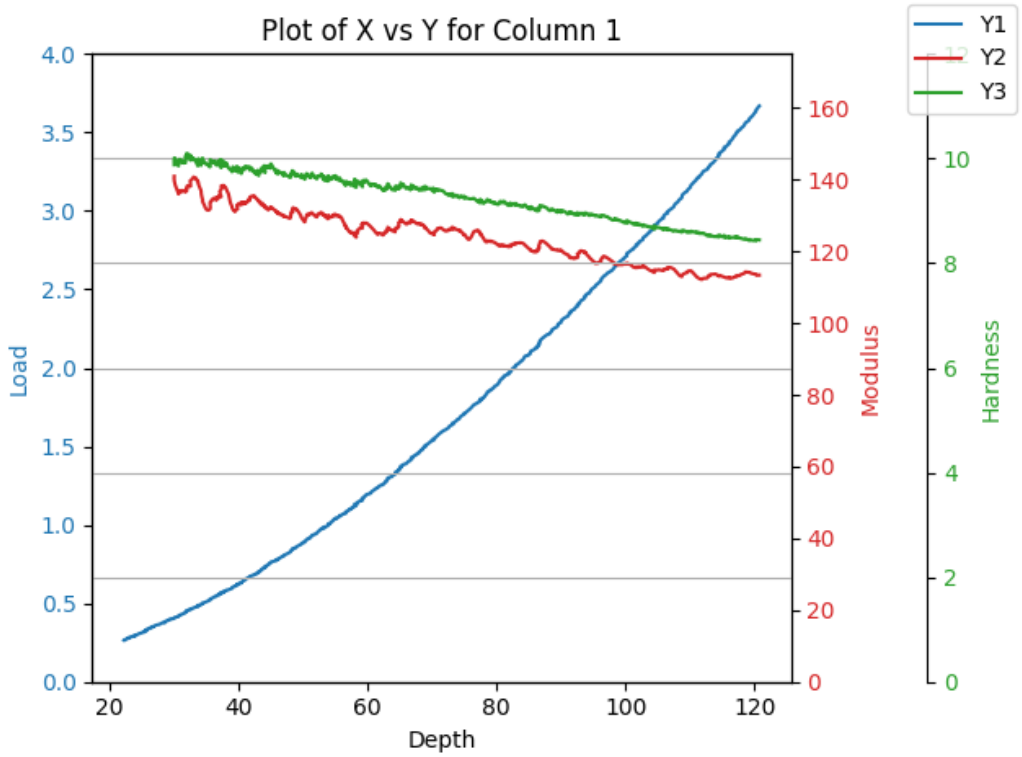

Figure 57. Example Load-Depth, Hardness-Depth, and Modulus-Depth curves for an indent in S3 that does not demonstrate TRIP behavior

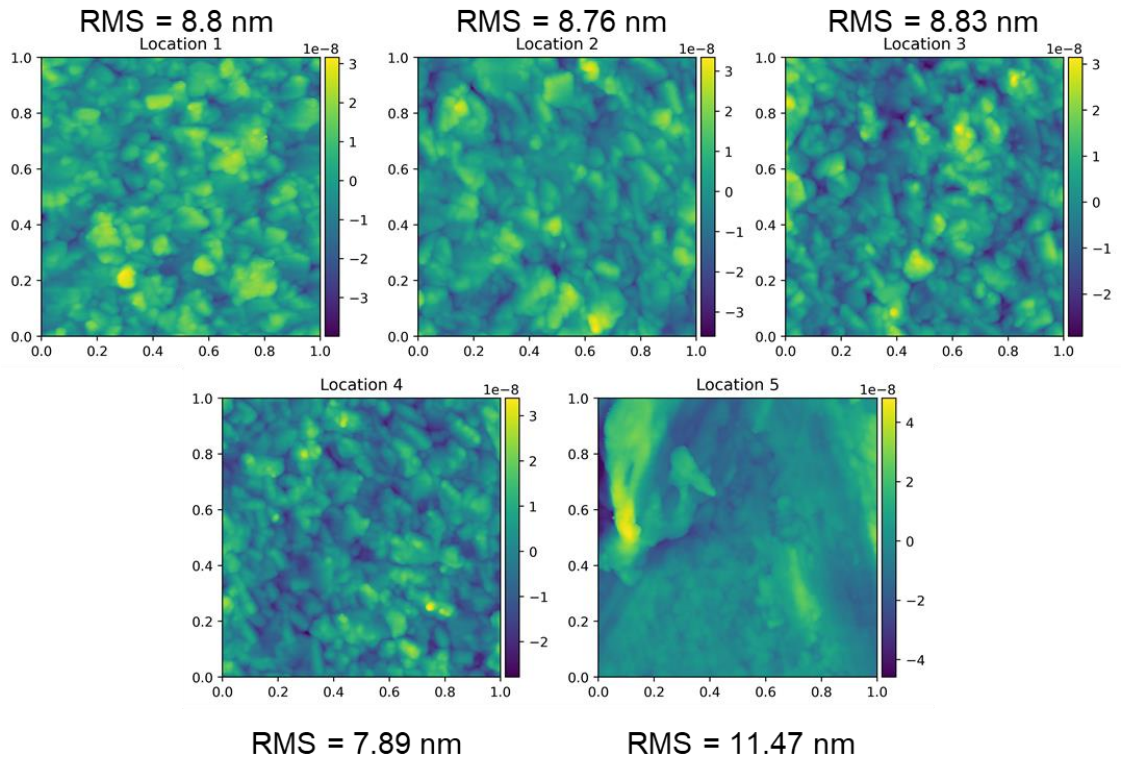

Figure 58. AFM topology maps of S5 from top (location 1) to bottom (location 5). 1 micron boxes with the RMS roughness values

VITA

Reece Emery was born and raised in Kingsport, TN by parents John and Alisa Emery alongside twin sister Hannah. He has attended the University of Tennessee since 2016 where he was awarded his Bachelor of Science degree in 2020 and his Master of Science degree in 2022 both in Materials Science and Engineering. Throughout his time at the University of Tennessee, Reece was advised by Dr. Philip Rack. His research was centered around combinatorial sputtering and focused on leveraging the technique as a rapid material discovery process in the development of next generation alloys.